Biomaterials for Monitoring and Modulating Immune Cell Function to Target Cancer and Metastasis

by

Yining Zhang

A dissertation submitted in partial fulfillment
of the requirements for the degree of
Doctor of Philosophy
(Chemical Engineering)
in The University of Michigan
2020

Doctoral Committee:

Professor Lonnie Shea, Chair
Professor Howard Crawford
Professor Joerg Lahann
Associate Professor James Moon
Associate Professor Greg Thurber

Yining Zhang

zyining@umich.edu

ORCID iD: 0000-0001-5966-0247

ACKNOWLEDGEMENTS

The work presented here would not have been possible without the support I have received from my mentors, friends, labmates (who are also friends!), and collaborators. Firstly, I would like to thank my advisor, Dr. Lonnie Shea, for his mentorship over the past five years. Thank you for always being engaged with our research, for providing invaluable expertise, and for creating an incredibly positive lab environment and community that truly fosters collaboration and camaraderie. I would like to thank my committee members, many of whom are also collaborators, for providing guidance and feedback that have helped to shape this work. I have thoroughly enjoyed working in the Shea Lab alongside my labmates, who are brilliant and driven researchers, and whom I can also call friends. To the members of Team Tumor, past and present, official and honorary, I have learned so much from working with you all. You are all so willing to set aside time to help, or discuss science, or chat about anything else. I would also like to thank the friends that I have made in grad school, especially those I met at the climbing gym. You have set the bar high for climbing, cooking, and geoguessing. I'm very grateful for my friends from college, who have been so supportive, especially in the last few months, even from afar. I'd also like to thank Larry for his support and for putting up with me during lockdown – I couldn't have asked for a better writing buddy. Finally, I'd like to thank Jason and my parents for always encouraging me to do more, and always supporting me when I couldn't.

TABLE OF CONTENTS

LIST OF FIGURES

Figure

LIST OF TABLES

Table

ABSTRACT

Despite the improvements made in the treatment of cancer in the last 50 years, metastasis still results in up to 90% of cancer related deaths. Metastatic tumor cells are not only more aggressive but they are often less immunogenic, able to escape detection and elimination by the immune system. In addition, tumor-secreted factors induce the proliferation and activation of aberrant immune cells that further suppress the anti-tumor immune response. New findings in the fields of cancer biology and cancer immunology have enabled the development of targeted therapies and immunotherapies that act to reverse this immunosuppression. The work presented here aims take an engineering approach to build upon these findings. The development and application of biomaterial platforms that can interact with and modulate immune cells, may enable better understanding and treatment of underlying mechanisms driving cancer progression and metastasis.

This work describes the application of biomaterial nanoparticles as a novel treatment for acute inflammation resulting from spinal cord injury. The nanoparticles were internalized by proinflammatory immune cells, and diverted these cells away from the injury site while reprogramming macrophages at the site to be more pro-regenerative. Increased tissue regeneration, reduced scarring, and improved functional recovery of the animal were observed with nanoparticle treatment. The immunomodulatory capabilities of nanoparticles were also tested in a model of metastatic breast cancer. The nanoparticles were found to be internalized by disease-relevant

immune cells and reduced the abundance of these cells in circulation as well as at the metastatic site. The immunomodulation resulted in slower tumor growth, fewer metastatic cells at the lung, and a survival benefit when combined with anti-PD-1 therapy. This work also explores the use of implantable biomaterial scaffolds for monitoring metastasis and disease progression, and introduces a scoring metric based on gene expression of cells recruited to the scaffold to predict therapeutic outcome and the likelihood of relapse. The scaffolds were also utilized to study the dynamics of $Gr1^+$ cell phenotype at sites of metastasis. RNA sequencing and functional studies revealed differences in the phenotype of these cells across tissues and over time. These studies add to the existing body of knowledge of $Gr1^+$ cells and introduces potential considerations in the development of drugs targeting these cells.

CHAPTER I

Introduction

1.1 Opening

Great strides have been made in the treatment of cancer in the last 50 years, but metastasis still results in up to 90% of cancer related deaths. Metastatic tumor cells are not only more aggressive but they are often less immunogenic, able to escape detection and elimination by the immune system. In addition, tumor-secreted factors induce the proliferation and activation of aberrant immune cells that further suppress the anti-tumor immune response. New findings in the fields of cancer biology and cancer immunology have enabled the development of targeted therapies and immunotherapies that act to reverse this immunosuppression. The work presented here aims take an engineering approach to build upon these findings. The development and application of biomaterial platforms that can interact with and modulate immune cells, may enable better understanding and treatment of underlying mechanisms driving cancer progression and metastasis.

1.2 Contents

Chapter 1 presents the general scope of the work and introduces the specific studies presented in this dissertation.

Chapter 2 provides the motivation and the context for the development of the biomaterial strategies explored. The background information describes the innate immune cell types that exhibit pro-tumor functions and support tumor growth and metastasis, including a literature review of previous approaches used to study and modulate these immune cells.

Chapter 3 presents the application of biomaterial nanoparticles as a novel treatment for acute inflammation resulting from spinal cord injury. The nanoparticles were delivered intravascularly and internalized by proinflammatory immune cells, and diverted these cells away from the injury site while reprogramming macrophages at the site to be more pro-regenerative. Increased tissue regeneration, reduced scarring, and improved functional recovery of the animal were observed with nanoparticle treatment. My contributions to the work included administration of the nanoparticle therapy post surgery, aiding in designing and execution of animal studies, as well as writing and editing the manuscript. This work has been published as follows:

> Jonghyuck Park, Yining Zhang, Eiji Saito, Steve J. Gurczynski, Bethany B. Moore, Brian J.Cummings, Aileen J. Anderson, and Lonnie D. Shea. Intravascular innate immune cells reprogrammed via intravenous nanoparticles to promote functional recovery after spinal cord injury. *Proceedings of the National Academy of Sciences of the United States of America*,116(30):1494714954, 2019.

Chapter 4 expands upon the the findings from Chapter 3. Nanoparticles were synthesized and tested for internalization by innate immune cells in a model of metastatic breast cancer. The nanoparticles were found to be internalized by disease-relevant cells and reduced the abundance of these cells in circulation as well as at the metastatic site, which resulted in slower tumor growth, fewer metastatic cells at the lung, and a survival benefit when combined with anti-PD-1 therapy.

Chapter 5 explores the use of implantable biomaterial scaffolds for monitoring disease progression and predicting recurrence following therapy. This work is motivated by the lack of reliable diagnostics for metastasis, and aims to close the gap for real-time monitoring of therapeutic efficacy of cancer treatments. The scaffold microenvironment was found to reflect the disease state of the animal, and gene expression analysis was used to generate a quantitative score that predicted therapeutic outcomes for surgical resection of the tumor. My contributions to the work included the adoptive transfer studies to investigate Gr1+ cell trafficking to the scaffold as a function of disease state, as well as aid in animal surgeries, sample processing, and writing and revising. This work has been published as follows:

> Oakes, R. S., Bushnell, G. G., Orbach, S. M., Kandagatla, P., Zhang, Y., Morris, A. H., Hall, M. S., LaFaire, P., Decker, J. T., Hartfield, R. M., Brooks, M. D., Wicha, M. S., Jeruss, J. S., Shea, L. D. (2020). Metastatic Conditioning of Myeloid Cells at a Subcutaneous Synthetic Niche Reflects Disease Progression and Predicts Therapeutic Outcomes. *Cancer Research*, 80(3), 602612.

Chapter 6 utilizes the scaffold detailed in the previous chapter to study the dynamics of $Gr1^+$ cell phenotype at site of metastasis. RNA sequencing was performed over these time points to assess the changes in $Gr1^+$ phenotype with disease progression. Functional studies revealed differences in the phenotype of these cells across tissues and over time. These studies add to the existing body of knowledge of $Gr1^+$ cells and introduces additional considerations in the development of drugs targeting these cells.

Chapter 7 summarizes the findings and highlights the major findings, as well as provide context for their potential impact and significance. Potential future directions for the work are also proposed.

CHAPTER II

Immune Cells in Cancer and Metastasis

2.1 Challenges to treating metastatic cancer

Metastasis, the spread of cancer cells from a tumor to secondary sites in the body, is the leading cause of cancer-related deaths. While significant progress has been made in the treatment of primary disease with development and use of chemotherapy, radiotherapy, surgery, and targeted antibody therapies, these treatments are typically not effective against metastasis. The process by which cancer cells leave the primary tumor, traffic to distal sites in circulation, and exit circulation to form a secondary growth is known as the metastatic cascade. Once tumor cells go through the metastatic cascade, they will have undergone phenotypic changes that make them more invasive and aggressive compared to cells at the primary tumor, making them more difficult to treat. Additionally, because metastatic cells are more invasive and proliferative than the primary tumor, they often have already compromised organ function by the time they are detectable by current methods.

Many of the challenges in treating metastasis and certain primary tumors lie in the complex interactions between tumor cells and the immune system. The role of the immune system in cancer has been widely studied, which has led to recent advancements in the treatment of metastatic cancer that have relied on modulating

the immune response to tumor cells. The discovery of immune checkpoints and the development of antibodies that target these checkpoints, for example, have drastically improved patient outcomes for several types of cancers. Despite these advances, there still exists a large population of patients for whom existing immunotherapies fail, which necessitates better understanding of specific immune cell interactions at the primary tumor and metastatic sites in order to develop new methods to diagnose and treat metastasis.

2.2 Understanding the immune system and the role of specific immune cells

2.2.1 The pre-metastatic niche mediates metastasis

The idea that metastatic tumor cells are attracted to a specific environment or niche traces back to Stephen Paget's 1889 "seed and soil" hypothesis [1]. Paget observed that breast cancers appeared to spread to specific organs, suggesting that metastasis was not purely a random process. Comparing the cancer cell to the "seed" and the organs to the "soil," he hypothesized that certain qualities of the organs, at the time unknown, provided a suitable environment for cancer cells that have left the primary tumor to colonize and proliferate in the organ [1].

It was not until 2005 that Kaplan and Lyden provided experimental evidence to support Paget's hypothesis [2]. Kaplan and colleagues observed the increase of vascular endothelial growth factor receptor-positive ($VEGFR1^+$) bone marrow-derived hematopoietic progenitor cells in common sites of metastasis prior to the arrival of tumor cells in human patient samples. They then injected bone marrow-derived cells (BMDCs) into mice and found that these immune cells localized to the lung and actively recruited subsequently injected tumor cells. Their experiments show

that the VEGFR1$^+$ bone marrow cells establish a "pre-metastatic niche," analogous to Paget's "soil," that attracts tumor cells from the primary tumor and promotes their growth.

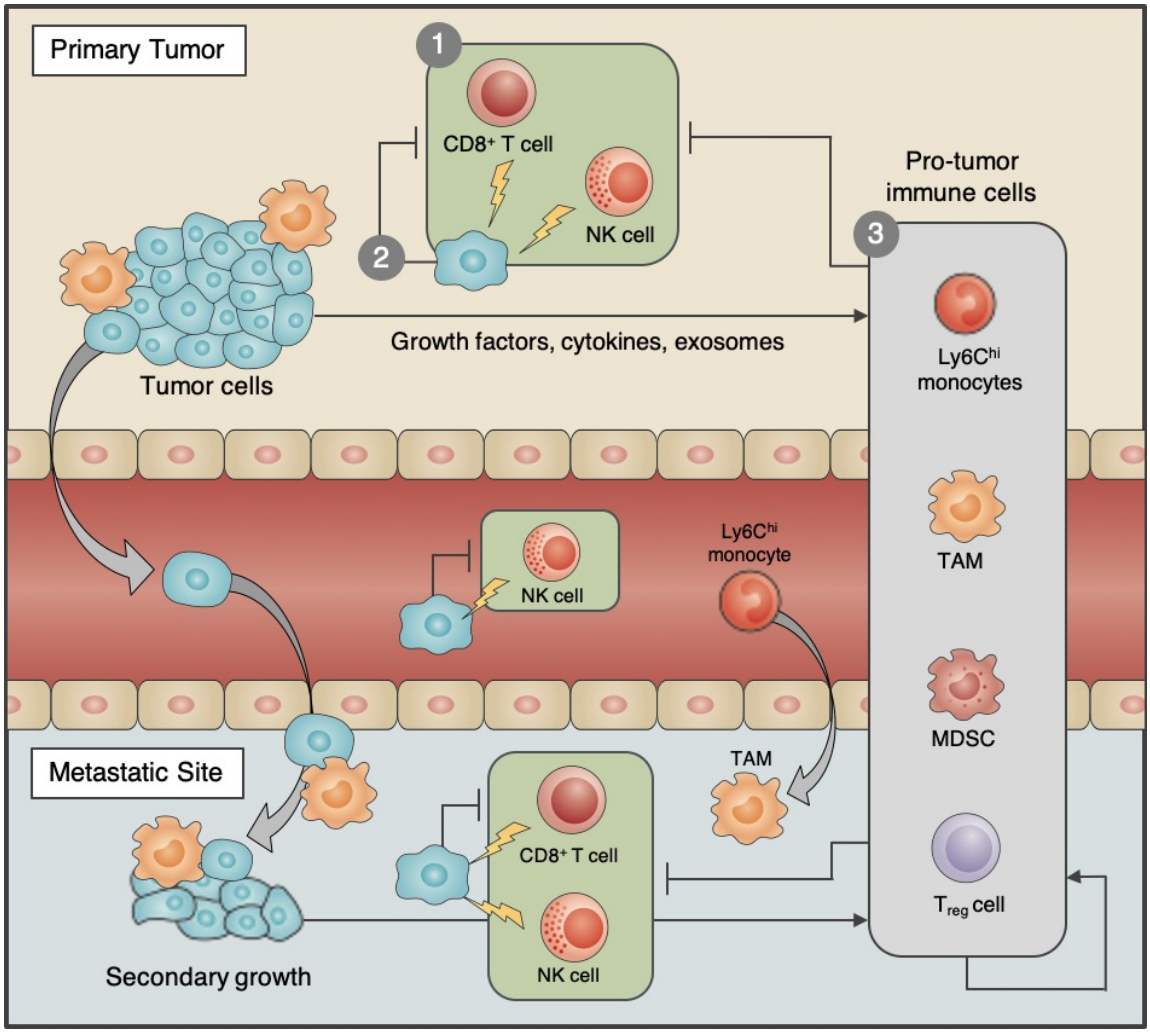

Figure 2.1: **Interactions between immune cells and tumor cells at the primary tumor and metastatic sites.** (1) Immune cells such as CD8$^+$ T cells and NK cells recognize and kill tumor cells, while (2) tumor cells display inhibitory signals that diminish the cytotoxic function of these immune cells. At the same time, (3) tumor-secreted factors induce the accumulation of pro-tumor immune cells that aid tumor growth and metastasis, and further suppress the function of T cells and NK cells. These events can be observed at both the primary tumor as well as systemically.

2.2.2 Tumors induce expansion and recruitment of pro-tumor innate immune cells

The findings from Kaplan and Lyden, which show that certain populations of immune cells promote tumor growth and metastasis, stand in contrast to what was previously understood about the role of the immune system in cancer and metastasis. The idea that the immune system protects the body from tumors was posited as early as 1909 by Paul Erlich. Furthering this concept, Burnet and Thomas introduced the idea of cancer immunosurveillance, in which innate and adaptive immune cells act to detect and eliminate tumor cells that arise in the body. More recently, however, it has been hypothesized that immune cells aid tumor cell survival through immunoediting. During immunoediting, immune cells eliminate immunogenic tumor cells and select for the tumor cells that are less immunogenic and more aggressive [3], making it more difficult for the immune system to recognize and kill these cells. In this way, immune cells unwittingly play a role in promoting tumor growth and metastasis.

In addition to the immune system supporting tumor cells through immunoediting, there now exists a substantial body of evidence indicating disease-induced immune cells are critical in establishing the pre-metastatic niche and promoting metastasis [4] (Fig. 2.1). The primary tumor secretes numerous factors to expand and recruit pro-tumor immune cells, namely myeloid-derived suppressor cells (MDSCs) and Ly6C^{hi} monocytes that differentiate into tumor associated macrophages (TAMs). These immune cells help to maintain an immunosuppressive microenvironment in the pre-metastatic niche and support tumor cell growth.

Much of the effort to understand the mechanisms by which MDSCs, monocytes, and TAMs contribute to tumor growth and metastasis has focused on the production of and response to cytokines and chemokines to recruit these innate immune cells.

A number of tumor-secreted factors involved in niche formation have been identified and studied. Interleukin-6 (IL-6), granulocyte/macrophage colony-stimulating factor (GM-CSF), and vascular endothelial growth factor (VEGF) stimulate innate immune cells to migrate out of the bone marrow and expand. Meanwhile, immune cell-secreted interferon gamma (IFNγ), Toll-like receptor (TLR) ligands, IL-13, and IL-4 in response to the tumor result in activation of these abhorrent cells [5, 6, 7]. Secreted factors can also directly interact with the pre-metastatic organ, for example, by inducing fibronectin expression [8]. Hypoxic tumor cells have also been shown to secrete lysyl oxidase (LOX), which crosslinks collagen IV at the pre-metastatic organ [9]. These changes to the extracellular matrix of the pre-metastatic niche help to recruit innate immune cells that then promote metastasis.

More recently, the role of tumor exosomes in niche formation and metastasis has been studied. Exosomes are extracellular vesicles that contain cellular contents and signaling molecules. Tumor cells have been shown to secrete exosomes that promote metastasis. Xiang et al. demonstrated that prostaglandin E2 (PGE2) and transforming growth factor-β (TGFβ) molecules within tumor exosomes cause MDSCs to accumulate [10]. Furthermore, administration of anti-PGE2 and anti-TGFβ antibodies in vivo decreased metastasis promotion by MDSCs [10]. Tumor exosomes have also been shown to induce vascular leakiness in the lung, which is an early sign of niche formation [11]. Exosomes containing integrins can determine the specific organ to which the primary tumor spreads, and have thus been implicated in metastatic organotropism [12].

2.3 The role of disease-induced myeloid cells in cancer

2.3.1 Characteristics of myeloid-derived suppressor cells

Myeloid-derived suppressor cells have garnered much attention in the past decade for their role in suppressing anti-tumor immunity. MDSCs are a heterogeneous population of immature myeloid cells that are recruited from the bone marrow to the tumor and metastatic sites. In mice, these cells are characterized by surface expression of myeloid markers CD11b and Gr-1 (Ly6C/Ly6G), though these cells are not distinguishable from neutrophils, monocytes, and macrophages by surface markers alone [5]. Two subsets of MDSCs (characterized by $Ly6C^{lo}/Ly6G^{+}$ and $Ly6C^{hi}/Ly6G^{-}$ in mice) have been identified and there is increasing evidence to suggest that these two populations have distinct pro-tumor functions. In humans, MDSCs exhibit similar immunosuppressive functions, and are also identified by surface expression of a number of myeloid lineage markers. Though there remains some ambiguity in the identification of MDSCs, the suggested nomenclature for these cells in mice and humans are detailed in the review from Bronte et al. [13].

2.3.2 MDSCs suppress T cell function

The success of most existing immunotherapies relies on the ability of $CD8^{+}$ T cells to recognize and kill tumor cells once they have been detected in the body. T cells that are primed to recognize tumor antigen are highly specific for tumor cells, and are efficient at recognizing and killing these cells. T cells also help to generate memory against these antigens to provide long-term immunity. However, tumor cells secrete or induce expression of factors that suppress T cell function. Immune checkpoint blockade therapies, such as anti-PD-1 and anti-CTLA-4 antibodies, work by

blocking the tumor and metastatic microenvironment from inducing T cell anergy and activation by dendritic cells (DCs), respectively [14]. Clinical evidence suggests that there is an additive effect in checkpoint blockade, in that combinations of multiple checkpoint inhibitors have been shown to be more effective than single inhibitors. Chimeric antigen receptor (CAR) T cell therapy aims to increase the ability of T cells to recognize tumor antigens. Similarly, increased efficacy has been reported for armored CAR T cells, which are engineered to secrete stimulatory cytokines that help the CAR T cells to overcome tumor-induced immunosuppression. Dendritic cell (DC)-based therapeutic vaccines such as Sipueleucel-T comprise of dendritic cells are stimulated in vitro with tumor antigen and adoptively transferred into the patient so the DCs can more readily activate adaptive response against the tumor cells [15]. The efficacy of combination therapies illustrates the need to overcome multiple mechanisms by which tumor cells and the tumor environment can suppress adaptive immunity.

MDSCs primarily inhibit T cell function through the upregulation of immunosuppressive factors including arginase 1 (Arg1) and inducible nitric oxide synthase (iNOS) and increased production of reactive oxygen species (ROS) and nitric oxide (NO) [5]. Studies have shown that these MDSC-derived factors induce regulatory T cells (Tregs) [4]. In addition to $CD8^+$ T cells, NK cells have also been shown to play a role in tumor cell killing by recognizing the absence or downregulation of MHC I expression on the surface of tumor cells. The presence of MDSCs in tissues resulted in decreased NK cell cytotoxicity [7].

2.3.3 Contributions of monocytes and tumor associated macrophages

Aberrant monocytic cells, characterized as being $CD11b^{+}$ $Ly6C^{hi}/Ly6G^{-}$ in mice, are also referred to as monocytic MDSCs (M-MDSCs). These have been shown to differentiate into tumor associated macrophages (TAMs), which interact with primary tumor cells to promote both tumor growth and metastasis [16]. The importance of monocytes and TAMs in tumor growth and metastasis has been highlighted by a number of studies in which these cells are depleted or their recruitment to the tumor or metastatic sites is blocked. Blockade of monocyte recruitment with a small molecule inhibitor of C-C motif chemokine ligand 2 (CCL2/MCP-1), for example, resulted in reduced tumor growth and metastasis [17]. Other studies that induced ablation of these cell types also resulted in reduced disease progression [18].

2.3.4 Expansion and recruitment of myeloid cells

Expansion and migration of MDSCs is attributed to a large number of tumor-induced factors including prostaglandins, GM-CSF, macrophage colony-stimulating factor (M-CSF), several interleukins (IL-1β, IL-6, IL-10, IL-12), and transforming growth factor beta (TGF-β) have all been shown to contribute to expansion and activation of MDSCs [4, 13, 5]. CCL2/MCP-1 has been identified as a potent driver of MDSC trafficking to the tumor; several studies that block CCL2 have demonstrated reduced metastasis and tumor growth. C-X-C motif chemokine receptor 2 (CXCR2) and its ligands (CXCL1, CXCL2, CXCL5), as well as S100A8/9, have also been implicated in the recruitment of MDSCs to tumors and metastatic sites.

2.3.5 Myeloid cells alter the tumor and metastatic microenvironments

In addition to direct immune suppression through $CD8^+$ T cell inhibition, MDSCs also support tumor growth and metastasis through the production of factors that remodel the tumor and metastatic microenvironment. At the primary tumor as well as at metastatic sites, MDSCs exhibit increased matrix metallopeptidases (MMPs), in particular MMP-9, which remodel the tumor extracellular matrix in order for tumor cells to spread and metastasize. MMP-9 also increases levels of VEGF in the tumor microenvironment, and the presence of MDSCs has been shown to reduce the efficacy of anti-VEGF therapy [19]. Taken together, these studies elucidate the multi-faceted roles of innate immune cells in promoting metastasis and tumor growth. In addition, the large number of interactions and signaling molecules that have been studied also serve to highlight the complexity of the interactions between tumor and immune cells as well as the need for better understanding and more effective treatments.

2.4 Scaffold-based strategies for studying and modulating immune cell function *in vivo*

2.4.1 Implantable scaffolds recruit tumor cells *in vivo*

Given the complexities of the interactions between innate immune cells and tumor cells, there remain many aspects of myeloid cells at the pre-metastatic niche that have yet to be investigated. The ability to study these interactions *in vivo* is limited by the difficulty in detecting micro-metastases. In addition, analyses of these sites often require explanting the diseased tissue, which prevents longitudinal monitoring of gene expression throughout disease progression. Implantable scaffolds have emerged as a method to recapitulate the metastatic niche environment for further study.

2.4.2 Cargo-free polymer scaffolds

The Shea lab has developed porous polycaprolactone (PCL) scaffolds that can be used to study the metastatic environment *in vivo*. The scaffold structure is comprised of a network of interconnected pores that support cell infiltration and colonization, resulting in the recruitment of metastatic and highly aggressive tumor cells [20]. It has been shown that key immune cells such as MDSCs, monocytes, and macrophages traffic to the scaffold from the peripheral blood to form an attractive environment for circulating tumor cells to home. Subsequently, the scaffolds are able to lower the tumor burden in other metastatic organs to provide a therapeutic benefit to the animal [21, 22].

Polymer scaffolds not only have therapeutic and diagnostic potential but are also important tools that can be leveraged to further study metastasis. Little is known about the dynamics of early niche formation or cancer cell colonization *in vivo* because the pre-metastatic niche is difficult to identify until the arrival of tumor cells. Porous PCL scaffolds provide a unique opportunity to study the dynamics of niche formation in immune competent BALB/c mice as well as in other cancer modles. Rao et al. have that demonstrated immune changes occur in scaffolds in the presence of a primary tumor to form the pre-metastatic niche [22]. However, these data provide a static image of the immune cells at the scaffold, and do not indicate whether or not the cells proliferate once at the scaffold, or if they leave the scaffold and are constantly replenished by interaction with the primary tumor. Further elucidating the process of niche formation and the role of immune cells within the niche will inform potential diagnostic and therapeutic interventions.

2.4.3 Loaded polymer scaffolds

Other groups have also created polymer scaffolds or microparticles that recruit tumor cells *in vivo*. These approaches included the released chemokines, or the scaffolds were embedded with extracellular matrix proteins or were seeded with stem cells in order to recruit metastatic tumor cells to the scaffolds [23, 24]. Scaffolds have also been seeded with cells or loaded with protein or lentivirus expressing cytokines or growth factors to study the effects of these factors on the recruitment of tumor cells [25].

2.5 Methods for targeting innate immune cells

In addition to studying innate immune cells to monitor disease progression, there has been considerable effort towards developing therapies that target the immunosuppressive function of disease-induced myeloid cells. Many of the previous studies targeting pro-tumor innate immune cells in the tumor microenvironment, namely MDSCs, monocytes, and TAMs, act by either 1) blocking cell trafficking to the tumor and metastatic sites, or 2) depleting the immune cells.

Macrophages have been depleted with small molecule colony stimulating factor 1 receptor (CSF1R) inhibitors, though the mechanism of inhibition appears to greatly influence therapeutic outcomes. In one study, depletion of TAMs using BLZ945 was effective against primary disease, but appeared to be tissue-specific and was not able to reduce the number of TAMs or reduce tumor burden in the lung in PyMT model [18]. Other studies employing CSF1R blockade observed increased sensitivity of tumors to paclitaxel [26] [deNardo 2011] and anti-PD-1 [27]. Similarly, blocking neutrophil recruitment to the pre-metastatic site and inhibition of

leukotriene-generating enzyme arachidonate 5-lipoxygenase (Alox5) has been shown to reduce metastasis in vivo [28]. However, there is evidence that there exist redundant pathways to activating and recruiting TAMs to sites of metastasis, suggesting that blocking CCL2/CCR2 signaling alone is not enough to reduce metastasis [29]. Macrophage populations are also readily reduced or depleted with clodronate liposomes, which induces apoptosis upon uptake. One such study demonstrated that macrophage depletion with clodronate liposomes and zoledronic acid used in combination with sorafenib inhibited tumor progression, angiogenesis, and lung metastasis compared with sorafenib alone in models of hepatocellular carcinoma [30]. Depletion of TAMs through systemic injection of clodronate liposomes has also shown efficacy in reducing tumor growth in instances where CCL2 blockade has not [31]. Additional studies involving ablation of TAMs demonstrate the challenges in targeting cells that have migrated into tissues [32]. These studies highlight the therapeutic potential in depletion of tumor associated macrophages, and the need for a more effective method for doing so.

2.5.1 Inhibition of immune cell trafficking

As previously mentioned, inhibition of immune cell recruitment to tumors or metastatic sites has been shown to be effective in reducing tumor growth and metastasis. A commonly used method for preventing cell trafficking employs small molecule inhibitors of surface receptors for chemokines. In one such study, antibody blockade of CCL2-CCR2 binding using anti-CCL2 antibody was shown to reduce the number of metastatic nodules in several mouse models of metastatic breast cancer [17]. By leveraging a different mechanism, several groups observed that antibody targeting of CCR2 results in deletion of CCR2-expressing monocytes and macrophages and ob-

served improved disease outcomes. In combination with anti-PD-1, anti-CCR2 also extended survival in glioma models, which were previously shown to be resistant to anti-PD-1 [33].

CHAPTER III

Intravascular Innate Immune Cells Reprogrammed via Intravenous Nanoparticles to Promote Functional Recovery After Spinal Cord Injury

3.1 Authors

Jonghyuck Park, Yining Zhang, Eiji Saito, Steve J. Gurczynski, Bethany B. Moore, Brian J. Cummings, Aileen J. Anderson, and Lonnie D. Shea

3.2 Abstract

Traumatic primary spinal cord injury (SCI) results in paralysis below the level of injury and is associated with infiltration of hematogenous innate immune cells into the injured cord. Methylprednisolone has been applied to reduce inflammation following SCI, yet was discontinued due to an unfavorable risk-benefit ratio associated with off-target effects. In this study, i.v. administered poly(lactide-coglycolide) nanoparticles were internalized by circulating monocytes and neutrophils, reprogramming these cells based on their physicochemical properties and not by an active pharmaceutical ingredient, to exhibit altered biodistribution, gene expression, and function. Approximately 80% of nanoparticle-positive immune cells were observed within the injury, and, additionally, the overall accumulation of innate immune cells

at the injury was reduced 4-fold, coinciding with downregulated expression of proinflammatory factors and increased expression of antiinflammatory and proregenerative genes. Furthermore, nanoparticle administration induced macrophage polarization toward proregenerative phenotypes at the injury and markedly reduced both fibrotic and gliotic scarring 3-fold. Moreover, nanoparticle administration with the implanted multichannel bridge led to increased numbers of regenerating axons, increased myelination with about 40% of axons myelinated, and an enhanced locomotor function (score of 6 versus 3 for control group). These data demonstrate that nanoparticles provide a platform that limits acute inflammation and tissue destruction, at a favorable risk-benefit ratio, leading to a proregenerative microenvironment that supports regeneration and functional recovery. These particles may have applications to trauma and potentially other inflammatory diseases.

3.3 Introduction

Traumatic spinal cord injury (SCI) results in an initial injury, followed by secondary events that can last from hours to weeks leading to permanent loss of function [34, 35, 36]. Inflammatory responses are initiated in part by the rapid influx of immune cells, including inflammatory monocytes and neutrophils, via a broken blood-spinal cord barrier. These cells infiltrate the injury site within hours and secrete proinflammatory cytokines, reactive oxygen species, and nitric oxide, all of which can contribute to additional neuronal cell death, axonal demyelination, and functional deficits following SCI [37, 38, 39, 40]. Critically, while glucocorticoids such as methylprednisolone were once the standard of care for acute SCI due to their antiinflammatory properties, these agents are also associated with unfavorable

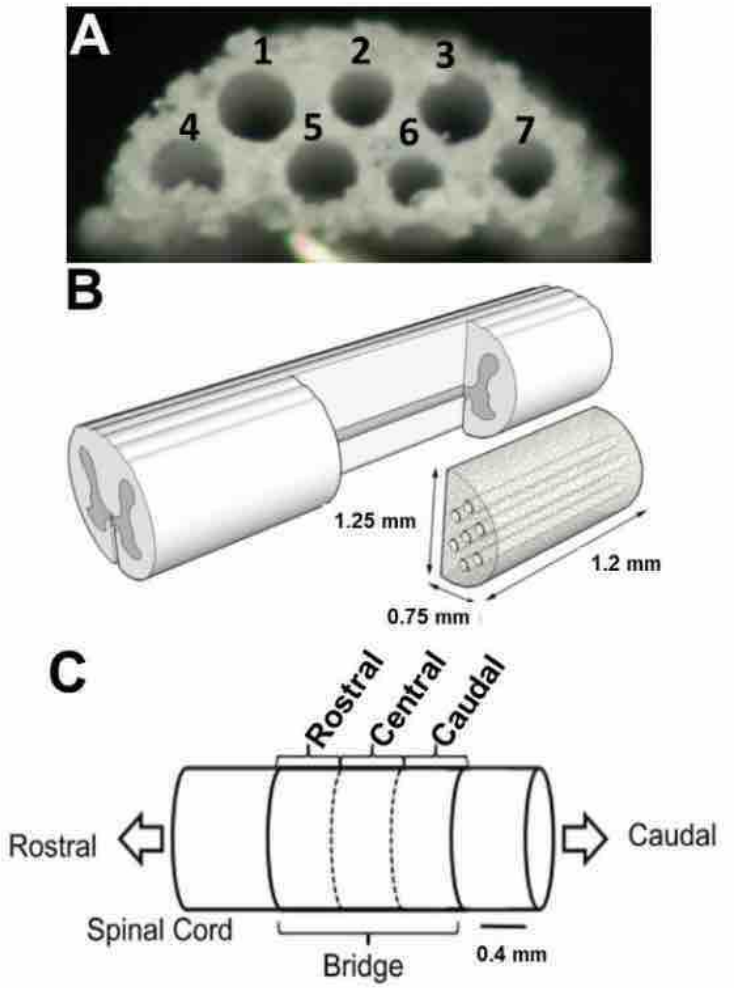

Figure 3.1: **PLG multichannel bridge and hemi-sectional SCI model. (A) Photomicrograph of a bridge with 200 μm multichannel.** (B) Schematic representation of hemi-section SCI at T9-T10 and multichannel bridge implantation illustrating approximate bridge dimensions. (C)Schematic multichannel bridge regions where the bridge was divided for analysis. From the rostral edge of the bridge/tissue interface, rostral region analysis was done at 0-400 μm, central at 400-800 μm, and caudal at 800-1200 μm.

side effects, such as sepsis, gastrointestinal bleeding, and thromboembolism [41, 42], indicating that improved methods are needed. Systemic depletion of neutrophils or monocytes has either not altered or has had a small effect on SCI outcome [43]. Because monocytes and neutrophils are necessary for wound healing and tissue regeneration after injury, reprogramming the immune response could be a more effective strategy to minimize loss of function and enable repair.

We have previously demonstrated that 500-nm-diameter poly(lactide-coglycolide) (PLG)-based nanoparticles (NPs) carrying a negative zeta potential distract circulating immune cells such as inflammatory monocytes and neutrophils away from the injury site [44, 45]. i.v.-administered NPs reduced pathological symptoms and produced a therapeutic benefit in inflammation-mediated diseases on the central nervous system (CNS) including West Nile virus, encephalitis, and experimental autoimmune encephalomyelitis [44, 45, 46]. Highly negatively charged NPs are thought to bind to the scavenger receptor on circulating immune cells, effectively reprogramming them to influence their trafficking to the spleen and, thus, indirectly attenuate the immune pathology at the inflamed area [45, 46]. In SCI, recent studies demonstrate that hematogenous-infiltrating immune cells are predominantly responsible for secondary axonal dieback, suggesting that reducing hematogenous immune cell infiltration at early time points may indirectly reduce tissue degeneration by attenuating the inflammation-mediated secondary events [47, 48]. Reprogramming immune cells to accumulate at the injury and assume proregenerative phenotypes may provide a means to directly modulate the injury environment to promote regeneration.

Herein, we investigate NPs that reprogram inflammatory cells intravascularly to obtain a fraction that home to the injury and modulate the microenvironment, resulting in enhanced regeneration and functional recovery after SCI. NPs (500 nm

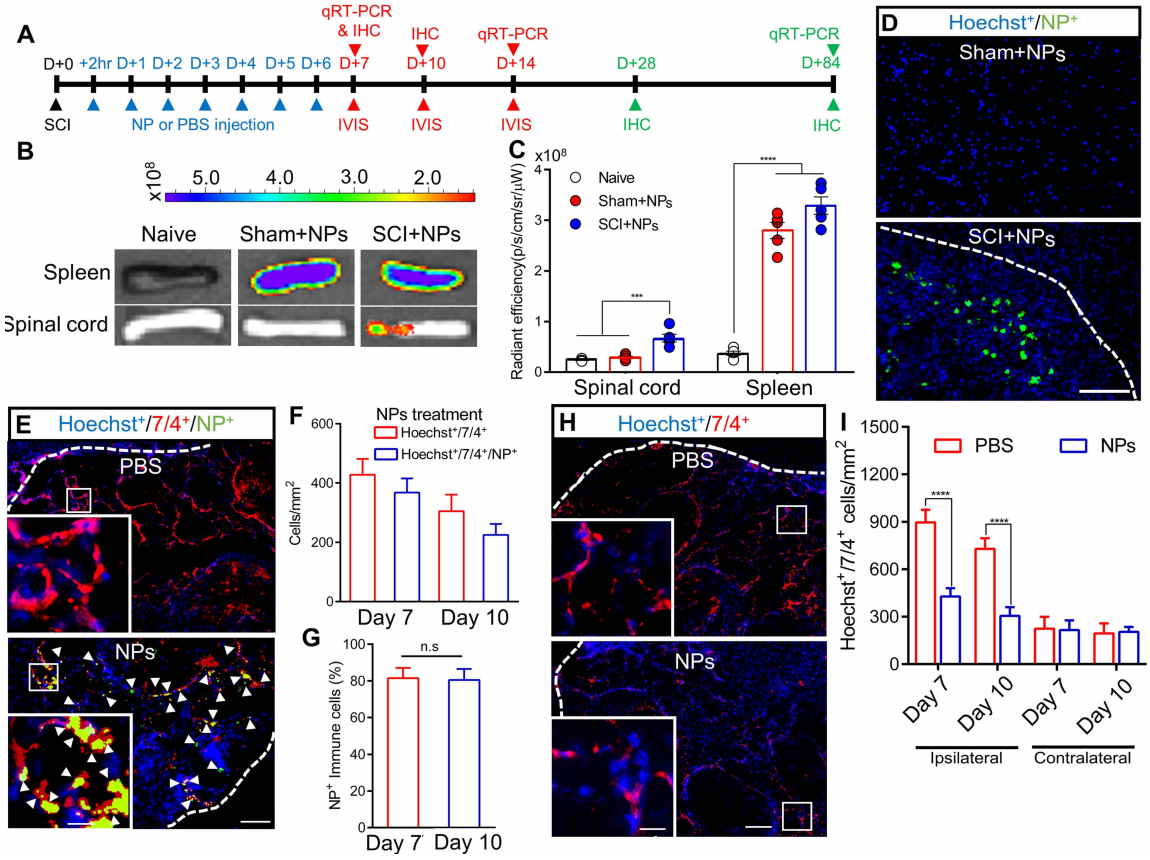

Figure 3.2: ***In vivo* biodistribution analysis and internalization of NPs.** (A) Experimental timeline in this study. (B) *In vivo* imaging system images from the spinal cord and spleen were acquired at day 1 after injection. (C) The fluorescence intensity was quantified in organs from all conditions. (D) NPs-Cy5.5 were observed within the injury from SCI group at day 7 after SCI. The white line indicates implanted bridge area within the spinal cord. (E) Spinal cord sections were labeled with anti-7/4 and Hoechst at day 7 after SCI. NPs-Cy5.5 colocalized with inflammatory monocytes/neutrophils (yellow) within SCI in the NP group. (Inset) High-magnification image of Hoechst$^+$/7/4$^+$/NP$^+$ within bridge area (white arrowheads). (F) and (G) The number of Hoechst$^+$/7/4$^+$/NP$^+$ and Hoechst$^+$/7/4$^+$ cells within bridge area from the NPs group (F) and percentage of NPs-Cy5.5 expressing immune cells (G) at day 7 and 10 after SCI. More than 80% of immune cells were colocalized with NPs-Cy5.5 within SCI. (H) 7/4$^+$ immune cells distribution from both groups at day 10 after SCI. (I) Number of accumulated immune cells was quantified at day 7 (E) and 10 (H) after SCI from both conditions from ipsilateral and contralateral sides. A 2-way ANOVA with Tukeys post hoc test for the multiple comparisons or unpaired t test (2-tailed) was performed (G), where ***P<0.001 and ****P< 0.0001 compared with PBS group, mean ± SD, n = 5 per group and time point. n.s., not significant. (Scale bars: D, 200 μm; E, 50 μm; H, 100 μm.)

diameter, zeta potential < -30 mV) were administered i.v. daily for 7 d immediately after SCI. A lateral hemisection SCI model was employed, with bridge implantation employed in all studies as a means to define a region in which spared axons can be distinguished from regenerating axons (Fig. 3.1). We investigate the biodistribution of NPs among tissues by fluorescence imaging and, subsequently, within the spinal cord. Inflammatory responses were characterized histologically and through gene expression analysis. Regeneration following NP treatment was assessed through the number of axons, the presence of serotonergic axons, and myelination of axons with locomotor functional testing performed. The administration of NPs targets innate immune cells to reprogram their function, which represents a strategy for neuroprotection and neuroregeneration after SCI.

3.4 Results

3.4.1 NP Internalization and Immune Cell Sequestration

In vivo images were acquired to investigate the biodistribution of NPs. Initially, NPs (1 mg, Cy5.5-conjugated [NPs-Cy5.5]) were administered i.v. on a daily basis for 7 d starting the day of injury (Fig. 3.2A). The spinal cord, spleen, and liver were collected for analysis at day 1, 4, and 8 after injection from all conditions (day 7, 10, and 14 after SCI) (Fig. 3.2B and Figs. 3.3 and 3.4). In both SCI and sham groups, the greatest fluorescence intensity from NPs was observed in liver. However, fluorescence associated with NPs was also observed in the spinal cord and spleen (Fig. 3.2C). Radiant efficiency levels associated with NPs-Cy5.5 in the spinal cord were approximately 3-fold greater in the SCI group compared with the sham group; in contrast, in the spleen and liver, no differences were observed between sham and

SCI groups. Subsequently, fluorescence levels gradually decreased in all sites over time (Figs. 3.3 and 3.4). At day 4 after injection (day 10 after SCI), the fluorescence associated with NPs-Cy5.5 was substantially decreased in the spleen and liver, yet no significant differences were observed in the spinal cord compared with those at day 1 post injection. However, the fluorescence associated with NPs-Cy5.5 was decreased in all organs as in the naïve group at day 8 after injection.

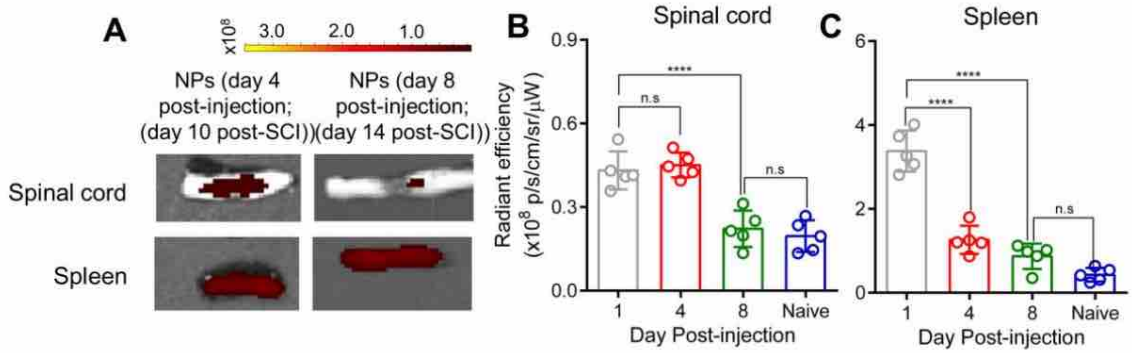

Figure 3.3: ***In vivo* biodistribution of NPs over time.** (A)The spinal cord and spleen were collected from SCI with NPs treatment group at day 4 and 8 post-injection and IVIS images were acquired. (B) and (C) The fluorescence intensity was quantified in spinal cord (B) and spleen (C)as a function of time. A two-wayANOVA with Tukeys post hoc test for the multiple comparisons, where ****P<0.0001, mean ± SD, n=5/group and time point.

Next, the distribution of particles within the spinal cord and cell types with internalized particles were investigated. Cy5.5 fluorescence was observed within the bridge area after SCI (Fig. 3.2D). In addition, immunofluorescence data indicated that about 80% of NPs-Cy5.5 were colocalized with 7/4 $(\text{Ly-6B.2})^{+}$ inflammatory monocytes/neutrophils within the bridge (Fig. 3.2 EG). Anti-7/4 was selected as a marker for inflammatory monocytes/neutrophils, since the 7/4 antigen is present on the cell surface of both inflammatory monocytes and neutrophils [49]. We subsequently investigated inflammation within the spinal cord, specifically focusing on the accumulation of inflammatory monocytes/neutrophils and gene expression asso-

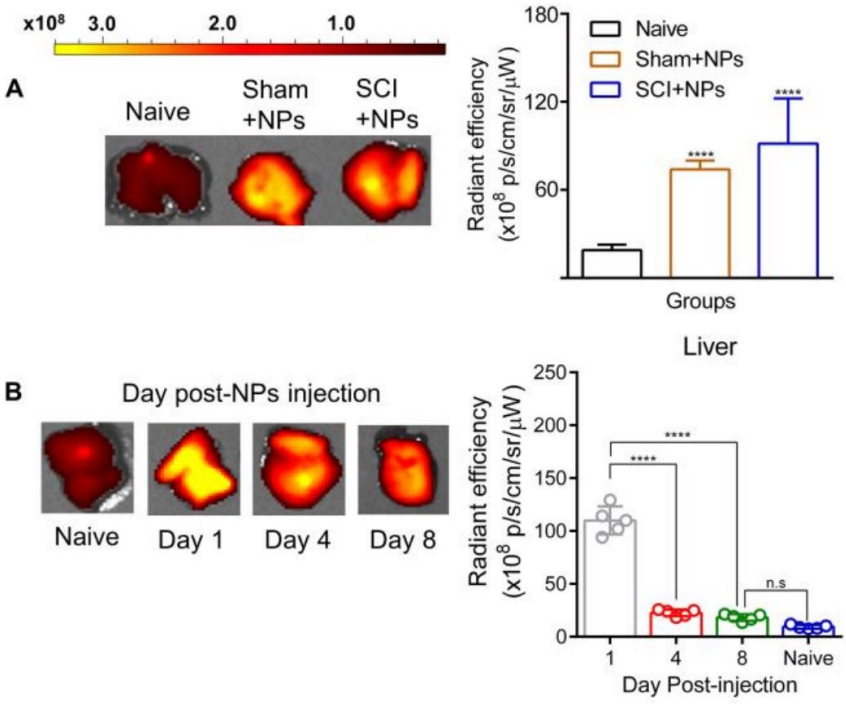

Figure 3.4: **NPs biodistribution in liver after SCI** (A) IVIS images from the liver were acquired at day 1 post-NPs injection. Radiant efficiency levels associated with NPs-Cy5.5in sham and SCI groups were substantially increased compared to nave group. (B) The liver wascollected from SCI with NPs treatment group and the fluorescence intensity was quantified at various time points in liver. A two-way ANOVA with Tukeys post hoc test for the multiple comparisons, where****p<0.0001, mean ± SD, n=5/group and time point.

ciated with immune cells. At days 7 and 10 after SCI, $7/4^+$ cell numbers in the injury with NP administration were significantly reduced relative to control conditions and no differences were observed in contralateral spinal cord (Fig. 3.2 H and I and 3.5). Gene expression levels for neutrophils (CD11b and Ly6G) and inflammatory monocytes (CCR2 and Ly6C) were investigated in the spinal cord and spleen at day 7 after SCI. The data indicated that NP administration significantly decreased the expression of genes associated with neutrophils and inflammatory monocytes within the spinal cord compared with the phosphate-buffered saline (PBS) group (Fig. 3.6A). Although Ly6C gene expression level within the spleen for NP treatment trended toward greater expression compared with the PBS group, these trends were not sig-

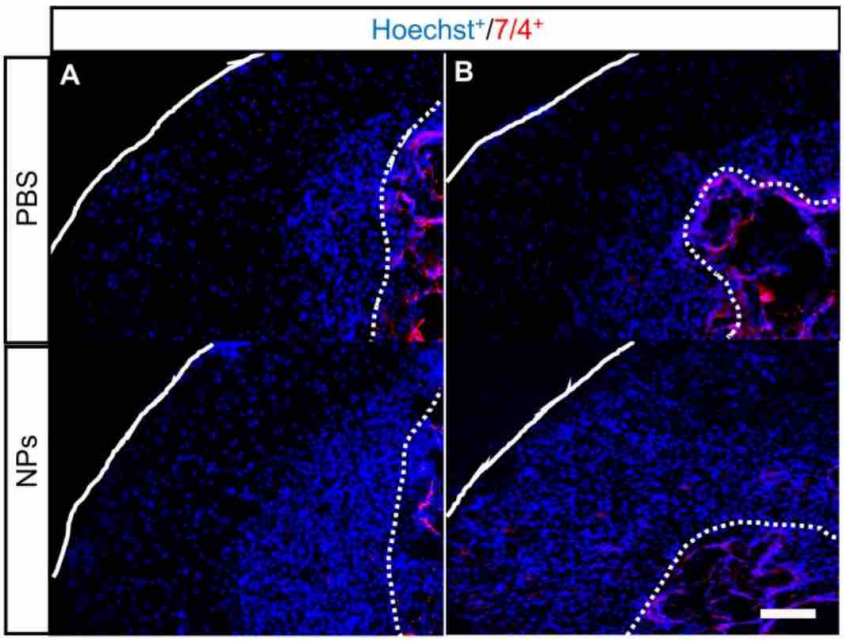

Figure 3.5: **Inflammatory monocytes/neutrophils distribution within contralateral side of spinal cord.** (A and B) Contralateral side of spinal cord sections were stained with anti-7/4 and Hoechst at day 7 post-SCI (A) and at day 10 post-SCI (B) from both PBS and NPs groups. Dashed line indicates the implanted bridge area and white line indicated host spinal cord, scale bar = 200 μm.

nificant. However, CD11b, Ly6G, and CCR2 expression levels in the spleen from the NP group were significantly increased relative to the PBS group (Fig. 3.6B). In the spleen, NPs colocalized with 7/4 cells (Fig. 3.7) and MARCO$^+$ cells (Fig. 3.8 AC). Additionally, *in vitro* NP internalization assays demonstrated that addition of soluble MARCO significantly decreased NPs internalization (Fig. 3.8D). Collectively, in agreement with previous studies [45, 46, 50], these results suggest that NP administration associates with innate immune cells such as inflammatory monocytes and neutrophils, which influence their numbers in the spleen and spinal cord. In addition, NP administration contributes to decreasing immune cells accumulation at inflamed sites.

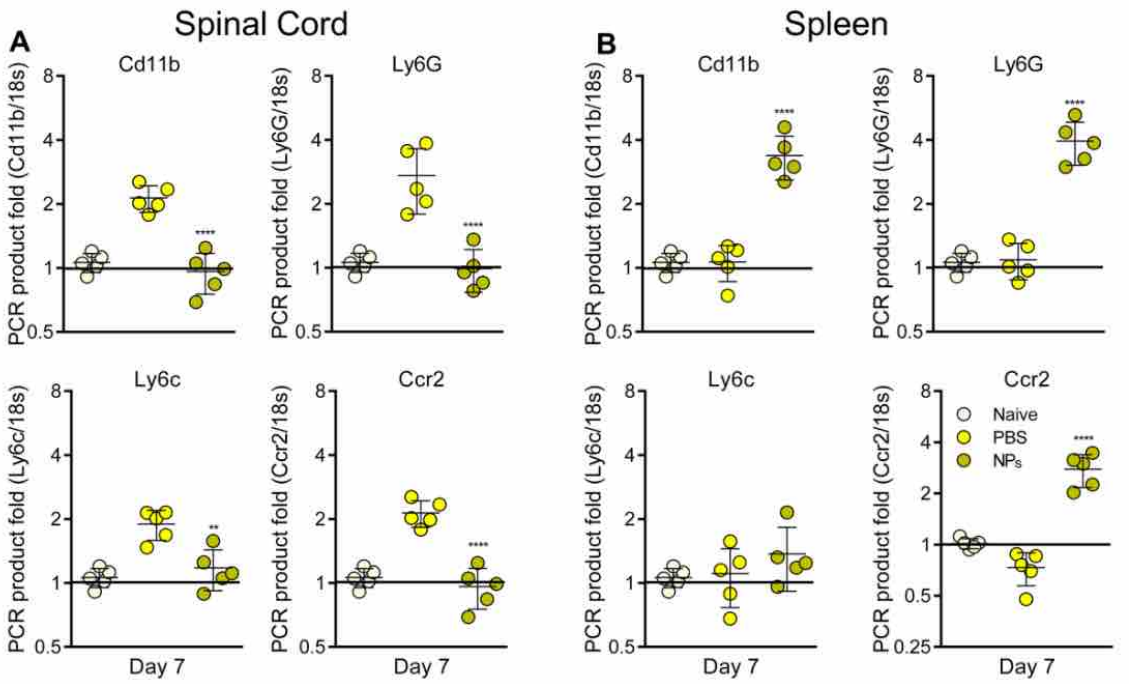

Figure 3.6: **Gene expression of neutrophils markers Cd11b and Ly6G and inflammatory monocytes markers Ly6c and Ccr2** were investigated from (A) spinal cord and (B) spleen through qRT-PCR at day 7 post-SCI in all conditions. The data suggest that NP-Cy5.5 downregulate the levels of neutrophils and inflammatory monocytes at the injured area. A one-way ANOVA with Tukeys post hoc test for the multiple comparisons, where **P<0.01, and ****P<0.0001 n=5/group.

3.4.2 NPs Induce Macrophage Polarization at the Injury Site

We next investigated macrophage polarization following NP treatment of SCI, as macrophages play pivotal roles in inflammatory responses after injury [47, 51] (Fig. 3.9). Macrophages have the potential for plasticity in their phenotype depending on their microenvironment, and although macrophage phenotypes are not binary, they have been classified as inflammatory M1 and proregenerative M2 phenotypes for ease of description [51]. We have reported that M2 macrophages contribute to creating proregenerative microenvironments leading to axonal regrowth and remyelination, and locomotor recovery after SCI [52, 53]. Analysis of markers for M1 and M2 macrophages in the spinal cord indicated that expression levels of the proinflammatory markers inducible nitric oxide synthase (iNOS), CD86, and monocyte

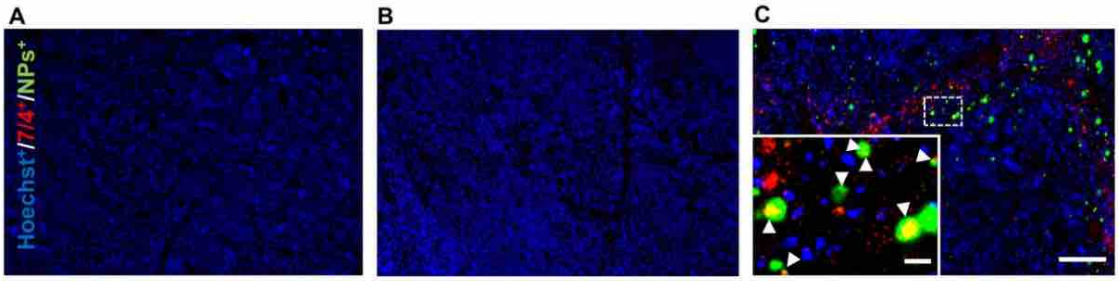

Figure 3.7: **$7/4^+$ immune cells and NPs colocalization in the spleen.** Spleen sections were collected from (A)naïve, (B) PBS injection, and (C)NPs injection groups and were labelled with Hoechst and anti-7/4 at day 7 post-SCI. NPs-Cy5.5 were colocalized with inflammatory monocytes/neutrophils within the spleen in NPs group. Inset: high-magnification image of $Hoechst^+/7/4^+/NP^+$ within the spleen (yellow, scale bar: 200 μm

chemoattractant protein-1 (MCP-1) were significantly down-regulated in the NPs compared with the PBS group from day 7. As key markers for M1 phenotypes, these factors are associated with inflammatory responses and release of proinflammatory factors, contributing to an inhibitory microenvironment at the injury [51]. In contrast, levels of the M2 markers CD206 and interleukin (IL)-10 were significantly increased in the NPs relative to the PBS group. These results were maintained until day 84 after SCI (Fig. 3.9 A and B). In agreement with previous studies [52, 54], no difference was observed in Arginase1 (Arg1) expression between groups at day 7, yet Arg1 was significantly up-regulated following NP treatment at day 14 and 84 after SCI compared with PBS. Interestingly, expression levels of proinflammatory factors (CD86 and MCP-1) were reduced in the PBS group compared with SCI only, while antiinflammatory markers (Arg1 and CD206) were substantially increased in the PBS group compared with SCI only at day 84 after SCI, indicating a role of the bridge for limiting inflammation. Subsequently, immunofluorescence data were investigated to quantify the total number of $CD206^+$ cells ($Hoechst^+/CD206^+$), macrophages ($Hoechst^+/F4/80^+$), and M2 macrophages ($Hoechst^+/F4/80^+/CD206^+$) at day 7 and 84 after SCI (Fig. 3.9 C and D). The number of $CD206^+$ cells was significantly

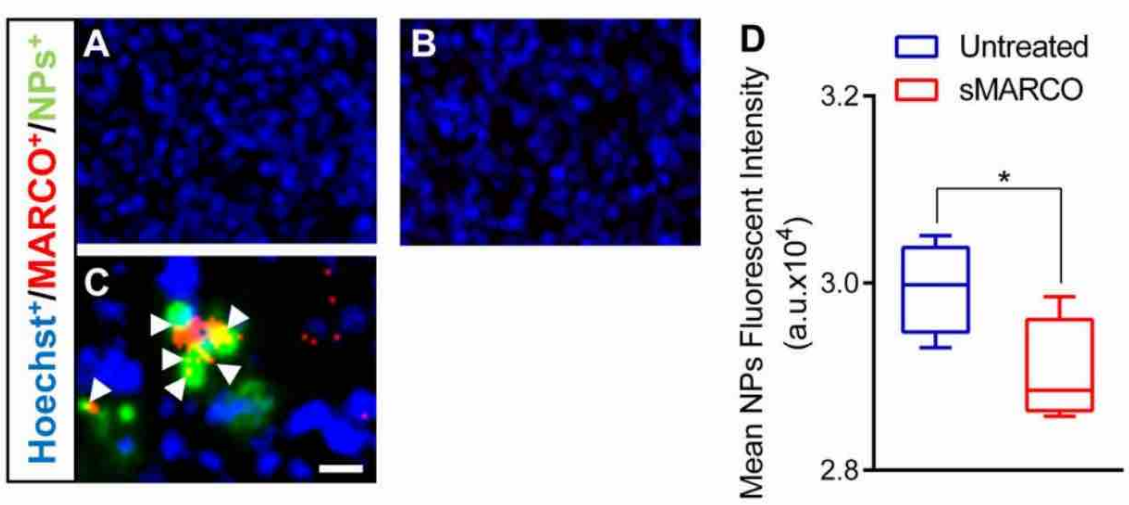

Figure 3.8: **NPs colocalization and internalization with MARCO$^+$ cells in the spleen.** (A)-(C) Spleen tissue sections were labelled for Hoechst (blue), anti-MARCO (red), and NPs (green) from (A) naïve, (B) PBS injection, and (C) NPs injection conditions at day 7 post-SCI.NP-Cy5.5 were colocalized with MARCO$^+$ cells (yellow) within the spleen in NPs group (scale bar: 100 μm). (D)Bone marrow derived macrophages were incubated with Cy5.5-NPs and 100 μg/ml of soluble MARCO (sMARCO)in cell culture media. The mean NPs fluorescent intensity was investigated using flow cytometry. The data indicated that sMARCO significantly reduced NPs internalization. Unpaired T-test was performed, where *P<0.05, n=4/group.

increased in the NPs compared with PBS group (Fig. 3.9F). The density of prore-generative M2 macrophages was about 2-fold up-regulated for the NPs group at day 7 and 84 after SCI (Fig. 3.9G). Furthermore, no statistical difference was noted in the total number of infiltrated macrophages for all conditions (Fig. 3.9E) over time, thus the ratio of M2 phenotypes to the total number of macrophages was substan-tially up-regulated in NP group (Fig. 3.9H). Therefore, NP administration influences macrophage polarization at the SCI.

3.4.3 NP Treatment Decreases Scarring Formation after SCI

SCI results in formation of both fibrotic and gliotic scar tissues at the lesion epi-center; we therefore investigated the impact of the NPs on these parameters. The scar tissue acts as a mechanical barrier to axon elongation and inhibiting axonal regener-

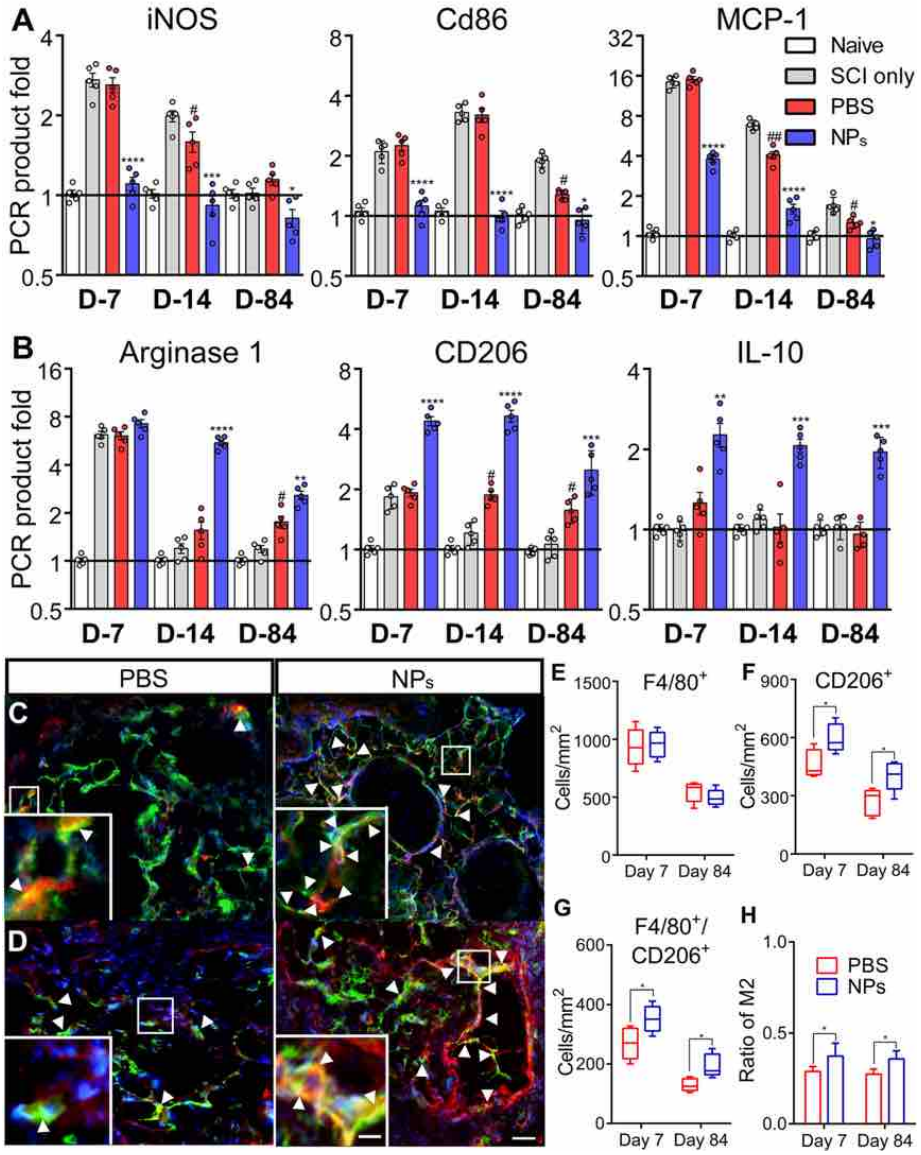

Figure 3.9: **Immunomodulation and macrophages polarization by NPs.** (A) and (B) qRT-PCR data indicate modulation of selected proinflammatory (A) and antiinflammatory (B) markers at day 7, 14, and 84 after SCI by NP treatment. A 2-way ANOVA with Tukeys post hoc test for the multiple comparisons, where ^{a}P<0.05, ^{b}P<0.01, ^{c}P<0.001, and ^{d}P<0.0001, compared with PBS group and P¡0.05 and P<0.01 relative to SCI only group, mean ± SD, n=5 per group and time point. (C) and (D) Immunodetection of M2 ($CD206^+/F4/80^+/Hoechst^+$; red, green, and blue, respectively) macrophages (yellow), (white arrowheads) within bridge from all conditions at day 7 (C) and day 84 after SCI (D). (Inset) High-magnification image of M2 within bridge area. (E) The density of total $F4/80^+$ macrophages within the bridge. No changes were observed between groups. (F) The quantitative analysis of $CD206^+$ cells. NPs up-regulate the expression of $CD206^+$ cells. (G) The density of M2 by NPs. (H) The ratio of M2 to the total number of macrophages. A 2-way ANOVA with Tukeys post hoc test for the multiple comparisons, where *P<0.05 compared with PBS group, mean ± SD, n=5 per group and time point. (Scale bars: C and D, 100 μm; C and D Inset, 50 μm.)

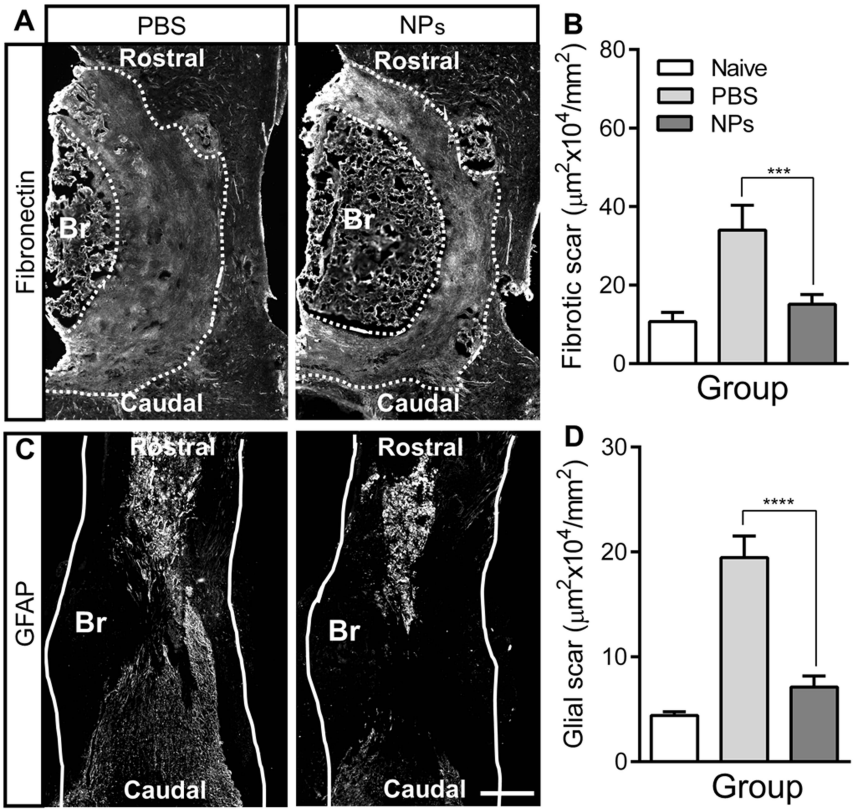

Figure 3.10: **NP treatment reduces the fibrotic and gliotic scarring after SCI.** (A) and (C) Spinal cord tissues were stained with anti-fibronectin (A) and anti-GFAP (C) using longitudinal sections from 4 wk after SCI (Br, bridge); dashed line indicates the area of fibrotic scar tissue around bridge and white line indicates host spinal cord. (Scale bar: 400 μm.) (B) and (D) Quantification of fibrotic (B) and glial (D) scarring around implanted bridge area. No differences were observed between the nave and NP group. The area of both fibrotic and glial scar was substantially decreased by NP treatment. A one-way ANOVA with Tukeys post hoc test for the multiple comparisons, where ***P<0.001 and ****P<0.0001 compared with PBS group, meanSD, n=5 per group and time point.

ation through accumulation of inhibitory molecules as a chemical barrier [34, 35]. A fibrotic scar is characterized by accumulation of fibronectin, fibroblasts, and various extracellular matrix molecules. Reactive astrocytes play prominent roles in formation of gliotic scar and act as a major impediment to axonal regeneration [35]. At 4 wk after SCI, the area of fibrotic scar tissue in the NP treatment group was decreased more than 2-fold compared with PBS (Fig. 3.10 A and B). Similar to the level of fibronectin, the area of glial fibrillary acidic protein (GFAP) staining in the NP group

was also substantially decreased 2- to 3-fold relative to the PBS group (Fig. 3.10 C and D). No differences were observed compared with naïve group (Fig. 3.11). These data indicate that NP administration significantly decreased both fibrotic and gliotic scarring after SCI.

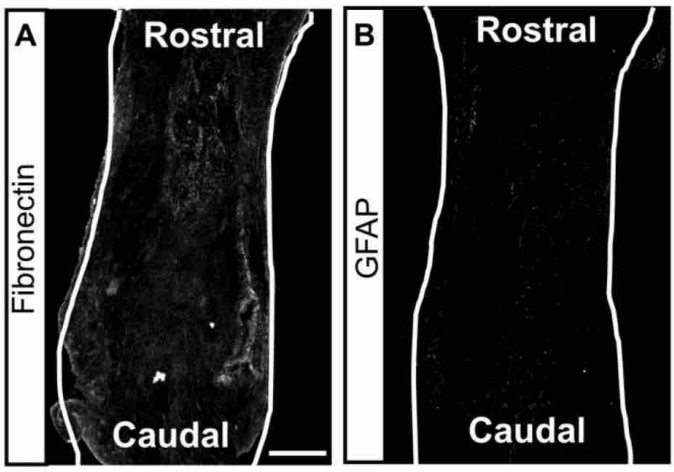

Figure 3.11: **Uninjured spinal cord tissues were labelled with anti-fibronectin (A) and anti-GFAP (B)** using longitudinal sections from 4 weeks after SCI (the white line indicates host spinal cord, scale bar=400 μm).

3.4.4 NPs Enhance Axonal Regrowth and Remyelination within an Implanted PLG Bridge

We investigated the impact of NP treatment on axonal regrowth and myelination in the chronic (day 84 after SCI) phase of SCI (Fig. 3.12). Spinal cord sections were stained using neurofilament 200 (NF200), myelin basic protein (MBP), and myelin protein zero (P0). Immunofluorescence data indicated that axons were observed throughout the bridges in all conditions (Fig. 3.12 A and B and Fig. 3.13). High magnification images showed that regenerating axons were found in bundles within the bridge (Fig. 3.12 A and B). NP administration substantially increased the number of $NF200^+$ axons relative to the PBS group (Fig. 3.12C). Similar to $NF200^+$ axons number, all myelinated axons ($NF200^+/MBP^+$) were increased 3-fold

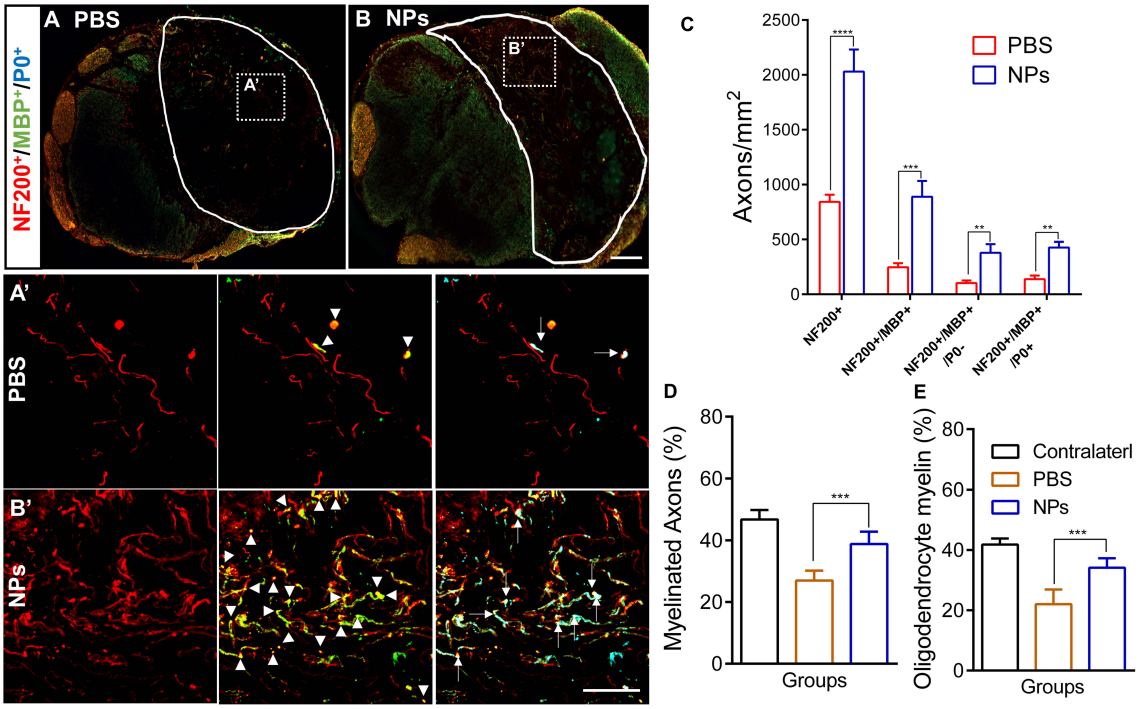

Figure 3.12: **NPs improve the axonal regrowth and remyelination in the chronic SCI phase.** (A and B) Spinal cord sections were labeled using NF200 (axons), MBP (all myelination), and P0 (Schwann cells derived myelination) from PBS (A) and NP (B) conditions at the rostral location. The line indicated the bridge area for quantification and dashed line is for higher magnification area in A' and B'. White arrowheads show all myelinated axons ($NF200^+/MBP^+$), and white arrows indicate Schwann cell-derived myelinated axons ($NF200^+/MBP^+/P0^+$). (C) Quantification of tothnnal number of $NF200^+$, $NF200^+/MBP^+$, $NF200^+/MBP^+/P0$ (oligodendrocyte-mediated myelinated axons), and $NF200^+/MBP^+/P0^+$. (D) Proportion of axons that was myelinated within the bridge area. (E) Percentage of axons that was myelinated by oligodendrocytes. A 2-way ANOVA with Tukey's post hoc test for the multiple comparisons were performed where **P<0.01, ***P<0.001, and ****P<0.0001 relative to PBS group, meanSD, n=5 per group. (Scale bars: A and B, 300 μm; A' and B', 100 μm.)

in response to NPs relative to PBS injection. In addition, the significantly greater number of oligodendrocyte- ($NF200^+/MBP^+/P0$) and Schwann cell-derived myelinated ($NF200^+/MBP^+/P0^+$) axons were observed for NP treatment relative to the PBS group. Furthermore, about 43% of the $NF200^+$ axons were myelinated in the NP condition, with 40% of those axons myelinated by oligodendrocytes, which were similar to those in uninjured contralateral side (Fig. 3.12 D and E). Collectively, these data suggest that NPs produce an environment more permissive to axonal

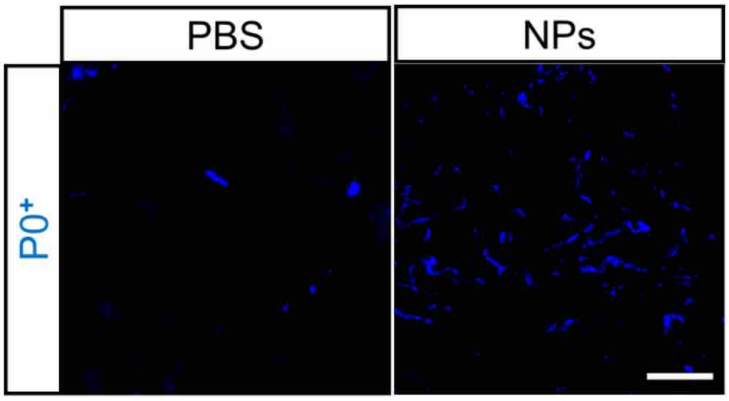

Figure 3.13: **Higher magnification area in figure 3.12A' and 3.12B'.** Spinal cord sections were stained with P0 (Schwann cells derived myelination) from both PBS and NPs groups. Scale bar; 50 μm.

growth and remyelination after SCI.

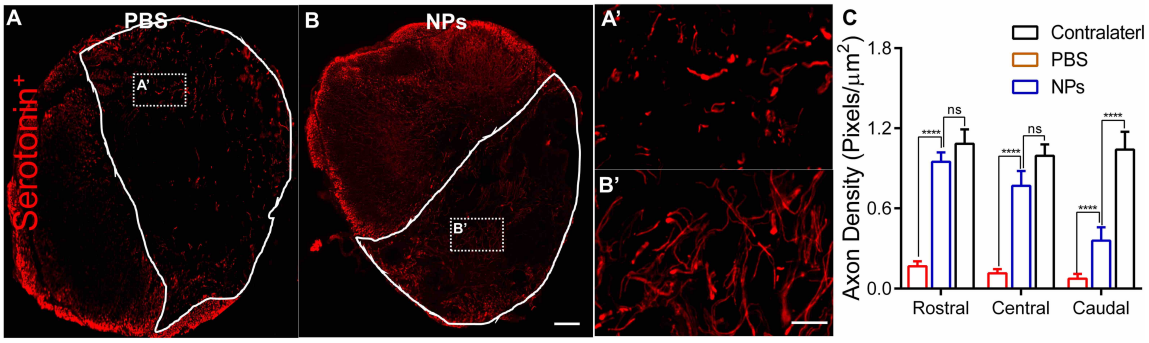

Figure 3.14: **Density of serotonergic fibers by NPs.** (A) and (B) Spinal cord sections were labeled for serotonin from PBS (A) and NP (B) conditions at the rostral location in the chronic SCI phase. The line indicated the bridge area for quantification and dashed line is for higher magnification area in A and B. (C) Quantification of serotonergic axonal density in the bridge at rostral (0-400 μm), central (400-800 μm), and caudal (800-1,200 μm) locations from the rostral edge of the bridge/tissue interface. A 2-way ANOVA with Tukey's post hoc test for the multiple comparisons, where ****P<0.0001 compared with PBS group, mean ± SD, n=5 per group. (Scale bars: A and B, 300 μm; A and B, 100 μm.)

3.4.5 NPs Increase the Density of 5-Hydroxytryptamine Fibers after SCI

The presence of axons that are positive for the neurotransmitter serotonin (or 5-hydroxytryptamine [5-HT]) was assessed because these axons have been associated with recovery of function and attenuation of allodynia/hyperalgesia after SCI [55, 56]. This role of 5-HT axons in function makes it a good marker for regeneration of

descending tracts. Spinal cord tissues were immunostained for 5-HT at day 84 after SCI, and the densities of 5-HT fibers quantified at 3 distinct locations of the bridge: rostral, central, and caudal (Fig. 3.14 and Fig. 3.1C). 5-HT fibers were identified throughout the bridge; however, about 5 to 9 times greater density of 5-HT fibers was observed with NP treatment in all 3 locations compared with PBS (Fig. 3.14 A, B, and C). Although data showed a trend toward greater intensity of 5-HT at rostral and central locations in contralateral side relative to NPs, no significant changes were observed between groups. These data suggest that in addition to the observation of neurofilament axons and active remyelination within the bridge, NP treatment specifically resulted in the growth of descending motor axons as assessed by density of 5-HT fibers within the bridge.

3.4.6 NPs Improve Locomotor Function after SCI

We next investigated the expression of regeneration-associated genes (RAGs) following NP administration in the acute and chronic SCI phase from the injured spinal cord tissue (Fig. 3.15 A and B). Genes were selected from neural system development (Gene Ontology [GO] accession no. GO:0007399), locomotor recovery- (GO:0007626), and chemical synaptic transmission- (GO:0007268) associated gene ontologies based on a previous study [53]. Gene expression data indicated that selected genes had up-regulated expression in the the NP group for both the acute and chronic phase of SCI relative to PBS injection. Interestingly, in the chronic SCI phase, expression levels of RAGs (ChAT, Hoxd10, and Lhx5) in the PBS injection group were also statistically up-regulated relative to SCI only group, suggesting a role for the bridge alone in supporting regeneration. Subsequently, ipsilateral hindlimb locomotor recovery was assessed through the Basso Mouse Scale (BMS) before injury, at day 3, and weekly for 84 d after SCI (Fig. 3.15C). All animals exhibited normal

open field locomotion before SCI (BMS;9). No ipsilateral hindlimb movement was observed at day 3 after SCI in any treatment group (BMS;0). However, BMS scoring in the NP group revealed a substantially improved locomotor function compared with the PBS group from day 7 through day 84 after SCI. In agreement with gene expression data, the BMS score in PBS group was significantly increased relative to the SCI-only group from day 70 after SCI, indicating that the bridge itself also has a positive effect on locomotor recovery. These data demonstrate that NPs have an early effect on reprogramming of circulating immune cells, which synergize with the microenvironment created by the bridge to induce long-term expression of RAGs at the injury, resulting in a proregenerative microenvironment that is associated with an improved locomotor function after SCI.

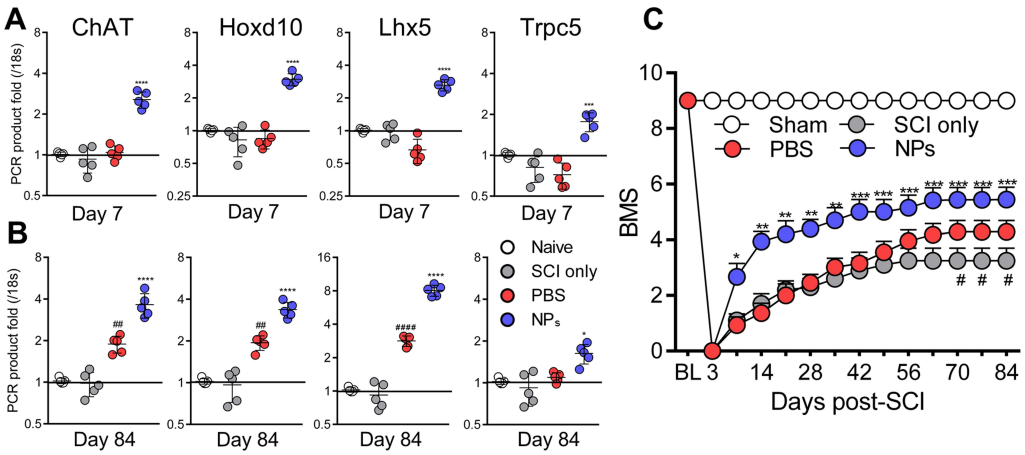

Figure 3.15: **Locomotor functional recovery by NPs.** (A and B) Regeneration associated genes were investigated via qRT-PCR in the acute (A) and chronic (B) SCI phase. A one-way ANOVA with Tukeys post hoc test for the multiple comparisons, where *P<0.05, ***P<0.001, and ****P<0.0001 compared with PBS group, P<0.01 and P<0.0001 relative to SCI only, meanSD, n=5 per group. (C) The ipsilateral hindlimb locomotor function was assessed using the BMS weekly for 84 d after SCI. NPs enhance the locomotor function following SCI. BL, baseline. A 2-way ANOVA with Tukeys post hoc test for the multiple comparisons, where, *P<0.05, **P<0.01, and ***P<0.001, compared with PBS group and ˆP<0.05 relative to SCI only, mean ± SD, n=18 per group and time point.

3.5 Discussion

In the present study, we investigated the potential for reprogramming of circulating innate immune cells through NP administration to enhance functional regeneration following SCI. When innate immune cells are activated in the blood and spleen, they have high phagocytic capacity for scavenging apoptotic cells, cellular debris, and foreign invasive materials [57, 58]. Generally, NPs may be perceived by inflammatory monocytes and neutrophils as foreign material and are then rapidly internalized [46, 59, 60]. The rapid infiltration of various immune cells including inflammatory monocytes and neutrophils into the SCI leads to inflammatory response-derived secondary damage, contributing to further neuronal cell death, axonal dieback, demyelination, and scar tissue formation [37, 61]. For *in vivo* SCI treatment, systemic depletion of immune cells has led to mixed results with some studies showing improved regeneration with partial depletion of select immune populations, while other studies show worsened histological and functional outcomes with complete depletion of certain immune populations [61]. Herein, we focused on a nondepleting strategy targeting inflammatory cells in the vasculature, before their extravasation to the injury. We tested the hypothesis that particles could reprogram innate immune cell trafficking and phenotype to limit deleterious inflammatory responses, and promoting an environment that is a more permissive for regeneration.

i.v.-delivered NPs influence trafficking patterns of inflammatory monocytes and neutrophils, with a modest proportion of NP-positive cells trafficking to the spinal cord and the majority accumulating in the spleen. The spleen plays substantial roles in coordinating inflammatory responses and restoring immune homeostasis that lead to functional recovery after SCI [62]. i.v.-administered NPs are thought to bind to cir-

culating immune cells via scavenger receptors such as MARCO. NPs with a diameter of 500 nm were selected based on our previous work with autoimmune disease [63] and a greater internalization due in part to binding affinity for immune cells and flow patterns within the blood [45]. Previous studies reported that neither resident microglia nor T lymphocytes express scavenger receptors such as MARCO [64], thus indicating that NPs target selectively circulating immune cells that would normally infiltrate a SCI. In agreement with previous studies, *in vitro* studies have demonstrated that NPs were internalized by bone marrow-derived macrophages (Fig. 3.8) [45, 50]. The sequestration of inflammatory monocytes/neutrophils in the spleen has been observed in other inflammation-mediated diseases models by NP treatment [45, 46, 48]. In agreement with these previous studies, NPs reduced the number of inflammatory monocytes/neutrophils in the injured spinal cord, with this decrease likely indirectly decreasing tissue degeneration due to the reduced immune cell infiltration. However, we observed that NP-positive cells were present within the spinal cord, and our data suggest that these cells directly influenced the microenvironment by inducing a proregenerative phenotype that was more permissive for tissue regeneration. These results are also supported by gene expression analysis (Fig. 3.6). In particular, both human and mice inflammatory monocytes express CCR2, which is principally responsible for recruitment and accumulation of these cells at inflammatory sites [45, 65]. Previous study showed that delivery of CCR2 small interfering RNAs via liposome-reduced inflammatory monocyte trafficking in inflammatory disease models [65]. However, because of widespread expression of CCR2 in other immune cells such as B cells and T cells, targeting CCR2 may have undesired side effects [66].

The cumulative effect of NP treatment is modulation of the microenvironment, which induces macrophage polarization from a proinflammatory phenotype toward

a proregenerative phenotype. In the intact CNS, microglia/macrophages have both M1 and M2 properties; however, following SCI, proregenerative M2 macrophages are typically decreased, while pathological M1 phenotypes are increased and produce proinflammatory factors [54]. Therefore, a transient and low number of M2 phenotype cells at the injury may fail to control secondary inflammatory events following primary SCI. NP treatment modulated the microenvironment and led to an M2-enhanced environment at the SCI site, with down-regulation of proinflammatory factors and up-regulated expression of antiinflammatory factors such as Arg1, CD206, and IL-10 throughout day 84 after SCI. Interestingly, NP treatment also decreased the expression level of MCP-1, which is responsible for attracting circulating inflammatory monocytes to injuries by binding to its receptor CCR2 [45] and may also influence trafficking patterns of inflammatory monocytes after SCI. In addition, down-regulation of proinflammatory factors following NP treatment indicates that repeated-administration of NPs was well tolerated and reduced scar formation. Arg1 has been shown to promote wound healing and decrease the intensity and duration of inflammation [53]. Similarly, CD206 and IL-10 both have demonstrated roles in modulating immune responses and secondary damage after injury. CD206 binds and removes apoptotic and necrotic cells without generation of cytotoxic byproducts after injury [54]. The antiinflammatory cytokine IL-10 suppresses nuclear factor-κB (NF-κB) activation, leading to down-regulation of proinflammatory factors secretion [53]. Consistent with these roles, NP treatment up-regulated the number of $CD206^+$ cells and M2 macrophages ($CD206^+/F4/80^+$) compared with the PBS group.

NP treatment significantly reduced both fibrotic and gliotic scarring after SCI. Lesion scarring represents both a mechanical and chemical impediment to axonal outgrowth and regeneration, and previous studies have demonstrated that macrophages

lead to a profibrotic microenvironment by releasing proinflammatory factors. In both mice and human, these proinflammatory factors contribute to fibroblast activation and the induced secretion of connective tissue growth factor (CTGF) and collagen IV through SMAD2/3-mediated pathways, initiating formation of a dense, insoluble fibrotic matrix [67]. Additionally, prior reports demonstrate that both circulating immune cells and hematogenous-derived macrophages recruit perivascular fibroblasts at the SCI, while depleting of hematogenous macrophages decreases the fibroblast accumulation and fibrotic scar area, enhancing axonal regrowth [68]. In addition to fibrotic scarring, astrocytes also become reactive after SCI and are a major component of gliotic scarring. Reactive astrocytic responses are also initiated by proinflammatory factors that act through up-regulation of extracellular signal regulated kinase (ERK) signaling [41]. In this study, NP inhibition of immune cell accumulation, induction of proregenerative phenotypes, and generation of antiin flammatory factors at the injury site may have altered fibroblast migration and astrocyte-activation, reducing fibrotic and gliotic scarring and promoting axonal regeneration following SCI.

NP treatment has positive effects on axonal regeneration and remyelination after SCI. In the inflammatory microenvironment, proinflammatory factors are cytotoxic to neuronal cells and stimulate a short and arborizing growth pattern of axons after SCI [41, 54, 69]. NP administration promotes axonal regrowth throughout the implanted-multichannel bridges compared with PBS injection. In the data reported herein, NP treatment influences the gene expression dynamics and macrophages polarization at the injury. Increased Arg1 by NPs at the injury enhances overexpression of polyamines, promoting cAMP downstream signaling pathway to activate axonal regrowth even in a myelin inhibitory microenvironment [54, 70]. IL-10 has been re-

ported to up-regulate expression of antiapoptotic factors and provide a direct trophic effect on axonal regeneration under the neurotoxic microenvironment [53, 71]. CD206 promotes tissue remodeling after injury involving wound retraction and inflammatory resolution for tissue homeostasis [47]. All of these factors may contribute to creating a proregenerative environment after SCI leading to axonal regeneration. Axonal remyelination after SCI is considered as a major component of the regenerative process and is mediated by multipotent oligodendrocytes progenitor cells (OPCs). Previous studies have indicated that macrophages polarization into proregenerative M2 phenotypes is an essential step for differentiation of OPCs for remyelination after SCI [53, 72]. Moreover, an M2 mediated-regenerative factor activin-A directly binds to OPCs and facilitate OPC differentiation at the SCI [72, 73]. Therefore, NP treatment-mediated reprogramming of innate immune cells toward proregenerative phenotypes may be a key component of the regenerative process for axonal regeneration and remyelination after SCI.

The early effects of NP treatment synergize with multichannel bridge to up-regulate long-term expression of RAGs and enhance functional recovery after SCI. PLG has been widely used for nerve tissues repair [41, 52, 74], with PLG biodegrading slowly into lactic and glycolic acid that are readily cleared from the tissue, metabolized, and eliminated from the body as carbon dioxide and water via citric acid cycle [75]. Previously, we reported that bridge implantation alone increased the expression levels of axonal guidance-associated and synaptogenesis- associated gene ontologies at the SCI lesion [53], and altered the chemical balance and physical cues for a more permissive environment via infiltration of endogenous supportive cells, leading to release of factors for injury stabilization and attenuation of inflammatory responses [41, 52]. Furthermore, mechanical guidance by the 3D structure

of the bridge contributed to regeneration of descending axons and an increase in growth associated protein 43 (GAP-43) expression below the injury, leading to forelimb functional recovery [74]. In addition, the bridge contributes to reducing the extent of scar formation and astrogliosis [53, 53]. These characteristics of bridge implantation are consistent with the observed up-regulation of RAG expression and reduction of proinflammatory factors in our control group, which consisted of PBS injections in conjunction with bridge implantation. These results indicate that the bridge itself has the potential to support axonal regeneration via modest alteration of inflammatory responses and up-regulation of RAGs, leading to the locomotor functional recovery over the SCI-only group over time. BMS scores in the NP group were significantly increased starting from 1-wk after SCI compared with PBS, indicating that rapid NP-mediated inhibition of inflammatory immune cells accumulation led to less degeneration for rapid recovery of motor function. Furthermore, an improvement of locomotor skills was also observed from the PBS group at the chronic SCI phase compared with SCI only, which likely results from a more permissive environment enabling regeneration. These results were also supported by gene expression data. NP-derived immune cells modulation led to the long-term expression of multiple antiinflammatory factors and RAGs and induced a proregenerative environment at the injury. A number of genes associated with motor neurons were observed to be up-regulated at later time points. Choline acetyltranferase (ChAT), which marks mature motor neurons [76], had increased expression. Similarly, an increased expression of Homeobox D10 (Hoxd10) was observed, which organizes the patterning of motor neurons in the spinal cord [53]. LIM homeobox 5 (Lhx5), implicated in the proliferation and differentiation of motor neurons [61], and transient receptor potential channel subfamily C (Trpc5), which leads to differentiation of neural progenitor

cells [41, 42], were also up-regulated. Following SCI, descending serotonergic projections to spinal motor neurons were disrupted, leading to a decrease in serotonin levels and enhancing the locomotor dysfunction [55, 56]. Our data demonstrate that NP treatment up-regulates the number of 5-HT fibers within bridges, which also may contribute to locomotor recovery. Taken together, these data demonstrate that NP treatment has early and rapid therapeutic impacts, which have long-term consequences with multichannel bridges synergistically, contributing to immune cells reprogramming toward pro-regenerative phenotypes. In addition, these effects lead to the long-term up-regulation of antiinflammatory factors, RAGs, and serotonergic fibers, promoting locomotor recovery after SCI.

In conclusion, this report demonstrates that NP treatment can modulate the inflammatory microenvironment after SCI. NP-mediated rapid reprogramming of innate immune cells has a sustained impact on microenvironment modulation at the SCI injury when combined with bridge implantation. In addition, this regenerative microenvironment initiates a cascade of events, including induction of gene expression profiles associated with neural development and regeneration, which likely contributes to the enhanced numbers of regenerating and myelinated axons and improved functional recovery. Collectively, this strategy of targeting the innate immune cells in the vasculature before their extravasation to a SCI may have applications to other injury models associated with inflammation-mediated tissue damage. Furthermore, NPs are made of a Food and Drug Administration-approved material, stable at room temperature, do not contain an active pharmaceutical ingredient (API), and can be readily stored for immediate i.v. administration within the standard of therapy guidelines to limit secondary damage.

3.6 Materials and Methods

3.6.1 Multichannel bridges fabrication

Initially, Poly(D,L-lactide-co-glycolide)(PLG, 75:25 lactide:glycolide; i.v. 0.76 dL/g; Lakeshore Biomaterials, Birmingham, AL, USA) was dissolved in dichloromethane (6 % w/w) and emulsified in 1% poly(ethylene-alt-maleic anhydride) using a homogenizer (PolyTron 3100;Kinematica AG, Littau, Switzerland) to make microspheres (z-average diameter 1μ m). D-sucrose (Sigma Aldrich), D-glucose (Sigma Aldrich), and dextran MW 100,000 (Sigma Aldrich) were mixed at a ratio of 5.3:2.5:1 respectively by mass then were caramelized, cooled, and drawn from solution using a Pasteur pipette to create sugar fibers. These fibers were coated mixture of PLG microspheres and salt (with a 1:1 ratio), then pressed into a salt-lined aluminum mold. Subsequently, it was equilibrated, and gas formed with high pressure of CO_2 gas (800 psi) for 16 h in a custom-made pressure vessel. The pressure was released over a period of 40 min, which fused adjacent microspheres to produce a continuous polymer structure. The bridges were cut into 1.2mm sections, and the porogen was leached in water for 2 hours, then the bridges were dried over-night and stored in a desiccator (Fig. 3.1A).

3.6.2 Nanoparticle fabrication and injection

First, 50:50 PLG (inherent viscosity = 0.55dL/g) was purchased from Absorbable Polymers (Birmingham, AL), and conjugated with Cyanine 5.5 amine dye (Lumiprobe corporation, Cockeysville, MD) using a N-(3-Dimethylaminopropyl)-N-ethylcarbodiimide hydrochloride (EDC) (Sigma-Aldrich, St. Louis, MO)/ N-hydroxysuccinimide (NHS)(Thermo Fisher Scientific, Waltham, MA) chemistry. Then, 50:50 PLG particles were fabri-

cated using an oil-in-water single emulsion solvent evaporation method. Briefly, 50:50 PLG polymer and the polymer conjugated with cyanine 5.5 dye were dissolved in dichloromethane. Then, the mixture was added to Poly (ethylene-alt-maleic anhydride) (Polyscience, Inc., Warrington, PA) solution, sonicated using a Cole-Parmer CPX130 Ultrasonic Processor (Vernon Hills, IL), and stirred overnight to remove organic phase. The resulting polymeric particles were washed three times and lyophilized with combination sucrose and D-mannitol (Sigma-Aldrich, St. Louis, MO). For the injections, PLG particles were resuspended in PBS at a concentration of 5 mg/ml and aggregates were removed with a 35 μm mesh filter. Each animal received 1 mg of particles (200 μl of suspension) via tail veil injection within two hours after SCI per day for 7 days. The same volume of PBS was injected as a control.

3.6.3 Spinal cord hemisection injury model and animal care

All animal surgery procedures and animal care were conducted according to the Animal Care and use Committee guideline at University of Michigan. The impact of NPs on biodistribution, inflammatory responses, and locomotorregeneration was assessed after SCI within five treatment groups: i) Nave (normal health animal), ii) Sham (laminectomy only), iii) SCI only (without bridge implantation), iv) PBS (SCI + bridge + PBS injection), and v) NPs (SCI + bridge + NPs injection)(Table 3.1) and immunofluorescence was investigated with; i) Naïve, ii) PBS (SCI + bridge + PBS), and NPs (SCI + bridge + NPs) (Table 3.2). A mouse hemisection SCI model was performed as described previously [53](1). Briefly, C57/BL6 female mice (6-8 weeks old; Jackson Laboratory, Bar Harbor, ME, USA) were anesthetized using isoflurane (2%). A dorsal laminectomy was performed at T9-T10 level then a 1.2 mm long lateral of the midline spinal cord segment was cut and removed to generate a

hemisection SCI model. Bridges were implanted in the injury site and covered using Gelform (Pfizer, New York, NY, USA) (Fig. 3.1B). Muscle was sutured together, then the skin was stapled. The animals were placed on a heating pad for recovery. For post-operative animal care, Baytril (enrofloxacin 2.5 mg/kg, once a day for 2 weeks), buprenorphine (0.1 mg/kg, twice a day for 3 days), and lactate ringer solution (5 mL/100 g, once a day for 5 days) were administrated subcutaneously. Bladders were manually expressed until bladder reflexive function was observed twice a day.

	Naïve	Sham (laminectomy only)+NPs	SCI only	PBS (SCI+bridge+PBS)	NPs (SCI+bridge+NPs)
IVIS	10	10	-	-	15
qRT-PCR	20	-	20	20	20
BMS	-	18 (without NPs injections)	18	18	18

Table 3.1: **All experimental groups and total number of animals**

	Naïve	PBS (SCI+bridge+PBS)	NPs (SCI+bridge+NPs)
7/4	10 (Contralateral)	10	10
Macrophage polarization	-	10	10
Scar formation	5	5	5
Axonal regrowth and Remyelination	5 (Contralateral)	5	5
5-HT	5 (Contralateral)	5	5

Table 3.2: **All experimental groups and total number of animals for IHC**

3.6.4 *In vivo* bio-distribution of Nanoparticle

For the *in vivo* biodistribution of NPs study, animals were administered via tail vein with 200 μl of 5mg/ml Cy5.5 conjugated NPs every day for 7 times. 1, 3, and 7 days after injection, animals were euthanized, and tissues were dissected from spinal cord and spleen. Each tissue was imaged using an IVIS Lumina LTE camera system (Caliper Life Sciences, Hopkinton, MA). The region-of-interest values from

each organ were recorded as photon flux in total photon count per cm^2 per steradian.

3.6.5 RNA isolation and Quantitative Reverse-Transcriptase PCR

Initially, the spinal cord tissues were removed from all conditions. The spinal cord tissues were removed and cut into about 2 mm segments centered on 1.2 mm of bridge region; samples were not pooled. Next, samples were homogenized using 1 mL of Trizol reagent (Invitrogen, Carlsbad, CA) with a glass tissue grinder. Samples were not pooled. RNA isolation was followed by chloroform extraction and isopropanol precipitation [42]. The concentration of RNA was measured using NanoDrop 2000C (Thermo Scientific, Newark, DE). Next, we conducted the quantitative Reverse-Transcriptase PCR (qRT-PCR) using spinal cord for the gene expression analysis over time. cDNA was synthesized using iScript^{TM} cDNA Synthesis kit (Bio-Rad, Hercules, CA). Primers were designed for qRT-PCR (Table 3.3) [53, 38, 39]. The qRT-PCR products were assessed using the accumulation level of iQ^{TM} SYBR Green Supermix (Bio-Rad) fluorescence following a manufacturers protocol on CFX Connect^{TM} Real-Time PCR Detection System (Bio-Rad). The gene expression level was normalized by the expression of 18s-rRNA and differences in gene expression were presented as fold ratios from control group. Relative quantification was calculated as X = 2 $\Delta\Delta$Ct, where $\Delta\Delta C_t = \Delta E \Delta C_t$ and $\Delta E = C_{t,exp} C_{t,18s-rRNA}$, $\Delta C_t = C_{t,control} C_{t,18s-rRNA}$ [77]. All qRT-PCR values were expressed as the log2 transformed after normalization to the housekeeping gene 18s-rRNA and +1 was marked as cut-off value for upregulation.

Gene	Accession number	Forward (5'-3')	Reverse (5'-3')
Arginase1	U51805.1	GAACACGGCAGTGGCTTTAAC	TGCTTAGCTCTGTCTGCTTTGC
CD206	NM_008625.2	TCTTTGCCTTTCCCAGTCTCC	TGACACCCAGCGGAATTTC
IL-10	NM_010548.2	ATGCAGGACTTTAAGGGTTACTTGG GTT	ATTTCGGAGAGAGGTACAAACGAGGT TT
iNOS	U58677.1	CCCTTCAATGGTTGGTACATGG	ACATTGATCTCCGTGACAGCC
Cd86	NM_019388.3	TTGTGTGTGTTCTGGAAACGGAG	AACTTAGAGGCTGTGTTGCTGGG
MCP-1	NM_011333.3	GCCAACTCTCACTGAAGCCA	TGCTGCTGGTGATCCTCTTG
Chat	NM_009891.2	GGCTTTTGTGCAAGCCATGA	CACAGGGCCATAACAGCAGA
Hoxd10	NM_010462.5	TGTACAGTGCAGAGAAGCGG	GTGTCTGGACTGGAGTCTGC
Lhx5	NM_008499.5	CAGGATCCGTTACAGGACGA	AACCACACCTGAATGACCCT
Trpc5	NM_009428.3	AACTCCCTCTACCTGGCAAC	TTCTGCAATCAGAGTCGGGT
18s-rRNA	NR_003278.3	GCAATTATTCCCCATGAACG	GGCCTCACTAAACCATCCAA
Cd11b	NM_008401.2	AAGCAGCTGAATGGGAGGAC	TAGATGCGATGGTGTCGAGC
Ly6G	NM_0013104 38.1	GAGCAATCTCTGCCTTCCCA	AGGAGTGGGGTGCCTATACA
Ccr2	NM_009915.2	AACAGTGCCCAGTTTTCTATAGG	CGAGACCTCTTGCTCCCCA
Ly6c	NM_0012520 57.1	GACAGAACTTGCCACTGTGC	GCTGGGCAGGAAGTCTCAAT

Table 3.3: **Primer sequences for qRT-PCR**

3.6.6 Nanoparticles internalization

Bone marrow derived macrophages (BMDMs) were generated as previously reported [78]. BMDMs (0.5 million/well) were plated in 12-well plates. Cy5.5-NPs were incubated in cell culture media for 30 min and incubated in 100 μ g/mL of soluble MARCO (sMARCO, Recombinant mouse MARCO, R&D system, Minneapolis, MN) for 45 min. Then, 100 μg/mL of sMARCO treated particles were added to each well and cultured for 2 hours. Cells were harvested, blocked with TruStain FcX^{TM} (anti-mouse CD16/32, BioLegend, San Diego, CA) and stained with fluorochrome-conjugated antibodies (BV650 Rat Anti-Mouse CD11b and BV510 Rat Anti-Mouse CD45, BD Biosciences, San Jose, CA). Data was acquired with a flow cytometry (LSRFortessa, BD Biosciences) and analyzed with FlowJo software (BD Biosciences).

3.6.7 Behavioral test for locomotor function

Locomotor functional recovery in the ipsilateral hindlimb after SCI was accessed using open field Basso Mouse Scale (BMS) locomotor rating scale with a score from 0 (no movement) to 9 (normal gait) [79]. The score is based on the ipsilateral hindlimb locomotor ability of SCI mice. SCI mice (n=18/group) were observed in an open field for 4 minutes after they had gently adapted to the field. Only the ipsilateral hindlimb side was assessed at days 3 and then weekly after SCI for 12 weeks. The score was obtained by taking an average value of results from each experimental group. A baseline (BL) was determined at day 7 and 1 prior to the SCI. Animals were randomly assigned to treatment group and assessment was performed by researchers blinded to the group.

3.6.8 Tissue processing and immunofluorescence

Spinal cord tissues were collected at 1, 4, and 12 weeks after SCI. Those tissues were then snap frozen in isopentane and embedded in Tissue Tek O.C.T compound (Sakura Finetek, Torrance, CA, USA) with 30% sucrose. Samples were cryosectioned in 18 μm transversely or in 12 μm longitudinally. All primary and secondary antibodies were provided in Table 3.4. The number of immune-positive cells were manually counted and done under blinded conditions. Multiple markers by co-staining was examined by evaluating pixel overlap of different channels in NIH ImageJ (Bethesda, MD, USA). Nonadjacent nine spinal cord tissues were selected randomly from three distinct locations at caudal (0-400 μm), central (400-800 μm), and rostral (800-1200 μm) from the caudal edge of the bridge/tissue interface (total 27 tissues were assessed per animal) (Fig. 3.1C). The accumulated inflammatory monocytes/neutrophils were

identified by co-labelling Hoechst$^+$ to 7/4 immunoreactive cells from day 7 and 10 following SCI within a bridge and from day 7 within the spleen. The percentage of 7/4$^+$ inflammatory monocytes/neutrophils that was co-labeled with NPs-Cy5.5 was determined from the ratio of the number of Hoechst$^+$/7/4$^+$/NP$^+$ cells divided by the number of Hoechst$^+$/7/4$^+$ cells within the bridge area. The total number of macrophages and pro-regenerative M2 macrophages within a bridge area were evaluated by determining Hoechst$^+$/F4/80$^+$ cells and Hoechst$^+$/F4/80$^+$/CD206$^+$ cells. Macrophages were identified by localizing Hoechst$^+$ staining to F4/80$^+$ immunoreactive and labeling them in ImageJ. Then, cell numbers were normalized to the counted area in each tissue section. To investigate the numbers of regenerated and myelinated neurofilaments, we used NF200$^+$, NF200$^+$/MBP$^+$, and NF200$^+$/MBP$^+$/P0$^+$ axonal fibers to identify the numbers of axons, all myelinated axons, and myelinated axons by infiltrating Schwann cells, respectively. The percentage of myelinated axons was determined from the ratio of the number of myelinated axons (NF200$^+$/MBP$^+$) divided by the number of axons (NF200$^+$) within the bridge area. To determine the source of the myelination, we performed triple staining of NF200, MBP and P0. NF200$^+$/MBP$^+$/P0$^-$ neurofilaments were considered as oligodendrocyte-derived myelination. The fraction of oligodendrocyte-derived myelination was calculated as NF200$^+$/MBP$^+$/P0$^-$ divided by NF200$^+$/MBP$^+$. To evaluate fibrotic and glial scarring area around implanted multichannel bridges, nine nonadjacent sagittal sections were selected randomly from each animal and condition, and the area of fibrotic and gliotic scarring around the implanted bridge was investigated. The immunofluorescence images were converted to black and white then a standardized optical density threshold to each image was applied. ImageJ was used to measure the amount of stained area around the implanted bridges. To investigate the intensity of serotoner-

gic fibers, total labelled pixels of serotonin labeled axons within the bridge area were quantified and divided by the bridge area to obtained mean serotonergic axon density. Uninjured contralateral spinal cord tissues were obtained from PBS and NPs injection groups and the density was obtained by taking an average value of results. All tissues were imaged on an Axio Observer Z1 (Zeiss, Oberkochen, Germany) using a 10x or 20x/0.45 M27 apochromatic objective and an ORCA-Flash 4.0 V2 Digital CMOS camera (C11440-22CU, Hamamatsu Photonics, Hamamatsu City, Shizuoka, Japan).

Name	Company	Catalog number	Concentration
anti-CD206	Abcam	ab195192	1:200
F4/80	AbD Serotec	MCA497GA	1:200
7/4	Bio-Rad	MCA771GA	1:200
Neurofilament 200	Sigma Aldrich	N4142	1:200
anti-MARCO	Bio-Rad	MCA1849	1:200
Myelin Basic Protein	Santa Cruz Biotech	SC-13914	1:500
P-zero myelin protein	Aves Labs	PZO	1:250
anti-fibronectin	Sigma Aldrich	F7387	1:200
anti-GFAP	Abcam	ab53554	1:500
anti-serotonin	Abcam	ab66047	1:400
Hoechst 33258	Fisher	H3569	1:2000
AlexaFluor 488 AlexaFluor 555, and AlexaFluor 647	Fisher	A-21429, A-21424, A-11055, A-21432, A-21447, and A-31571	1:1000

Table 3.4: **Primary and secondary antibodies for immunofluorescence**

3.6.9 Statistical analysis

A one or two-way ANOVA and Tukey's post hoc test for the multiple comparisons, and Students t test were used for the statistical analysis. We performed the Kolmogorov-Smirnov normality test [80]. P-value (alpha) 0.05 was used as a cut-off such that P-values larger than 0.05 are considered as passing the normality test. To achieve reasonable statistical power analyses, type II errors were controlled at 0.2 level for all the statistical tests and α=0.05. Equal variance (ANOVA Model) was validated and assumed for each study. Given the above parameters, a conservative

effect size was 0.25 for appropriate sample size for each study and all statistical analysis were performed using G* Power Software [53], OriginPro (OriginLab Corporation, Northampton, MA, USA), and Prism 6 (GraphPad Software, La Jolla, CA, USA). $P<0.05$ was considered as statistically significant and the all values were expressed in mean $\pm$ standard deviation (SD).

CHAPTER IV

Therapeutic Benefit of Cargo-Free Immunomodulatory Nanoparticles Combined with Anti-PD-1 Antibody

4.1 Authors

Yining Zhang, Kevin R. Hughes, Jacqueline S. Jeruss, and Lonnie D. Shea

4.2 Abstract

The presence of immunosuppressive innate immune cells such as myeloid derived suppressor cells (MDSCs), Ly6C-high monocytes, and tumor-associated macrophages (TAMs) at a tumor can inhibit effector T cell and NK cell function. Immune checkpoint blockade using anti-programmed death 1 (PD-1) antibody aims to overcome the immune suppressive environment, yet only a fraction of patients respond. Herein, we test the hypothesis that cargo-free poly(lactide-co-glycolide) (PLG) nanoparticles administered intravenously can divert circulating immune cells from the tumor microenvironment to enhance the efficacy of anti-PD-1 immunotherapy in the 4T1 mouse model of metastatic triple-negative breast cancer. *In vitro* studies demonstrate these nanoparticles decrease the expression of monocyte chemoattractant protein 1 (MCP-1) by 5-fold and increase the expression of tumor necrosis factor alpha (TNF-α) by more than 2-fold upon uptake by innate immune cells. Intravenous

administration of particles results in internalization by neutrophils and monocytes, with particles arriving in the liver, lung, spleen, and primary tumor. Nanoparticles and anti-PD-1 antibody combination therapy significantly slowed tumor growth and prolonged survival, while neither monotherapy did. Nanoparticle delivery decreased the abundance of MDSCs in circulation and in the lung, the latter being the primary metastatic site in the 4T1 model. Gene expression analysis by Gene Set Enrichment Analysis (GSEA) indicated that inflammatory myeloid cell pathways were down-regulated in the lung and upregulated in the spleen and tumor. Upregulation of extrinsic apoptotic pathways was also observed in the primary tumor. Collectively, these results demonstrate that cargo-free PLG nanoparticles can reprogram immune cell responses and alter the tumor microenvironment *in vivo* to overcome the local immune suppression attributed to myeloid cells to enhance the efficacy of anti-PD-1 therapy.

4.3 Introduction

Tumor growth and metastatic progression are aided in part by the function of innate immune cells, which can be induced toward an immune suppressive function by tumor-secreted factors [4]. Disease-induced cell types found at the primary tumor or metastatic niche include inflammatory monocytes ($CD11b^+$ $Ly6C^{hi}$ cells in mice), tumor-associated macrophages (TAMs), and myeloid-derived suppressor cells (MDSCs). Circulating inflammatory monocytes differentiate into tumor-associated macrophages (TAMS) in tissues, which have immunosuppressive phenotypes and induce angiogenesis to aid metastasis [81, 82]. Additionally, myeloid cell recruitment has been shown to be critical for pre-metastatic niche development prior to

metastatic cell colonization [6]. MDSCs are a class of neutrophil that has been implicated in aiding tumor growth and metastasis, especially to the lung [5, 28]. These cells normally serve to regulate the immune response to pathogens, but in the context of cancer, MDSCs secrete immunosuppressive cytokines and reactive oxygen species (ROS) to inhibit anti-tumor T cell and NK cell function [7]. These cells contribute to the failure of immune checkpoint blockade or T-cell immunotherapies [83].

The immunosuppression and pro-tumor functions of myeloid cells have been the targets of numerous therapies to alter either their numbers or phenotypes. Small molecule inhibitors have been applied to inhibit cytokine secretion that recruits myeloid cells [84, 85] or T cell function [86, 83], or repolarizing cells such as tumor-associated macrophages [87]. Small molecule inhibitors of specific protein activators of MDSCs and TAMs have been shown to reduce their number and abrogate disease [58, 18]. Depletion of one or more cell types has also been studied in this context [58, 88, 89]. However, the large number of cells, cytokines, and other factors that contribute to the immune suppression limit the efficacy of therapies that target a single cell type or protein [90]. In addition, myeloid cell phenotypes within various tissues are distinct [91], which motivates the development of therapies that can elicit a tissue-dependent response.

An emerging approach for modulating innate immune cell response in tissues are nanoparticles administered intravenously that target circulating immune cells. Cargo-free polymer nanoparticles (NPs) have been shown to redirect the trafficking of phagocytic innate immune cells upon, and moderate the disease-induced aberrant behavior of these cells. The therapeutic benefit of these NPs has been demonstrated in a West Nile virus infection model, ischemic reperfusion injury [45], traumatic brain injury [92], as well as in spinal cord injury [93]. NPs have highly negative surface

charge that result in uptake through scavenger receptors including MARCO [45], and the specificity and biodistribution of polymeric NPs can be tuned with changes to the polymer backbone. As such, NPs are not limited to uptake targeting ligands [94], and they do not induce systemic responses in multiple tissue as with steroids or NSAIDs.

In this report, we test the hypothesis that cargo-free PLG nanoparticles administered intravenously divert circulating immune cells from the tumor microenvironment or metastatic sites, altering the immune responses at the niche and enhancing the efficacy of anti-PD1 immunotherapy. In the orthotopic 4T1 mouse model of metastatic triple negative breast cancer, disease-induced myeloid cells rapidly increase in number systemically with disease progression [22] and metastatic 4T1 cells readily colonize the lung due to the host of factors secreted by aberrant monocytes, macrophages, and MDSCs. These myeloid cells have also been shown to directly contribute to resistance to anti-PD-1 and anti-CTLA-4 in the 4T1 model [58]. The cell types and biodistribution of nanoparticles are analyzed, and the impacts of the particles on the cell phenotypes are analyzed both *in vitro* and *in vivo*. Particle administration is analyzed with respect the the growth of the primary tumor, as well as the impact on survival. Finally, impact of nanoparticles on gene expression within the primary tumor or metastatic site is analyzed. The ability of nanoparticles to reprogram innate immune cells within the primary tumor and metastatic tissues represents an opportunity to improving the therapeutic benefit of anti-PD-1 and other immunotherapies.

4.4 Results

4.4.1 Nanoparticle Internalization by Innate Immune Cells

PLG nanoparticle internalization by tumor-induced immune cells was initially investigated *in vitro*. Three fluorescently labeled NP formulations were synthesized by varying the surfactant type and PLG molecular weight (Fig. 4.1A) and incubated with blood leukocytes from tumor-bearing mice at 5 ug/mL and 50 ug/mL NP concentration (Fig. 4.1B). PEMA-High NPs exhibited high internalization at both concentrations, so the subsequent studies were performed with PEMA-High NPs. Myeloid-derived suppressor cells (MDSCs, $CD11b^+/Ly6Clo/^-/Ly6G^+$) and other myeloid cells ($CD11b^+/Ly6C^-/Ly6G$-) showed increased Cy5.5-NP internalization at 50 μg/mL relative to 5 μg/mL (Fig. 4.1C), whereas the increased concentration had no effect on the number of Cy5.5-NP^+ monocytes as a percentage of total cells. As MDSCs comprise a large majority of immune cells in circulation, internalization was also quantified as the percentage of Cy5.5-NP^+ cells relative to the number of single cells for each cell subtype (Fig. 4.1D). At 5 μg/mL, nearly all monocytes are NP^+ (89.4 $\pm$ 5.4%) while a lower percentage of MDSCs and other myeloid cells have lower relative internalization (23.7 $\pm$ 10.4% and 72.3 $\pm$ 14.5%, respectively). When the NP^+ cell numbers are increased at 50 μg/mL, nearly all cells are Cy5.5-NP^+ in all three cell populations (99.3 $\pm$ 0.5% of MDSCs, 99.9 $\pm$ 0.1% of monocytes, and 99.6 $\pm$ 0.2% of other myeloid cells). Taken together, these data demonstrate that monocytes more readily internalize NPs than other myeloid subtypes at low concentrations, yet nearly all MDSCs and other myeloid cells have internalized NPs.

The biodistribution and *in vivo* internalization by myeloid cell subsets was next studied following intravenous injection of Cy5.5-NPs. Assessment of whole-organ flu-

A

	Surfactant	PLG MW	Zeta (mV)	Size (nm)
PEMA-Low	PEMA, 1%	Low	-57.9 ± 0.6	428.6 ± 1.4
PEMA-High	PEMA, 1%	High	-24.1 ± 0.35	896.3 ± 19.05
PVA-High	PVA, 2%	High	-20.1 ± 0.38	249.4 ± 2.23

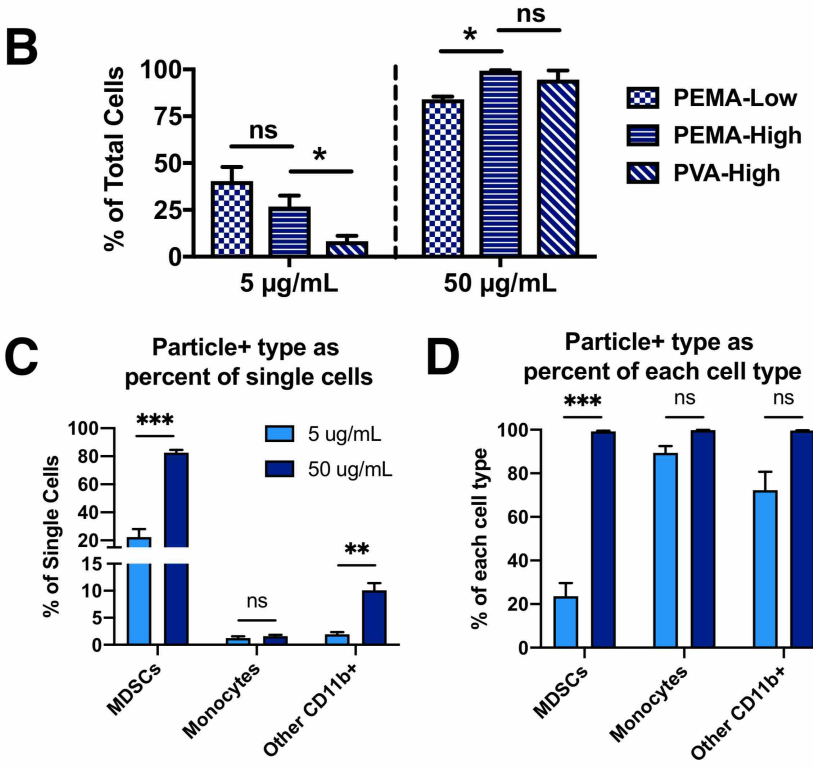

Figure 4.1: **Cy5.5-NPs are internalized by innate immune cells and are distributed in disease-relevant tissues.** (A) Three NP formulations with different combinations of surfactant and PLG molecular weight were tested for uptake *in vitro*. (B) Blood leukocytes from 4T1 tumor-bearing mice at 21 days post inoculation were incubated *in vitro* with each formulation at 5 μg/mL and 50 μg/mL, and internalization was quantified. PEMA-High NPs exhibited high uptake at both concentrations, and subsequent studies were performed with the PEMA-High NPs. Uptake was quantified (C and D) for myeloid cell subtypes (C) as a percentage of all cells and (D) as a percentage of each cell subtype. $CD11b^{+}/Ly6C^{lo/-}/Ly6G^{+}$ cells (MDSCs) and $CD11b^{+}/Ly6C^{-}/Ly6G^{-}$ cells (other myeloid cells) showed increased uptake with increase in NP concentration, while monocytes did not. These data indicate that monocytes more readily internalize NPs compared to MDSCs and other myeloid cells. A 2-way ANOVA with Tukeys multiple comparisons test was performed (A and B), bars show mean ± SEM for n = 3 biological replicates per condition, where ** $p < 0.01$, *** $p < 0.001$, ns, not significant.

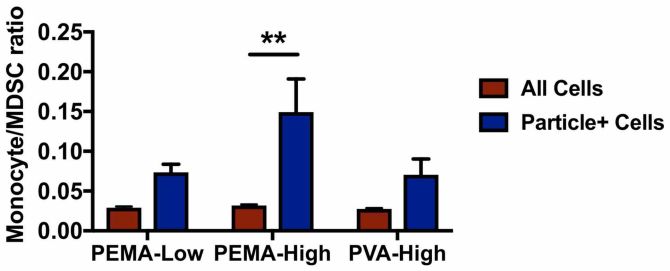

Figure 4.2: **Uptake specificity can be tuned by changing surfactant and polymer molecular weight.**

orescence (Fig. 4.3A and Fig. 4.4) indicated that Cy5.5-NPs accumulated primarily in the liver and spleen, and Cy5.5-NPs were detected in these organs through 48 hours post injection. NPs accumulated in the lung at 12 hours, yet the majority was cleared from the lung by 48 hours. Relatively low levels of Cy5.5-NPs were detected in the tumor. The cell types within these organs that were associated with NPs was quantified by flow cytometry and each NP+ cell type was shown as a percentage of all NP+ cells within each organ (Figs 2B, S2B). Monocytes comprised the largest population of NP+ myeloid cells in all organs (37.6 ± 7.9%, 46.3 ± 7.9%, 26.6 ± 4.3%, 7.6 ± 2.4% in tumor, lung, spleen, and liver, respectively) compared to MDSCs (15.6 ± 5.3%, 34.8 ± 10.0%, 7.8 ± 2.0%, 3.6 ± 0.7% in tumor, lung, spleen, and liver, respectively) and macrophages (19.5 ± 7.7%, 3.3 ± 0.5%, 3.5 ± 0.8%, 4.0 ± 0.9% in tumor, lung, spleen, and liver, respectively).

4.4.2 Nanoparticle Administration Alters Immune Cell Distribution in Blood and Organs

We next investigated whether the intravenously delivered NPs would influence the distribution of innate immune cells in circulation, and at the primary tumor or metastatic sites (i.e., lung). The analysis of blood revealed that the proportion of MDSCs decreased from 82.5 ± 2.8% to 63.5 ± 13.9% (Fig. 4A). No significant change

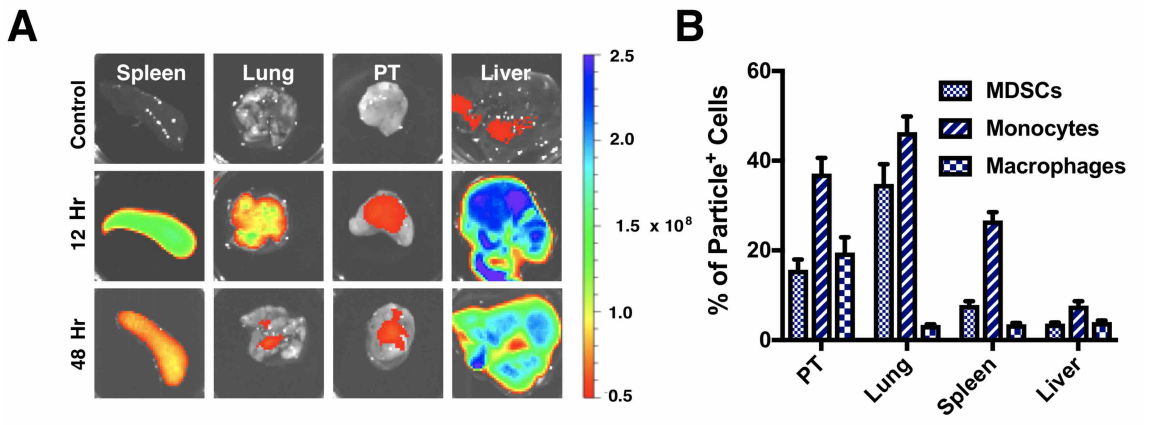

Figure 4.3: ***In vivo* distribution of Cy5.5-NPs.** (A) *Ex vivo* imaging following i.v. injection of 1 mg of Cy5.5-NPs shows they primarily accumulate in spleen and liver, and are detectable for more than 48 hours post injection. (B) Quantification of particle uptake by myeloid cell subsets within tissues as a percentage of total NP^+ cells for a given tissue.

was observed in the percentage of macrophages ($CD11b^+/F4/80^+$), monocytes, or dendritic cells (DCs, $CD11c^+$) in the blood with NP administration (Fig. 4.5). The accumulation of cells within the primary tumor and metastatic sites was analyzed following 6 consecutive days of NP administration. The quantity of MDSCs as a percentage of all single cells in the lung (Fig. 4.5C) decreased with NP administration ($30.0 \pm 3.7\%$ for PBS vs. $21.1 \pm 6.2\%$ for NP), consistent with a decrease observed in the blood (Fig. 4.5A). No significant differences in myeloid cell proportions were observed in the spleen or primary tumor.

4.4.3 Synergistic Therapeutic Effect Observed in Nanoparticles Combined with Anti-PD-1

The therapeutic efficacy of NPs against 4T1 tumor growth and metastasis was next investigated. Mice were inoculated with orthotopic 4T1 tumors and placed in one of four treatment groups: 1) PBS control, 2) anti-PD-1 antibody only, 3) NPs only, and 4) NPs + anti-PD-1 (Fig. 4.6A). Average tumor size was decreased for

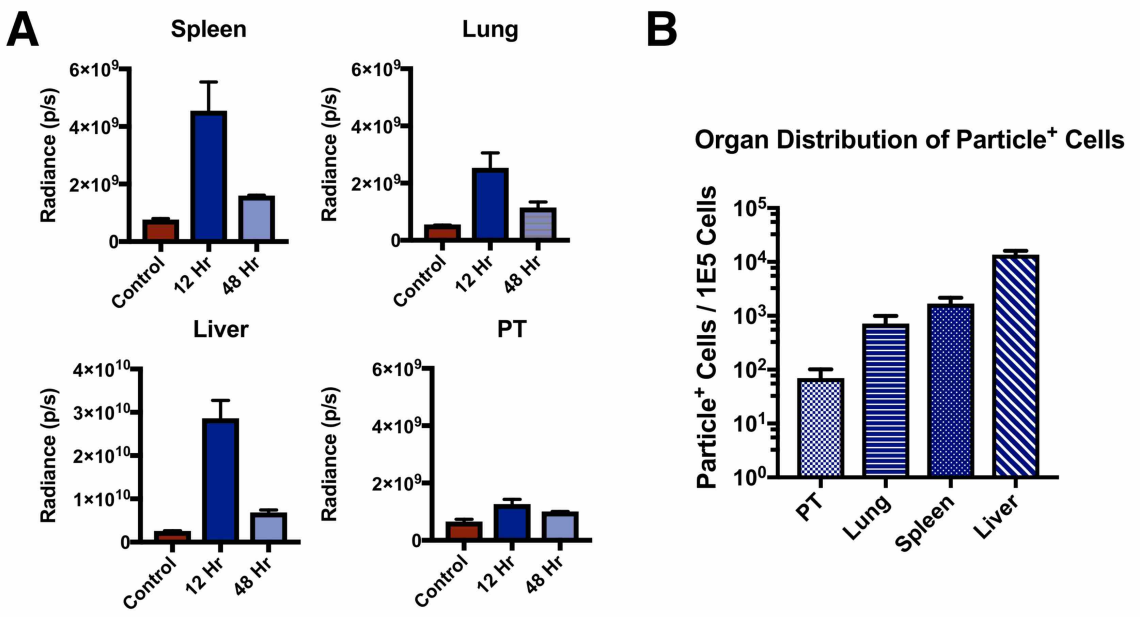

Figure 4.4: **Quantification of Cy5.5-NP signal by IVIS (A, n = 3 NP$^+$, n = 2 PBS) and (B) flow cytometry.**

combination NPs + anti-PD-1 (V = 1240 ± 298 mm^3) compared to PBS control (V = 1940 ± 431 mm^3; p = 0.038), but was not decreased for either monotherapy (V = 1630 ± 578 mm^3 for anti-PD-1; V = 1690 ± 575 mm^3 for NPs) (Fig. 4.6B). Survival, based on body condition and tumor appearance, was monitored after day 22 post inoculation (Fig. 4.6C). Median survival was 24 days for the PBS and anti-PD-1 groups, 25 days for NPs alone, and 28 days for NPs + anti-PD-1 combination treatment. A survival benefit was observed for the combination treatment cohort compared to cohorts treated with PBS (p = 0.001), or cohorts treated with either anti-PD-1 or NP monotherapy (p = 0.015 and p = 0.030, respectively). The efficacy of the combination therapy on metastatic burden was evaluated through analysis of tumor cell numbers in the lung. Combination therapy reduced the lung metastatic burden by 2-fold compared to PBS control (p = 0.018). Taken together, these data indicate an additive or synergistic therapeutic effect by combining NPs and anti-PD-1 antibody.

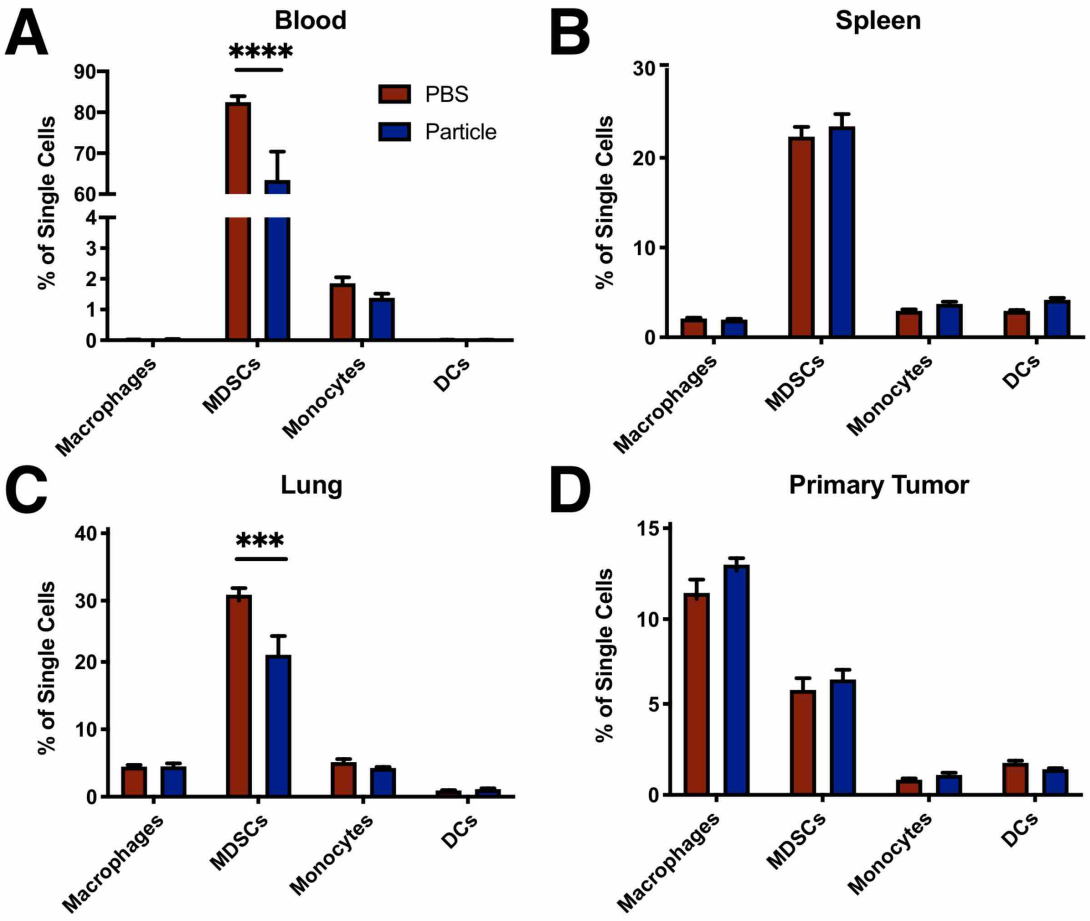

Figure 4.5: ***In vivo* administration of cargo-free NPs reduces the proportion of MDSCs in circulation and at metastatic organs.** (A) Tumor-bearing mice at were administered i.v. 1 mg of NPs in 200 μL of PBS or the equivalent volume of PBS only (n = 4 per group), and innate immune cells were quantified in the blood 12 hours post injection by flow cytometry. (B-D) NPs were administered at a dose of 1 mg/200 μL for 6 days to allow for accumulation and uptake of NPs (n = 4 PBS control, n = 5 NP). Flow cytometry quantification of immune cells in the spleen (B), lung (C), and primary tumor (D) was performed on day 10 post inoculation. Decrease in MDSCs observed in the blood (A) and lung (C) with NP administration. A 2-way ANOVA with Tukeys multiple comparisons test was performed (A-D), bars show mean ± SEM, where *** $p < 0.001$, and **** $p < 0.0001$.

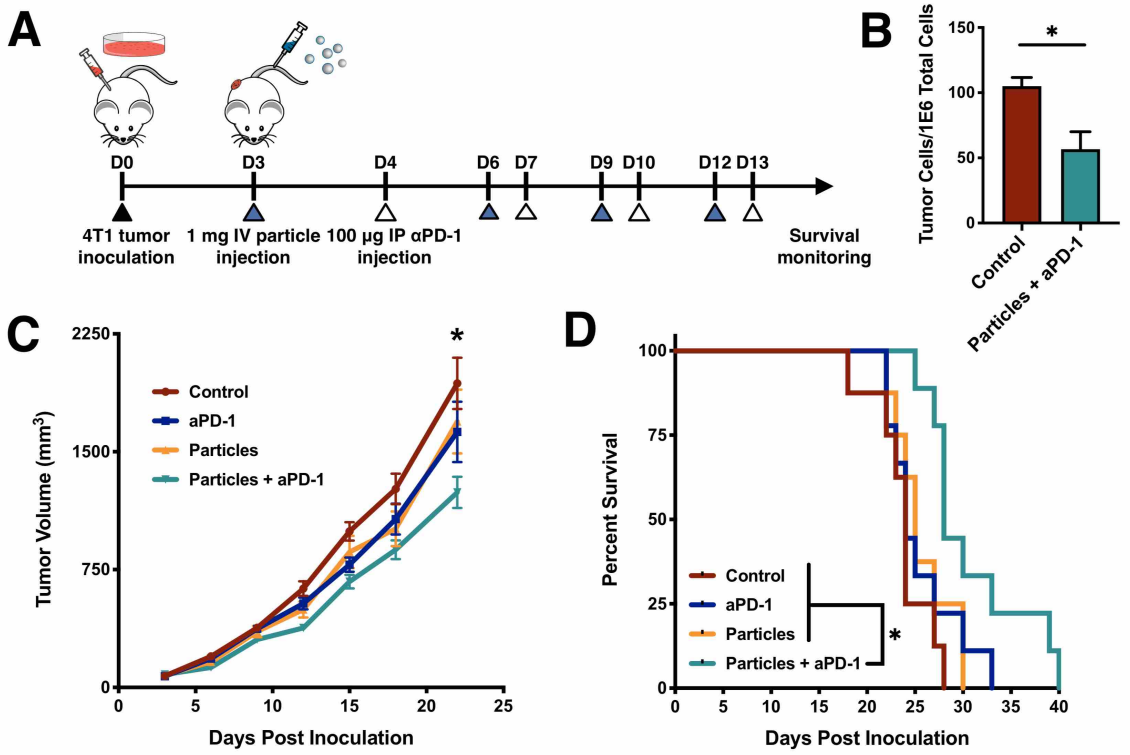

Figure 4.6: **NPs + anti-PD-1 combination therapy delays 4T1 tumor growth and reduces metastasis.** 4T1-bearing mice were treated with PBS (control), anti-PD-1 (aPD-1), NPs (particles), or combination therapy (particles + aPD-1). (A) Schematic of disease model and treatment. (B) A two-fold reduction in lung metastatic burden (n = 4 per group) at day 14 post inoculation as measured by flow cytometry for particles + aPD-1 compared to control. (C) Tumor volumes, and (D) survival curves are shown for the four treatment conditions (control, n = 7; aPD-1, n = 9; particles, n = 8, particles + aPD-1, n = 9), indicating a therapeutic benefit for particles + aPD-1 but not for either monotherapy compared to control. Two-tailed unpaired t test (B) and 2-way ANOVA with Tukey's multiple comparisons tests were performed. Bars show mean ± SEM where * $p < 0.05$ compared to control (C), and where * $p < 0.05$ compared to particles + aPD-1 (D).

4.4.4 Nanoparticle Internalization Results in Upregulation of Inflammatory Pathways

The mechanism by which NP administration may reduce tumor growth and metastasis was investigated *in vitro* by analyzing cell secretion of multiple cytokines associated with tumor progression following nanoparticle treatment. Mice were first treated with anti-PD-1 antibody post inoculation (Fig. 4.7A), and splenocytes were then isolated from healthy and tumor-bearing mice (with and without anti-PD-1 treatment) at day 14 post inoculation. Splenocytes from tumor-bearing ($Tumor^+$) mice secreted elevated amounts of the cytokines interleukin 6 (IL-6), granulocyte-macrophage colony-stimulating factor (GM-CSF), monocyte chemoattractant protein 1 (MCP-1), and tumor necrosis factor alpha (TNF-α), but not transforming growth factor beta (TGF-β) relative to those of $Tumor^-$ mice (Fig. 4.7 B-F). Treatment of these cells with NPs significantly decreased secretion of MCP-1 (Fig. 4.7D) and increased TNF-α ecretion (Fig. 4.7E). This effect is amplified with the addition of anti-PD-1 ($Tumor^+$ $\alpha PD\text{-}1^+$). No alteration in cytokine expression was observed for NP treatment for production of IL-6 (Fig. 4.7B) or TGF-β (Fig. 4.7F) in tumor-bearing mice with or without anti-PD-1. Increased granulocyte-macrophage colony-stimulating factor (GM-CSF) production was observed with NP treatment only in the $Tumor^+$ $\alpha PD\text{-}1^+$ group (Fig. 4.7C). Notably, NP^+ treatment increased TNF-α production by more than 2-fold in tumor-bearing mice both with and without anti-PD-1 (Fig. 4.7E). The production of MCP-1 is also greatly increased in tumor-bearing mice, yet there is a nearly 5-fold decrease in secreted MCP-1 with NP treatment in both the $Tumor^+$ and $Tumor^+$ $\alpha PD\text{-}1^+$ groups. These data indicate that NPs can alter the production of inflammatory cytokines and that anti-PD-1

contributes to additional changes in cytokine levels.

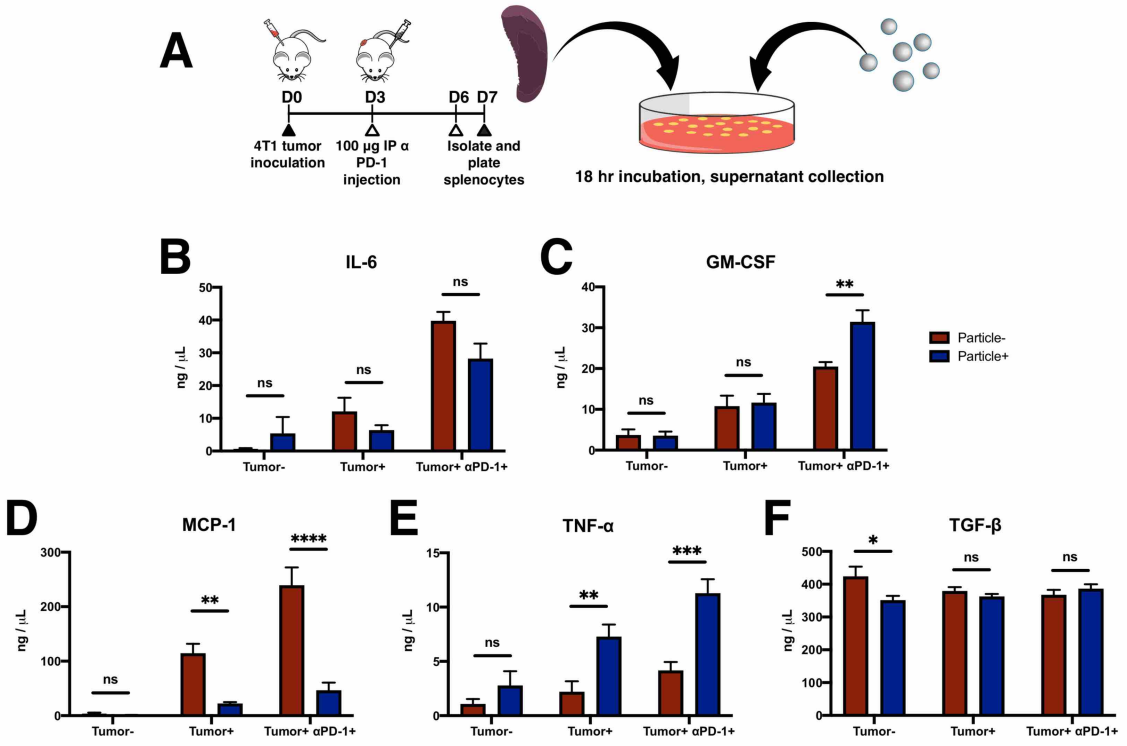

Figure 4.7: **Reprogramming of inflammatory response by NP treatment *in vitro*.** A) Schematic and timeline of the study. Splenocytes from tumor-bearing mice that were treated with or without aPD-1 and incubated with NPs. (B-F) Cytokine secretion as measured by ELISA for splenocytes isolated from healthy (tumor-), tumor-bearing (tumor$^+$), and *in vivo* aPD-1-treated (tumor$^+$ aPD-1$^+$) mice. Solenocytes were treated *in vitro* with (particle$^+$) or without (particle-) NPs. Notably, there was a large decrease in the production of the MDSC-recruiting chemokine MCP-1 (D) and an increase in the production of proinflammatory TNF-a (C). 2-way ANOVA with Tukeys multiple comparisons tests were performed. Bars show mean ± SEM where * $p < 0.05$, ** $p < 0.01$, *** $p < 0.001$, **** $p < 0.0001$ compared to particle$^-$ control ($n = 4$ per condition).

4.4.5 Tissue-Specific Deactivation of Disease-Relevant Pathways *In Vivo*

Gene expression within the primary tumor and metastatic site was analyzed at day 14 post inoculation to assess the impact of NP and anti-PD-1 treatment on these tissues. Gene expression at the spleen was analyzed as a control for systemic immune changes. Principal component analysis based on DESeq2 normalized total

	Tissue	Total Genes	Up	Down	Total Pathways	Up	Down
NP Only	Lung	14472	6	8	5944	221	623
	Spleen	14472	128	43	5944	327	264
	Tumor	14472	2	0	5944	353	71
NP + aPD-1	Lung	14472	173	105	5944	84	934
	Spleen	14472	54	91	5944	612	165
	Tumor	14472	1	0	5944	411	110

Table 4.1: **Summary of *in vivo* gene expression changes with treatment compared to PBS.**

expression [95] showed that different tissues clustered together by gene expression, yet the treatment groups were not readily distinguished (Fig. 4.8). Differential gene expression was evaluated for each tissue compared to the PBS control group (Table 4.1). In addition, pathway changes were investigated using Gene Set Enrichment Analysis (GSEA) for a total of 5,944 gene sets were examined (Fig. 4.9). Gene sets that showed the greatest enrichment (positive or negative) for immune cells were obtained for each tissue and condensed into a list of 14 disease-relevant pathways (Fig. 4.10). Pathways with normalized enrichment score (NES) $>$ 1.3 or NES $<$ -1.3 was considered differentially expressed compared to untreated control. NP treatment resulted in downregulation of pathways associated with pro-tumor innate cells and upregulation of IL-2 biosynthesis in the lung. The addition of anti-PD-1 appeared to downregulate negative regulation of T cell proliferation. Cells in NP-treated spleens exhibited downregulation of intrinsic apoptosis and upregulation of T cell chemotaxis. Anti-PD-1 additionally increased signaling by VEGF and along with several immune activation pathways in the spleen. The intrinsic apoptotic pathway was downregulated in the tumor, while extrinsic apoptotic signaling was upregulated in both treatments. Taken together, these data suggest deactivation of pro-tumor immune cells and upregulation of anti-tumor pathways with NP treatment.

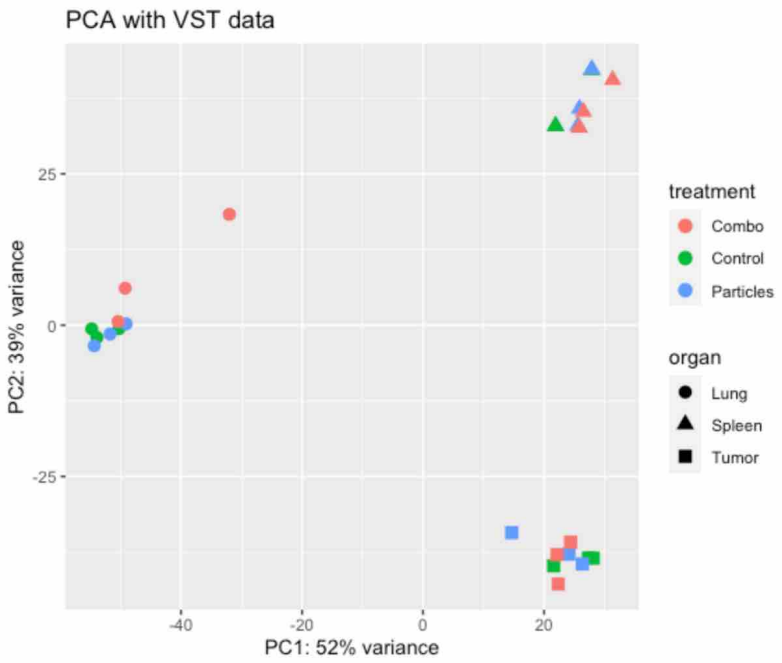

Figure 4.8: **Principal component analysis of RNAseq for each sample and condition show organs cluster together.**

4.5 Discussion

In this study, cargo-free PLG NPs were investigated for systemic delivery and therapeutic efficacy in the 4T1 mouse model of metastatic breast cancer. Innate immune cells, such as MDSCs, inflammatory monocytes, and TAMs have been revealed to support pro-tumor functions at the primary tumor and metastatic niche. These cells have been widely studied for their potential as biomarkers for early diagnostics of cancer and metastasis [96, 97, 98, 99, 100]. Furthermore, the therapeutic benefit of immunotherapies, such as immune checkpoint blockade (ICB) and CAR T-cells, which primarily aim to improve the adaptive anti-tumor immune response, are limited by the presence of these immunosuppressive innate cells [58, 88, 89]. As such, targeting of these innate immune cells has emerged as a potential cancer immunotherapy. The data presented here demonstrate that NPs delivered systemically alter the phenotype of the pro-tumor innate immune cells at the primary tumor and

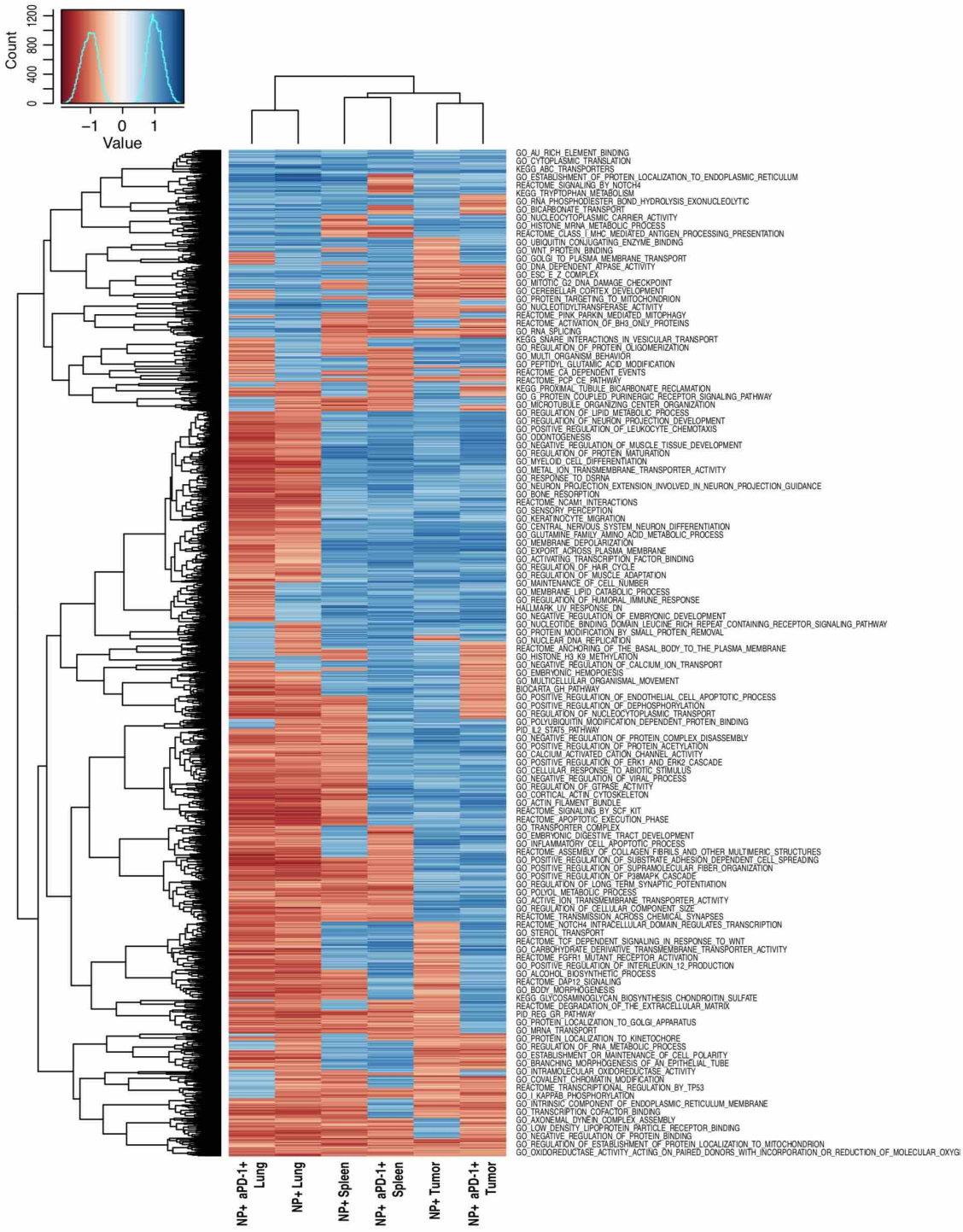

Figure 4.9: **Gene set enrichment analysis (GSEA) heatmap for a set of 5,944 pathway changes for lung, spleen, and tumor compared with tissues from PBS-treated mice.** Pathway changes in the spleen were more similar to those in the tumor. The lung showed broad downregulation of immune-related pathways.

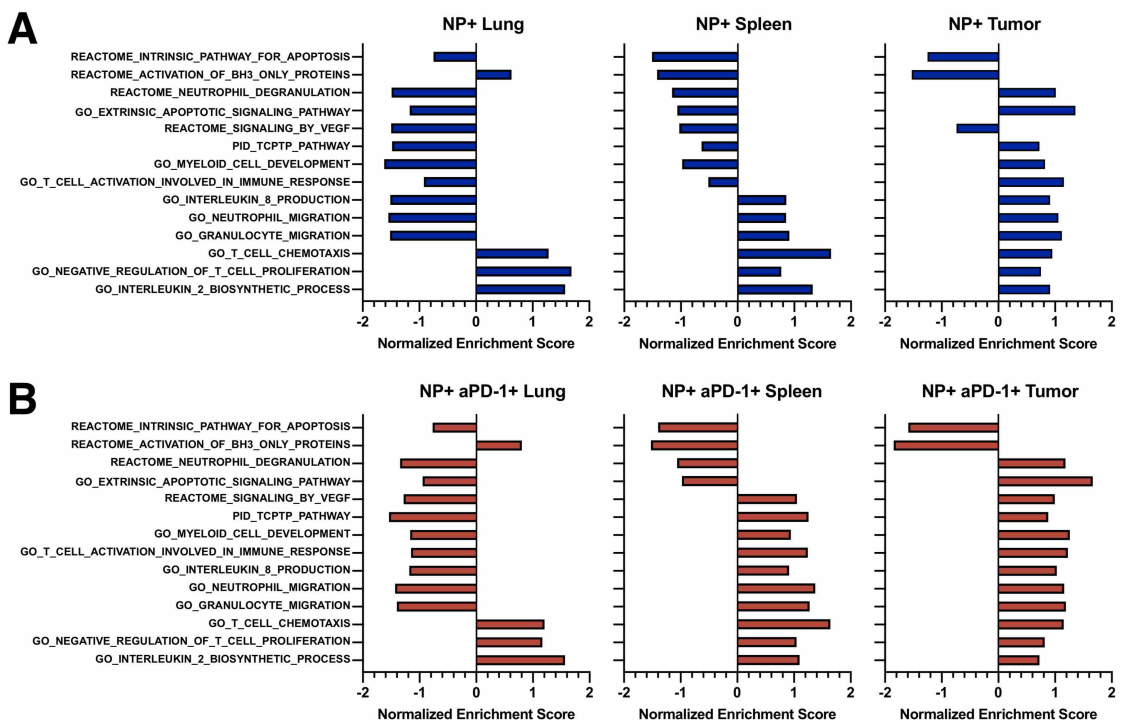

Figure 4.10: **Tissue-specific *in vivo* reprogramming by NP and aPD-1 treatment.** Gene expression by RNA-seq was performed on lung, spleen, and tumor tissue from mice treated with PBS, NPs, or NPs + anti-PD-1 (n = 3 per condition), and phenotypic differences were analyzed by Gene Set Enrichment Analysis. (A and B) Pathway enrichment for NP (A) and NP and aPD-1 (B) treated mice as shown by normalized enrichment score (NES) compared with PBS for the given gene sets. Pathways with NES $>$ 1.3 or NES $<$ -1.3 were considered differentially expressed. Changes in the tumor largely reflected systemic changes as seen in the spleen, with positive enrichment of immune cell function, whereas the lung showed negative enrichment in many of these pathways.

metastatic sites, resulting in a therapeutic benefit when combined with anti-PD-1.

Previous studies have targeted innate immune cells with antibodies or small molecules against cell surface receptors or their ligands. MDSC depletion with antibodies either against Gr-1 or Ly6G has been reported to have a therapeutic benefit in multiple cancer models [101, 102]. In the 4T1 model, diversion or depletion of MDSCs has resulted in a survival benefit following resection of the primary tumor [103, 22]. Inhibiting MDSC activation resulted in total elimination of tumors in mice treated with combination anti-PD-1 and anti-CTLA-4 [58]. Alternatively, small molecule inhibitors of myeloid cell recruitment and activation have also proven to be effective

for targeting specific myeloid cells and improving the efficacy of immuno-, chemo-, and radio-therapies. However, there have been several reports of adverse effects of existing therapies. Stopping CCL2 inhibition has been shown to accelerate breast cancer metastasis [104]. CSF1R inhibition delays tumor growth [18], yet also promoted metastasis by diminishing the amount of IL-15 and reducing the number of NK cells [105]. The NPs reported here do not deplete the cell types, and do not contain an active pharmaceutical ingredient. No adverse effects were observed for NP treated animals in these studies, suggesting that NPs may provide an opportunity to enhance outcomes and improve safety by avoiding off target effects. In addition, human MDSCs cannot be readily targeted with these antibodies due to differences between mouse and human surface proteins [5, 90, 106]. NPs may instead provide an opportunity to modify human MDSCs based on a similar functionality between human and mice.

Administration of cargo-free PLG NPs intravenously in the cancer model leads to their subsequent association with monocytes, MDSCs, and other myeloid cells (Fig. 4.3B), which results in a reduction in the percentage of myeloid cells present in the blood and lung (Fig. 4.5). The NPs accumulated primarily in the spleen and liver, and to a lesser extent in the lung for the first 48 hours post injection. Previous reports have suggested that intravenous NP administration diverted inflammatory cells to the spleen [45, 93], while others have observed granulocyte trafficking to the liver in several inflammatory disease models [107]. A greater percentage of Ly6C^{hi} monocytes was observed to internalize NPs relative to MDSCs and other myeloid cells, though no significant decrease in monocytes was observed in tissues. These monocytes are thought to be precursors of TAMs [81], and previous studies found decreased metastatic seeding in the lung when monocyte recruitment was inhib-

ited [17]. The lower level of association with MDSCs is consistent with a decreased capacity for phagocytosis [13], yet confirms previous findings that MDSCs can still be targeted through particle internalization [108]. The difference in NP uptake may also be explained in part by physicochemical properties of the NPs. Preferential internalization by specific cell types was reported to be a function of the surfactant used for NP manufacturing [109] or polymer properties [110]. In addition, nanoparticle size and surface charge influence internalization by myeloid cells [111], and selectivity can be achieved without targeting moieties [112, 113].

Reduced primary tumor growth in addition to reduced lung tumor burden was observed in the 4T1 model with combination NP and anti-PD-1 treatment (Fig. 4.6). NP internalization induces phenotypic changes in the myeloid cells, with the response dependent upon the status of the immune system. PLG nanoparticles have been applied to reduce inflammation in spinal cord injury, yet the NPs appear to induce inflammatory pathways both *in vitro* and *in vivo* in the 4T1 model. *In vitro* studies of NP internalization indicated upregulation of two immunostimulatory cytokines TNF-α and GM-CSF. These cytokines have relatively nuanced roles in cancer progression. Neutralization of systemic GM-CSF with cytokine sponges can enhance the efficacy of anti-PD-1 treatment [114]. Conversely, combinations of GM-CSF, IL-6, and TNF-a have also been shown to inhibit human T cell activation *in vitro*, though solid tumors that contained MDSCs were found to consistently downregulate GM-CSF [90]. NP treatment *in vitro* also resulted in a decrease in the production of MCP-1 (CCL2), which is a critical cytokine for the recruitment of MDSCs [17]. Signaling within the tumor microenvironment or the metastatic niche is complex, and the survival advantage provided by these particles warrant further investigation into the mechanisms of action.

NP treatment led to substantial changes in the gene expression systemically and within the primary tumor and metastatic sites, which may contribute to the delayed progression of disease and the survival benefit. Differential gene expression and pathway analysis revealed downregulation of neutrophil-related signaling and function, notably a decreased expression of matrix metallopeptidase 9 (MMP9) in the lung. MMP9 has been shown to be a major contributor to the establishment of the pre-metastatic niche [115, 116], and its downregulation along with other proteins in ECM pathways indicate the NPs may have altered the lung microenvironment to be less favorable for tumor cell colonization. Additional downregulation of pro-tumor neutrophil/MDSC-related pathways and upregulation of IL-2 biosynthesis and signaling pathways were observed in the lungs of treated with NPs. IL-2 is primarily produced by $CD4^+$ T cells and can stimulate growth and proliferation of $CD8^+$ T cells, and IL-2 therapy has been successfully been used to treat metastatic cancer, but exhibits high toxicity when delivered systemically [117]. The upregulation of IL-2 in the lung and not the liver or spleen indicates tissue-specific activation of IL-2, which may confer anti-tumor benefit at the metastatic site while reducing toxicity. The enrichment of extrinsic apoptosis response at the primary tumor may be reflective of increased tumor cell killing as evidenced by slower tumor growth. This effect was not detected in the lung or spleen, which may be due to the relatively small numbers of tumor cells in the organs compared. The addition of anti-PD-1 led to downregulated negative regulation of T cell proliferation, which is consistent with findings that PD-1 downregulates T cell proliferation [118].

In conclusion, we report that PLG NPs delivered systemically to target circulating immune cells improve the efficacy of ICB. The NPs are well-tolerated due to the absence of an active pharmaceutical ingredient may reduce off target effects. The

NPs reprogram immune cell phenotypes by altering their trafficking and expression of key cytokines, which can alter the microenvironment of the primary tumor or metastatic sites. Modulation for the innate cell responses by the NPs combined with ICB therapy that targets the adaptive responses contributes to an improved therapeutic outcome. PLG NPs that target circulating innate immune cells may provide novel therapeutic strategies in cancer, used either alone or to complement current or emerging T-cell-targeted immunotherapies.

4.6 Materials and Methods

4.6.1 Nanoparticle fabrication

To fabricate fluorescent nanoparticles, acid-terminated 50:50 Poly(DL-Lactide-co-Glycolide)(PLG) polymer (inherent viscosity 0.55-75 dL/g, Lactel) was first conjugated with cyanine 5.5 amine dye (Lumiprobe) using N-(3-Dimethylaminopropyl)-N-ethylcarbodiimide hydrochloride (EDC) (Sigma-Aldrich)/N-hydroxysuccinimide (NHS) (Thermo Fisher Scientific) chemistry. Unconjugated polymer and cyanine 5.5-conjugated polymer were then dissolved in ethyl acetate at 99:1 weight ratio. The dissolved polymer was added to a Poly (ethylene-alt-maleic anhydride) (PEMA)(Polyscience) solution and the mixture was sonicated using a Cole-Parmer CPX130 Ultrasonic Processor to form the nanoparticles. Organic solvent was removed by evaporation overnight, and nanoparticles were lyophilized for storage following three washes in DI water.

4.6.2 Tumor cell culture and inoculation

4T1-luc2-tdTomato cells (Perkin Elmer) were expanded in RPMI 1640 + GlutaMAX (Thermo Fisher Scientific) with 10% FBS for 5 days at 37°C and 5% CO_2 prior to inoculation. Cells were removed from culture flasks by incubation with trypsin for 10 minutes at 37°C and resuspended in RPMI 1640. Cells were then pelleted by centrifugation at 300 x g and washed with DPBS, and resuspended at 1 x 10^7 cells/mL of DPBS. Orthotopic tumor inoculations were performed by injection of 5 x 10^5 tumor cells resuspended in 50 μL DPBS (Life Technologies) into the fourth right mammary fat pad of 8- to 10-week-old female BALB/c mice (Jackson Laboratory). The cell line was confirmed to be pathogen free and authenticated by short tandem repeat DNA analysis and compared to the ATCC STR profile database (DDC Medical).

4.6.3 Nanoparticle and anti-PD-1 treatment

Nanoparticles were resuspended in DPBS (Life Technologies) at 1mg in 200 μL and passed through a 35 μm filter mesh prior to intravenous administration via tail vein injection. Control animals received 200 μL of DPBS intravenously. InVivoMab anti-mouse anti-PD-1 (CD279) antibody (clone RMP1-14, Bio X Cell) was diluted in DPBS to a final concentration of 1 mg/mL immediately prior to i.p. injection. For therapeutic efficacy studies, NPs and anti-PD-1 were administered once every 3 days, for a total of 4 doses. For studies with NP biodistribution in tissues, Cy5.5-NPs were administered at a dose of 1 mg/200 μL for 6 days to allow for accumulation of NPs and to observe potential NP-induced cell trafficking (n = 4 PBS control, n = 5 NP). Organs were explanted at day 10 post inoculation and innate immune cell

distribution was quantified by flow cytometry. For studies of NPs and blood-based immune cell distribution, a single dose of NPs was injected and flow analysis of blood was performed 12 hours post injection.

4.6.4 Tumor size measurement and survival monitoring

Tumors were measured using standard electronic calipers (VWR) while mice were anesthetized with 2% v/v% isoflurane. Tumor volume was calculated as V = 0.5 x L x W^2, where L is the length of the longest dimension of the tumor and W is the length of the tumor perpendicular to the longest dimension. Mice were monitored for tumor size and body conditioning to determine survival. Mice were euthanized if any of the following criteria were met: tumor size of $>$ 2cm in any dimension, ulceration of more than 50% of the visible tumor area, partial paralysis due to tumor invasion of hind limb muscle, labored breathing, ascites, lethargy, or visible weight loss.

4.6.5 *Ex vivo* fluorescence and bioluminescence imaging

Nanoparticle distribution was measured in explanted whole organs following particle injection at 675/700 Ex/Em using an IVIS Lumina LTE imaging system (Caliper Life Science). Fluorescence signal intensity is reported as photon flux in total photon count per cm^2 per steradian. Metastatic tumor burden of luciferase-expressing tumor cells in explanted lungs was measured by bioluminescence imaging with the IVIS. Lungs were incubated in 50 μM d-luciferin (Caliper) at room temperature for 10 minutes prior to imaging. Bioluminescence signal intensity is reported as integrated light flux (photons/sec) as calculated by the Living Image Software (Caliper Life Sciences).

4.6.6 Flow cytometry

Flow cytometry was performed on primary cells obtained from explanted organs. Spleens, lungs, primary tumors, and livers were minced and enzyme digested with Liberase TL or TM (Roche), then filtered through a 70 μm cell strainer (Corning) to obtain a cell suspension. Whole blood was collected by cardiac puncture and mixed with 10 v/v% 25mM EDTA (Life Technologies). Red blood cell lysis of whole blood, spleens, and lungs was performed with ACK Lysing Buffer (Life Technologies). Cells were pelleted by centrifugation at 400xg for 5 minutes and resuspended in MACS buffer. Nonspecific staining was blocked with anti-CD16/32 (Biolegend) and samples were stained for innate immune markers with anti-mouse CD45 AF700, F4/80 PE-Cy7, Ly6G PacBlue, Ly6C FITC (Biologend), and CD11b BV510 (BD Biosciences). For adaptive markers, samples were stained with anti-mouse CD45 AF700, CD4 V500, CD8 FITC, CD19 PacBlue, and CD49b PE-Cy7 (Biolegend). Stained samples were analyzed using the MoFlo Astrios Flow Cytometer or CytoFLEX (Beckman Coulter), and data were processed using FlowJo (BD) and MATLAB release 2019a (MathWorks).

4.6.7 *In vitro* nanoparticle uptake and ELISA

Single cell suspensions were isolated from spleens and whole blood of tumor-bearing mice at 14 or 21 days post tumor inoculation as described above. For nanoparticle uptake assays, cells were resuspended in RPMI 1640 media with 10% FBS and seeded in 24-well plates at 1 x 10^6 cells per well. Nanoparticles were resuspended in DPBS at 1mg/mL and added to the wells. Uptake was characterized

following a 30 minute incubation at 37°C by flow cytometry as described above. For cytokine secretion assays, cells were resuspended in media and seeded in 96-well plates at 2.5 x 10^5 cells per well. Nanoparticles were resuspended as described above and added to each well. Following incubation for 6, 18, or 24 hours, cells were pelleted at 1000 x g for 5 minutes and the supernatant was removed and diluted 4x for quantification of cytokine secretion by ELISA, which was performed by the Caner Center Immunology Core at the University of Michigan.

4.6.8 Gene expression analysis by RNA-seq

Tissues were flash-frozen as described above and homogenized in TRIzol reagent (Thermo Fisher Scientific). RNA was extracted from each tissue sample with the Direct-zol RNA spin column kit (Zymo Research). Purified RNA concentration was measured by UV spectroscopy using a Nanodrop 2000c (Thermo Scientific) to confirm all samples had concentrations 10 ng/μL. RNA quality control, QuantSeq 3 mRNA-seq library prep and quality control, and sequencing were performed by the Advanced Genomics Core at the University of Michigan. Samples were sequenced using the Illumina NextSeq 550 sequencer, and sequences were aligned to Gene Symbols. Raw sequencing counts were normalized and differential gene expression was calculated in R and using DESeq2 [95]. Normalization of raw counts was performed for principal component analysis [119] and genes with differential expression were identified. For pathway analysis, mouse gene symbols for counts obtained through RNA-seq were first converted to human gene symbols using the biomaRt package in R. Gene Set Enrichment Analysis (GSEA) was performed on DESeq2-normalized counts and the corresponding human gene symbols for a total of 5,944 MsigDB gene sets (Hallmark, Reactome, PID, and Gene Ontology (GO)). A positive normalized

enrichment score (NES) indicates enrichment in the treated cohort compared with PBS control.

4.6.9 Statistical analysis

One-way or two-way ANOVA and Tukey's multiple comparisons tests were performed on groups with more than 2 conditions. Two-tailed unpaired t test was used for single comparisons between two conditions. Median survival and survival curves were analyzed with the log-rank (Mantel-Cox) test for statistical significance. Following normalization of RNA-seq gene expression data with DESeq2, genes with adjusted p-value < 0.05 were considered differentially expressed. Statistical analyses were performed using Prism 8 (GraphPad Software). A p-value < 0.05 was considered to be statistically significant and all values are expressed in mean $\pm$ standard deviation (SD). Error bars one plotted data represent standard error of the mean (SEM).

CHAPTER V

Metastatic Conditioning of Myeloid Cells at a Subcutaneous Synthetic Niche Reflects Disease Progression and Predicts Therapeutic Outcomes

5.1 Authors

Robert S. Oakes, Grace G. Bushnell, Sophia M. Orbach, Pridvi Kandagatla, Yining Zhang, Aaron H. Morris, Matthew S. Hall, Petrina LaFaire, Joseph T. Decker, Rachel M. Hartfield, Michael D. Brooks, Max S. Wicha, Jacqueline S. Jeruss, and Lonnie D. Shea

5.2 Abstract

Monitoring metastatic events in distal tissues is challenged by their sporadic occurrence in obscure and inaccessible locations within these vital organs. A synthetic biomaterial scaffold can function as a synthetic metastatic niche to reveal the nature of these distal sites. These implanted scaffolds promote tissue ingrowth, which upon cancer initiation is transformed into a metastatic niche that captures aggressive circulating tumor cells. We hypothesized that immune cell phenotypes at synthetic niches reflect the immunosuppressive conditioning within a host that contributes to metastatic cell recruitment and can identify disease progression and response to

therapy. We analyzed the expression of 632 immune-centric genes in tissue biopsied from implants at weekly intervals following inoculation. Specific immune populations within implants were then analyzed by single-cell RNA-seq. Dynamic gene expression profiles in innate cells, such as myeloid-derived suppressor cells, macrophages, and dendritic cells, suggest the development of an immunosuppressive microenvironment. These dynamics in immune phenotypes at implants was analogous to that in the diseased lung and had distinct dynamics compared with blood leukocytes. Following a therapeutic excision of the primary tumor, longitudinal tracking of immune phenotypes at the implant in individual mice showed an initial response to therapy, which over time differentiated recurrence versus survival. Collectively, the microenvironment at the synthetic niche acts as a sentinel by reflecting both progression and regression of disease.

5.3 Introduction

All too often, the detection of cancer occurs after some tissue such as the lung or bone begin to fail, which typically represents an advanced stage of disease that is challenging to treat. Systems for the early detection of cancer would provide the opportunity to intervene at earlier stages and prior to tissue dysfunction. The risk for distant recurrence is being determined by gene and protein expression in primary tumor samples that define molecular signatures of patient tumors. Clinically, these molecular signatures are reduced to predictive scores, which help guide decisions about systemic therapy for patients with cancer [120]. Clinical examples include Oncotype DX [121], Mammaprint [122], PAM50 ROR Score [123, 124], Breast Cancer Index [125], and EndoPredict [126]. Yet, the information obtained from the primary

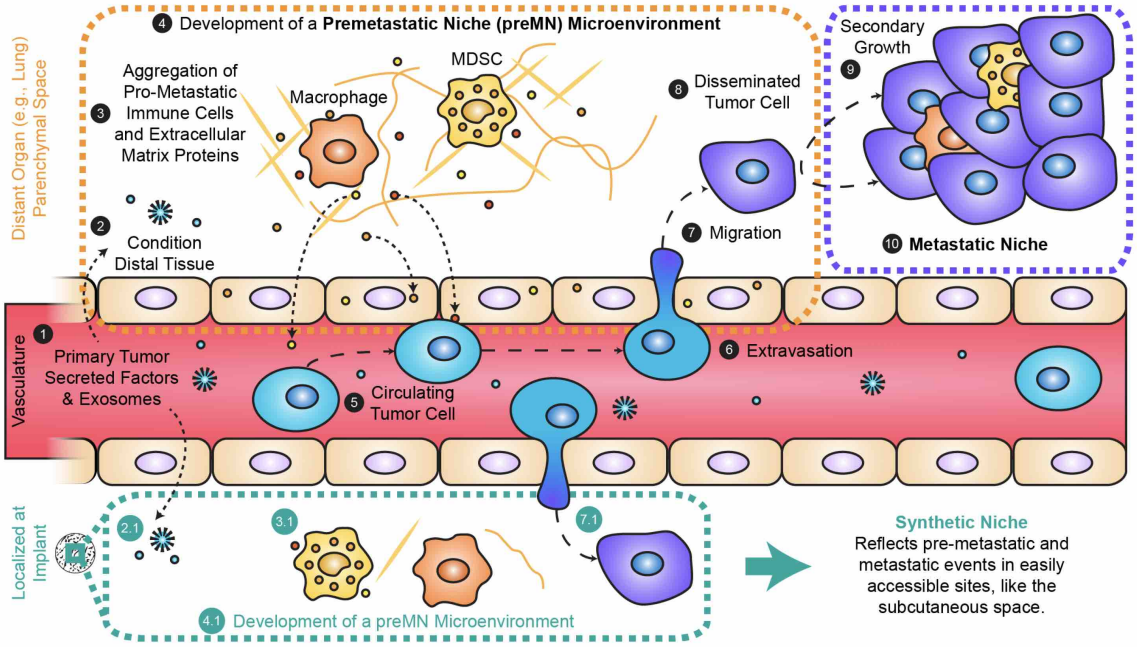

Figure 5.1: **Development of the pre-metastatic niche (preMN), metastatic niche (MN), and synthetic diagnostic site.** Circulating tumor cells exhibit a tropism for specific distal microenvironments, thus indicating that metastasis is pre-determined. Development of these predetermined sites is driven by (1) systemic conditioning from the primary tumor through secretion of factors and exosomes, which is amplified by simultaneous conditioning o the bone-marrow and alterations in bone-marrow derived cells. (2) This process conditions distal tissues and contributes to the (3) aggregation of pre-metastatic immune cells and extracellular matrix proteins. (4) These primed distal microenvironments are denoted as the preMN and facilitate homing then colonization of (5) circulating tumor cells which (6) extravasate and (7) migrate into distal organs where they may become a (8) disseminated tumor cells if the conditions are hospitable. This disseminated tumor cell may then undergo a phenotypic shift to initiate a (9) metastatic secondary growth, thus leading to development of a metastatic niche. Given that the preMN contains a unique mixture of soluble factors, extracellular matrix, stromal and immune cells (e.g., cancer-associated fibroblasts and myeloid-derived suppressor cells, MDSCs), it is reasonable that preMN function could be synthesized through the recapitulation these unique factors at a synthetic site *in vivo*. This rationale underpins the development of material based synthetic diagnostic site that (2.1) is conditioned, (3.1) populated by disease associated immune cells, (4.1) develops characteristics of a preMN, and (7.1) captures metastatic tumor cells.

tumor is focused on measurements taken prior to the initiation of firstline treatment of the primary tumor, which limits this approach to pretreatment predictions of disease progression. Liquid biopsies show promise, yet face challenges associated with low cell numbers, as well as phenotypic relevance, as approximately 0.01% of circulating tumor cells will become metastatic foci and circulating immune cells are distinct from those in distal tissue [127, 128, 129]. We and others have previously reported that biomaterial implants function as a synthetic metastatic niche, with recruitment of early metastatic cells that represent aggressive populations observed within the lung [20, 21, 22, 25, 130, 131, 132, 133, 134]. The development of the metastatic niche is driven by circulating acellular material from the primary tumor that alters the immune system of the host, including discrete sites in distal organs [2, 135, 136, 137]. These sites precede and support colonization by metastatic tumor cells (Fig. 5.1). The identification of the metastatic niche was enabled through mouse models of metastasis, which recapitulated the conditioning of distal sites and validated the long standing seed and soil hypothesis [8]. The metastatic niche develops, in part, from an influx of bone marrowderived cells, such as hematopoietic progenitor cells and myeloid-derived suppressor cells (MDSC), that differentiate within the distal sites and create a permissive metastatic site in target organs [2, 135]. Monitoring the natural metastatic niche could alter the course of therapeutic interventions, yet the potential is hindered because of metastatic niche formation in obscure and inaccessible locations within vital organs, such as the lung and the liver. A synthetic metastatic niche provides a technical solution by predefining sites in readily accessible locations.We tested the hypothesis that analysis of immune dynamics at biomaterial implants, functioning as a synthetic metastatic niche, would provide unique information that correlates with disease progression. The tissue within the implant

integrates with the host and is subsequently modified by disease onset and progression [138, 139]. Following implantation, a porous biomaterial scaffold supports cell infiltration, vascularization, and the persistent recruitment of immune cells due to the localized foreign body response to the material [140]. The initiation of cancer metastasis is associated with systemic alteration of immune responses, which we hypothesize also alters the composition of the foreign body response [141]. In the context of cancer progression, the immune response at an implanted microporous polymer scaffold would acquire immunosuppressive trademarks, thus mimicking the properties of disease-targeted organs. We propose to analyze the immune cell composition and phenotype to draw correlations with disease progression, while sparing vital organs or other sites from invasive sampling. For cancer metastasis, this scaffold could advance disease detection capabilities by providing a predefined site that indicates an altered immune environment and disease progression in vital organs [2]. Identifying early metastatic events has the potential to inform a new generation of therapeutic approaches that target the earliest stages of metastatic disease.

5.4 Results

5.4.1 Metastatic disease alters gene expression at implants as a function of disease severity

We performed a high-throughput gene expression analysis of immune pathways to characterize the dynamics at a biomaterial implant that recruits metastatic cells, throughout the process of disease progression. We and others have shown that metastatic tumor cells colonize microporous implants, yet are vastly outnumbered by other cell types including stromal, immune, and epithelial cells [20, 21, 22, 130, 131]. Microporous implants (5-mm diameter, 2-mm thickness, interconnected 250-425 mm

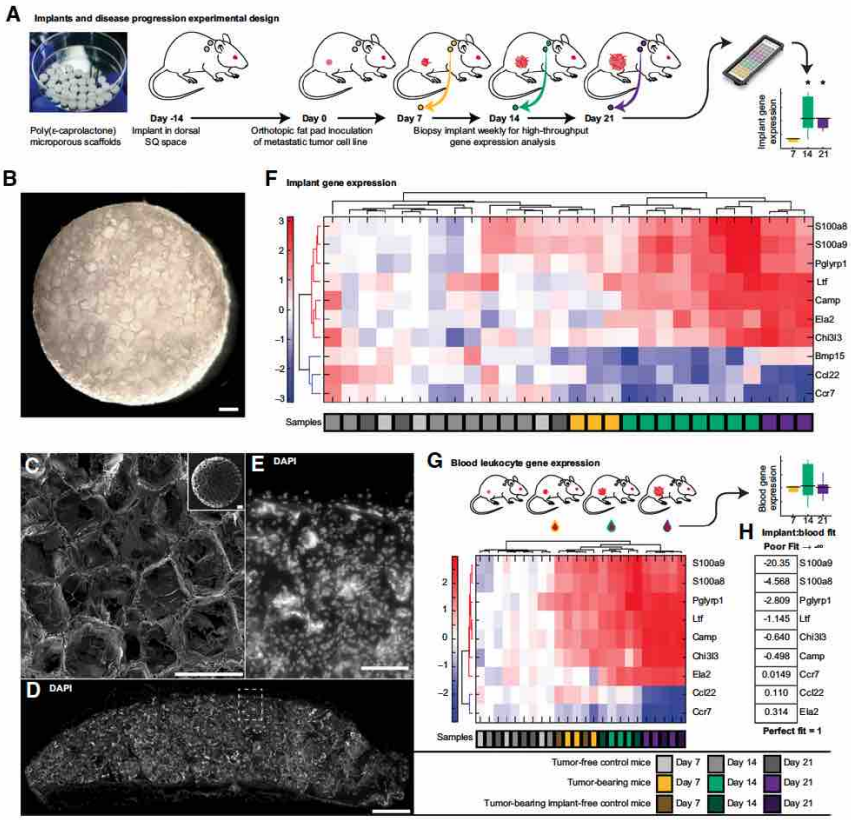

Figure 5.2: **Microporous polymer scaffolds support host tissue integration when implanted, which is then progressively modified as a function of disease burden and presents unique dynamics compared with blood.** (A) PCL scaffolds and experimental timeline for scaffold implantation, tumor inoculation, implant biopsies, and high throughput gene expression analysis. (B) and (C) Representative macroscopic and SEM images of PCL scaffold illustrating microporous architecture. Scale bar, 500 μm and interconnected 250425 μm pores. (D) DAPI staining illustrates dense and uniform cellularity throughout the implant. Scale bar, 500 μm. Highlighted area (dashed box) indicates region of higher magnification (E). Scale bar, 100 μm. (F) Progressive gene expression changes in tissue biopsied from implants during metastatic disease course. BALB/c mice were implanted with microporous polymer implants (day -14), then inoculated with syngeneic 4T1 tumor cells at day 0. Implants were biopsied at days 7, 14, and 21 and tissue was analyzed with a high-throughput qRT-PCR platform (OA, 632 target and 16 reference genes). The heatmap illustrates unsupervised hierarchal clustering of the 10-gene panel,with expression levels for each gene depicted as standardized data (n=14 per condition). Cohort size at days 7 (n=3), 14 (n=8), and 21 (n=3) represent different mice as biological replicates. (G) BALB/c leukocytes were isolated from blood of tumor-bearing mice, gene expression profiled, and compared against tumor-free and implant-free control mice. Many of the genes in the panel showed significant differences in the same directionality as those in the implant. (H) The heatmap shows differences in dynamics between the implant to blood gene expression ratio and the goodness of fit for this relationship between days 7 and 21. Fit for the regression analyses was determined by normalized root mean squared error, where negative values indicate a worse fit and a value of 1 indicates a perfect fit. S100a9, S100a8, Pglyrp1, and Ltf had the worst fits when comparing implant with blood. Bmp15 is not shown as it was not measurable in blood.

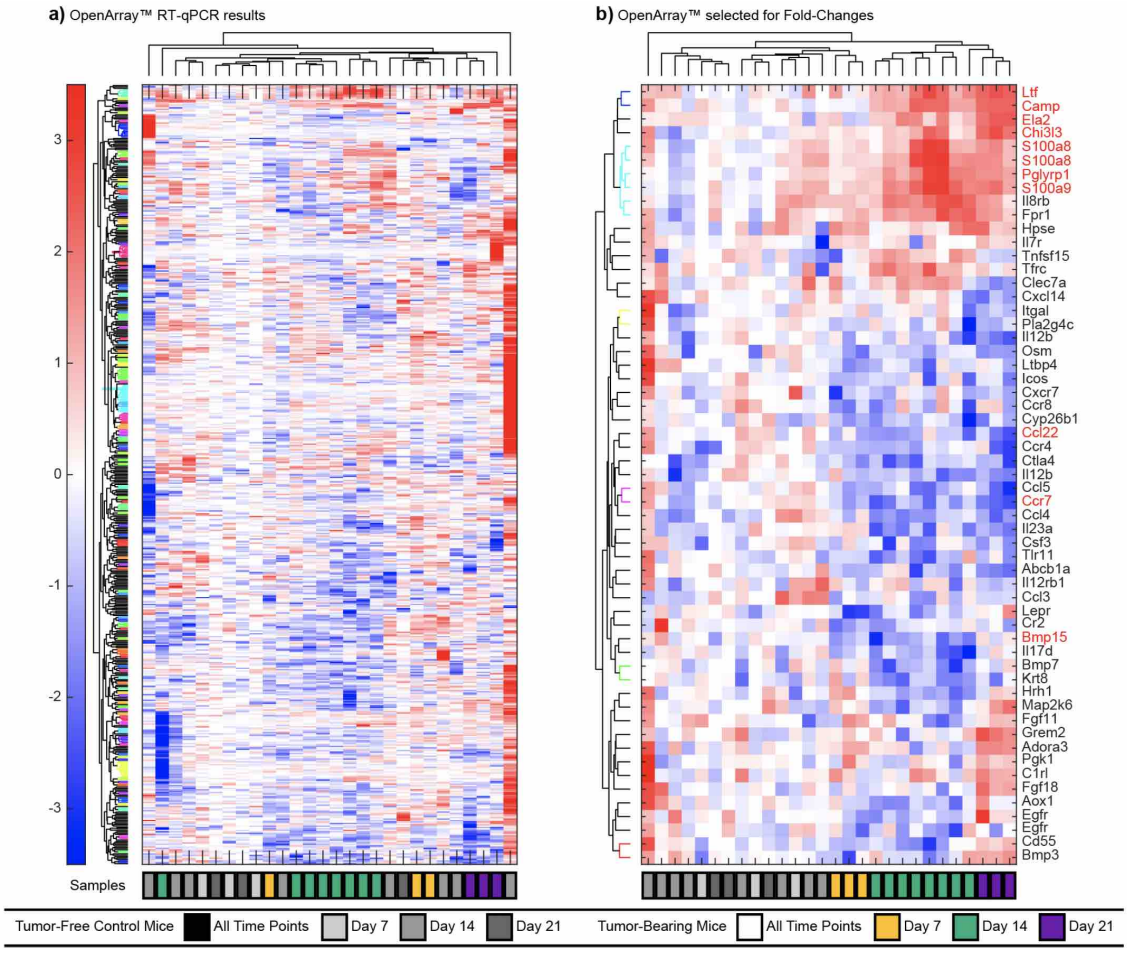

Figure 5.3: **Experimental designs and OpenArray™ output for select genes with high fold-change and predictive value.** (A) Results from OpenArray for TB mice at Days 7 (n=3), 14 (n=8), and 21 (n=3) along with time-matched TFC mice (n=14). (B) Results from OpenArray selected for fold change TFC or TB. For panels (B)-(C) mice are indicated on x-axis and genes are indicated on y-axis with clustering done via Euclidian distance and average linkage. Genes indicated in red text on the y-axis were selected for the smaller 10-gene panel analysis is subsequent studies.

pores) composed of PCL (Fig. 5.2A and B), were inserted into dorsal subcutaneous space of BALB/c mice to allow for tissue ingrowth. Microporous PCL scaffolds (Fig. 5.2C) facilitate the longitudinal studies herein by provide greater implant stability compared with more rapidly degradable polymers like poly(lactide-co-glycolide) [22]. This microporous architecture facilitated cell colonization throughout the thickness of the implant (Fig. 5.2D and E). After 2 weeks, mice were orthotopically inoculated (day 0) with triple-negative 4T1 tumor cells. At weekly intervals (days 7, 14,

and 21), tissue from implants was biopsied and changes in the gene expression were screened via a high-throughput qRT-PCR platform, OA (Fig. 5.2A). This screening assessed the expression of 632 target and 16 reference genes per sample in parallel (Fig. 5.3A). Gene expression from the biopsied implants of tumor-bearing mice was compared against time-matched tumor-free control mice that had implants yet were not inoculated with 4T1 cells. Altered expression was observed for 113 genes following tumor inoculation. To focus our studies, a panel of 10 genes was identied on the basis of fold change (Fig. 5.3B), level of signicance (FDR corrected), and expression stability. The 10 target genes (Fig. 5.2F; Fig. 5.4A) were normalized against an average expression of 5 reference genes. As a function of disease progression (Fig. 5.4B), expression increased for 7 of the 10 genes within the implant, including: S100 Calcium Binding Protein A8 (*S100a8*), S100 Calcium Binding Protein A9 (*S100a9*), Peptidoglycan Recognition Protein 1 (*Pglyrp1*), Lactotransferrin (*Ltf*), Cathelicidin Antimicrobial Peptide (Camp), Elastase 2 (Ela2), Chitinase (Chi3l3). Expression decreased for 3 of the 10 genes within the implant, including: Bone Morphogenetic Protein 15 (*Bmp15*), C-C Motif Chemokine Ligand 22 (*Ccl22*), and C-C Motif Chemokine Receptor 7 (*Ccr7*). Unsupervised hierarchical clustering of the expression of these genes in the implant-derived tissue produced a separation between tumor-bearing and tumor-free control cohorts. Over time, the gene expression in the tissue inltrate of tumor-bearing mice progressively separated from tumor-free controls with day 7 expression being most similar to tumor-free mice. No structured or time-based organization was observed in the gene expression from the tumor-free controls, presumably due to the microenvironment stability in healthy mice. Clustering also identied distinct gene groups (i.e., *S100a8/S100a9/Pglyrp1*) that displayed similar expression patterns.

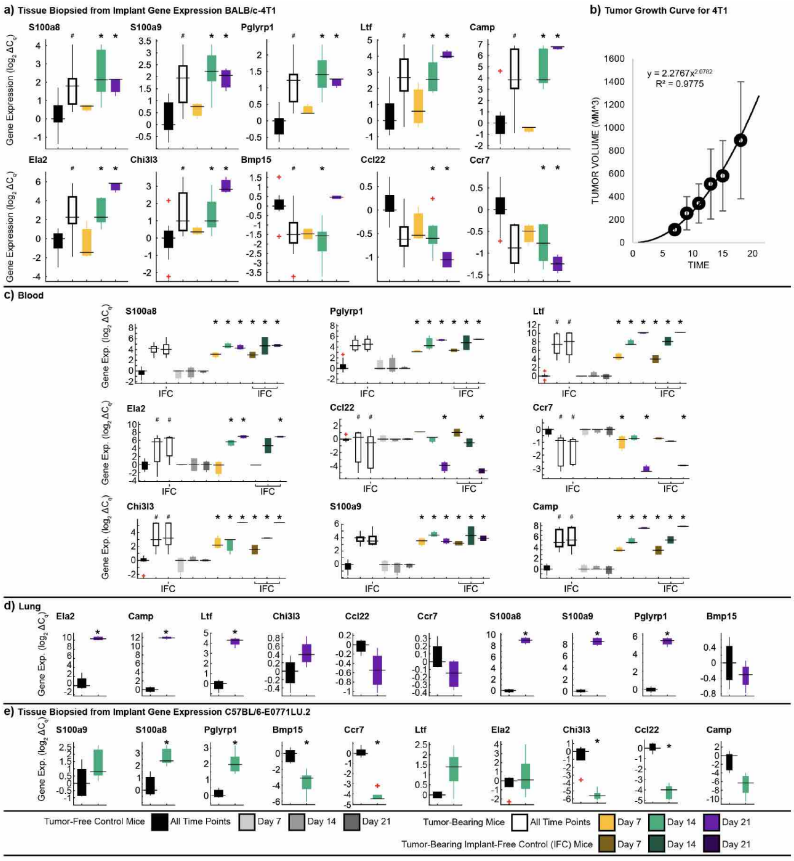

Figure 5.4: **Statistical plots to support heatmaps in main text and supplementary materials.** (A) Box plots for gene panel heatmap in Fig. 5.2F show the median, 25th-75th percentiles and most extreme data points that were not considered outliers (outliers are visually indicated by red). TB cohort expression is centered relative to the time-matched TFC cohort median. Scale depicts the log2-transformed fold change. A two-way MANOVA showed a significant interaction effect between condition and time (Pillais Trace=1.276, F(20,28)=2.465, p=0.014). Post hoc univariate ANOVA showed significant differences within the f diseased cohort over time (indicated by #, df=(2,22), p<0.05). Simple effects analysis showed significant differences between diseased and time-matched TFC (indicated by , idák adjusted p<0.05 adjusted). (B) Tumor growth curve for 4T1 mice starting at Day 7, with a power regression line, error bars are standard deviation. (C) Box plots of gene expression to support the data in the C57BL/6-Lu.2 heatmap in Fig. 5.5B. indicates significance (Dunn-Šidák corrected to p<0.005) from independent two-tailed t-tests comparing TB to TFC (n=5 per condition). (D) Box plots of gene expression for blood data to support the heatmap found in Fig. 5.2. Tumor-bearing Implant Free Controls (IFCs) are shown to illustrate that the implants do not alter the gene expression of blood leukocytes. A two-way MANOVA showed a significant interaction effect between condition and time (Pillais Trace=2.527, F(36,40)=1.907, p=0.024). Post hoc univariate and simple effects analysis showed significant differences within the diseased cohort over time as indicated as # (df=(2,15), p<0.001) and indicates significant differences compared to time matched controls (Šidák adjusted p<0.05 adjusted). (E) Gene expression data from the lung tissue heatmap in Fig. 5.5A. indicates significance (Dunn-Šidák corrected to p<0.005) from independent two-tailed t-tests comparing TB to TFC (n=4 per condition).

The 10-gene panel was then analyzed in blood leukocytes isolated from blood at multiple time points following tumor inoculation to identify correlations or unique dynamics in synthetic niche. Liquid biopsies represent a relatively accessible source to analyze the intermediary stages of metastasis that occur between the primary tumor and distant metastatic sites. Most genes (except *Bmp15*) analyzed in the implant-derived tissue were expressed in the blood (Fig. 5.2G; Fig. 5.4C), yet their expression dynamics differed from those of the implant. This difference was particularly evident for the genes *S100a9*, *S100a8*, *Pglyrp1*, and *Ltf*. At the implant, expression of these genes progressively increased over time, which aligned with the progression of disease. In the blood, expression of these genes was stable and lacked a correlation with disease progression, illustrated by a goodness-of-t analysis in which *S100a9*, *S100a8*, *Pglyrp1*, and *Ltf* had the poorest alignment between the implant and blood (Fig. 5.2H). In contrast, gene expression for *Ela2* and Camp progressively increased in both the implant and blood. Collectively, the data acquired from blood does not directly correlate with the synthetic niche, indicating that synthetic niche provides distinct information that has the potential to complement liquid biopsy.

5.4.2 Disease-driven differences at the implant have unique dynamics and are reective of distal organs

The 10-gene panel was analyzed in diseased lung tissue to determine whether the synthetic niche correlates with native metastatic sites in distal organs. The lung is normally the primary metastatic site for 4T1 cells, and we thus analyzed lung biopsies from tumor-bearing and tumor-free control mice for comparison with synthetic niche. The gene expression patterns for the 10-gene panel in the lung at day 21 following tumor inoculation (Fig. 5.5A; Fig. 5.4D) was highly aligned

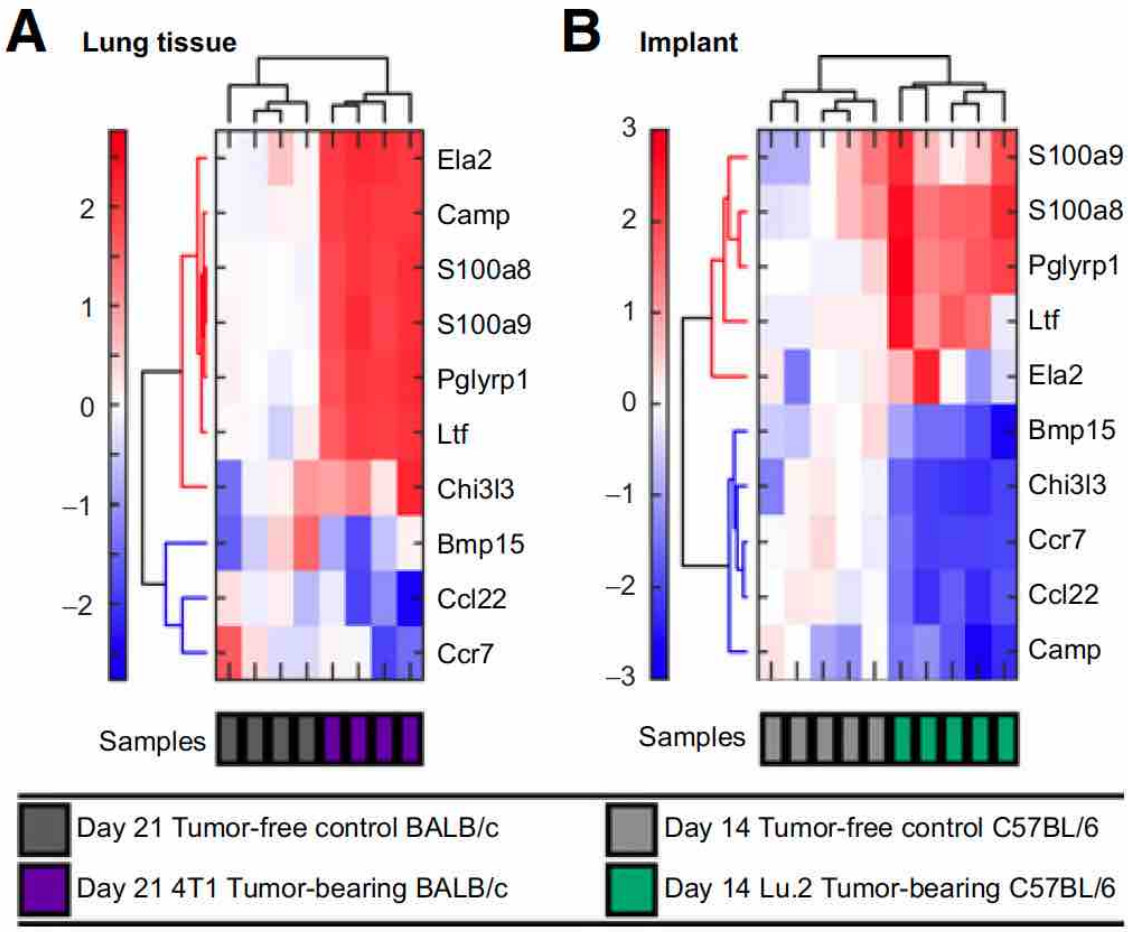

Figure 5.5: **Tissue biopsied from implants is indicative of diseased lung.** (A) BALB/c mice orthotopically inoculated with 4T1 tumor cells at day 0 had lung tissue biopsies taken and qRT-PCR analyzed at day 21 from tumor-bearing and tumor-free control mice. Heatmap of gene expressions from lung tissue of tumor-free control and tumor-bearing mice. Organization was based on unsupervised clustering of samples and genes. (B) Tissue biopsied from implants in C57BL/6 was analyzed for gene expression in tumor-free and tumor-bearing mice that were inoculated with a lung-tropic, syngeneic metastatic cell line. C57BL/6 mice were implanted with microporous PCL scaffolds (day -14) and then orthotopically inoculated with a metastatic derivative (developed through serial inoculations of explanted lung metastases) of the E0771 syngeneic line (day 0). At day 14, scaffolds were biopsied from tumor-bearing and tumor-free control mice. Heatmap of gene expressions for a 10-gene panel normalized to reference genes, centered on the healthy tumor-free control median, and standardized. Organization is based on unsupervised clustering of samples and genes.

with that observed in the implant. Notable is that all 7 genes upregulated in tissue biopsied from synthetic niche are clustered in the lung data. Similarly, the 3 genes downregulated in the tissue biopsied from implants are clustered in the lung data. These measurements of tissue taken from the lung were consistent with data from other studies regarding metastatic niche development and the phenotype of MDSCs in distal tissues during metastasis [137]. Collectively, the gene expression patterns of the synthetic metastatic niche reect the patterns observed in native metastatic niche.

We developed a lung-tropic tumor cell line for C57BL/6 as an additional immunocompetent model of lung-biased metastasis to determine whether the expression panel may reect lung metastasis. To match the aggressive and lung-tropic metastasis of the BALB/c-4T1 model, we developed an aggressive variant of the E0771 cell line through serial inoculation of lung metastases. This aggressive and lung-tropic E0771 variant, denoted as Lu.2, was inoculated in C57BL/6 mice implanted with the polymer scaffolds. This experiment also used an orthotopic inoculation of tumor cells into the mammary fat pad, which maintained the experimental design of a primary tumor conditioning distal sites and spontaneous metastasis. The C57BL/6-Lu.2 had similar gene expression changes and clustering to the lung tissue from the BALB/c-4T1 model (Figs. 5.2C and 5.5A), with 80% (8/10) of altered genes progressing in a similar direction (Fig. 5.5B; Fig. 5.4E). The two genes that demonstrated a difference in expression (Camp and Chi3l3) may be due to the slower progression of disease that we observed in the B6-Lu.2 model, yet additional studies would be necessary to fully understand the impact of mouse strain and cell line metastatic potential on distal conditioning. Our data illustrates that the synthetic niche consistently mimics and serves as a sentinel for metastatic conditioning of lungs.

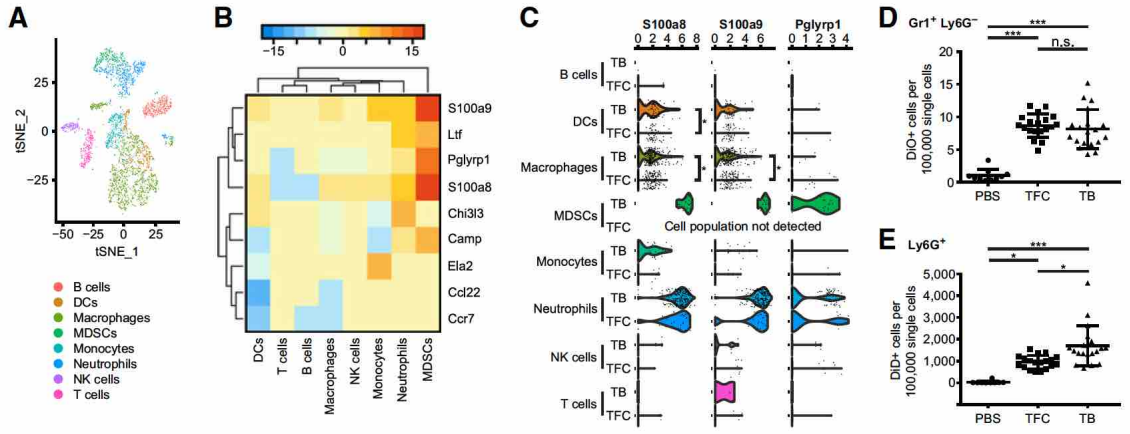

Figure 5.6: **Select innate immune populations drive phenotypic changes within the synthetic niche.** At day 14, immune populations within the scaffolds of tumor-free control (TFC) and tumor-bearing (TB) mice were profiled by scRNA-seq, with a focus on the 10-gene panel derived from analysis of the whole microenvironment. (A) T-distributed Stochastic Neighbor Embedding (tSNE) plot of innate and adaptive immune cells analyzed in implants during disease progression. (B) Heatmap and unsupervised hierarchical clustering of aggregated gene expression of the total immune cell population in the tumor-bearing models. This data represents the expression level of a gene in a specific cell type as compared with other cell types (e.g., cumulative MDSCs express the highest amount of S100a8 and S100a9 compared with all other cell types). (C) Violin plots of single-cell gene expression from tumor-free control and tumor-bearing mice including B cells, DCs, macrophages, monocytes, neutrophils, natural killer (NK) cells, and T cells. Each dot represents the gene expression (x-axis) of a single cell within a cell type and health state (tumor-bearing or tumor-free control; y-axis). Bmp15 is absent as it was undetected using scRNA-seq. (D) and (E) Immune cells adoptively transferred from tumor-bearing mice readily infiltrate implants of tumor-free control and tumor-bearing mice. $Gr1^{+}Ly6G^{-}$and $Ly6G^{+}$ immune cells were isolated from spleens of tumor-bearing mice through magnetic-activated cell sorting, then labeled with DiO orDiD, respectively. Labeled immune cells were adoptively transferred into tumor-free control or tumor-bearing mice implanted with scaffolds. For tumor-bearing mice, tumors were inoculated 7 days prior to adoptive transfer, where approximately 30 tumor cells were expected in implants. An injection of PBS was used as an unlabeled control to establish the analytical background [22]. Adoptively transferred DiO-labeled $Gr1^{+}Ly6G^{-}$cells (D) and DiD-labeled $Ly6G^{+}$ cells (E) readily trafficked into implants in tumor-free control and tumor-bearing mice. One-way ANOVA and post hoc *Šidák* multiple comparisons analysis with significance indicated as $*$, $P<0.01$; $***$, $P<0.0001$; n.s., not significant.

5.4.3 Select immune populations dictate alterations in the implant microenvironment during metastasis

We next investigated the gene expression of innate and adaptive immune cells (Fig. 5.6A) within implants during cancer metastasis to determine the cell types driving metastatic conditioning of the synthetic niche. Single-cell RNA-sequencing (scRNA-seq) was employed to investigate cell-specic gene expression. Our data supports previous studies that MDSCs are a driving force of immunosuppressive *S100a8/9* [137] MDSCs had increased expression of *S100a8*, *S100a9*, *Pglyrp1*, and *Ltf* relative to the other cell types (Fig. 5.6B). Specically, emphPglyrp1 was 1.8-fold higher in MDSCs than other neutrophils from implants of tumor-bearing mice. The scRNA-seq data are consistent with our previous data, showing an inux of MDSCs to the implant, and current literature on MDSC phenotype [142]. Interestingly, when the gene expression was normalized to the number of cells in each population, a phenotypic shift was observed. *S100a8* was signicantly upregulated in dendritic cells (DC) of tumor-bearing mice and *S100a8* and *S100a9* were signicantly upregulated in macrophages of tumor-bearing mice, relative to their tumor-free counterparts (Fig. 5.6C; Fig. 5.7A and 5.7B). This phenotypic shift in antigen-presenting cells, which reside as sentinels in tissues, suggests that multiple branches of the myeloid lineage are inuenced by primary tumor conditioning of distal sites [143]. In our data, diseased neutrophils cluster closely with MDSCs as they are also a source of *S100a8*, *S100a9*, *Pglyrp1*, and *Ltf*. However, individual neutrophils did not signicantly change their expression of these genes, yet overall increases from neutrophils at the implants were observed because of their increased cell numbers following the onset of metastasis (Fig. 5.6C). The scRNA-seq data indicates that the genes most associated with

MDSC phenotype (Fig. 5.6B) were also those genes that poorly aligned with blood leukocyte gene expression (Fig. 5.2H). Perhaps this is supported by previous studies showing that MDSCs can activate within metastatic niche distal sites [135], similar to our scRNA-seq data showing that a phenotypic shift occurs in antigen-presenting cells within the synthetic niche (Fig. 5.6C). This data on phenotypic shift of myeloid lineage cells in tissue biopsied from implants underlies the function of synthetic niche.

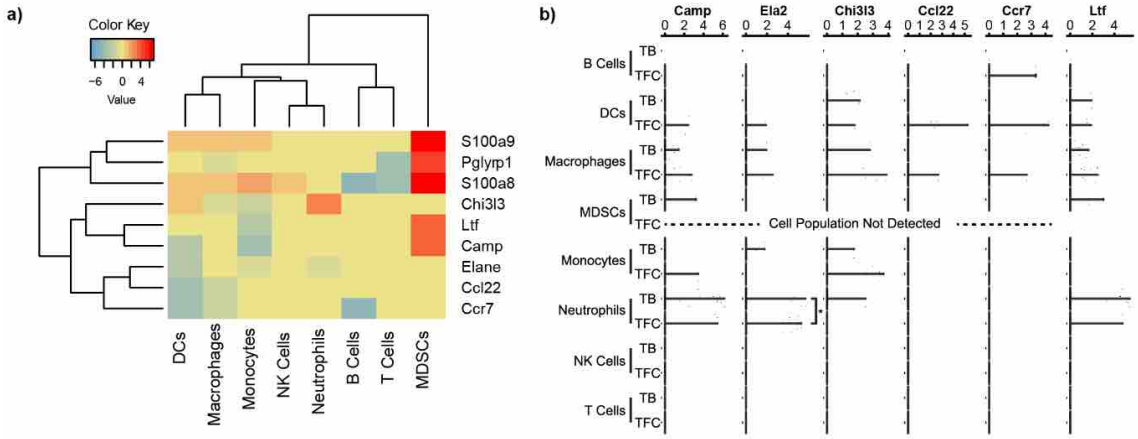

Figure 5.7: **Additional scRNA-seq plots of the gene panel analyzed in Fig. 5.6.** (A) Heatmap of fold-change between scaffolds in tumor-bearing mice and tumor-free controls. Data is analogous to that presented in Fig. 5.6C and Fig. 5.7B violin plots. (B) Violin plots of single-cell gene expression from TFC and TB mice including B cells, dendritic cells (DCs), macrophages, monocytes, neutrophils, natural killer (NK) cells, and T cells. Each dot represents the gene expression (x-axis) of a single cell within a cell type and health state (TB or TFC, y-axis). Bmp15 is absent as it was undetectable by scRNA-seq.

The trafficking of innate immune cells to implants was investigated for its dependence on primary tumor conditioning of the implant. We adoptively transferred puried $Gr1^{+}Ly6G^{-}$and $Ly6G^{+}$ cells (isolated from tumor-bearing mice) into tumor-free control and tumor-bearing mice that had implanted scaffolds. $Gr1^{+}Ly6G^{-}$and $Ly6G^{+}$ cells were labeled prior to transfer with DiO and DiD lipophilic dyes, respectively. Scaffolds were analyzed for labeled immune cells at 36 hours after the transfer. Both labeled immune cell populations were present in implants of the tumor-free control and tumor-bearing mice at an equal order of magnitude. Compared with

PBS controls, transferred $Gr1^{+}Ly6G^{-}$cells were increased by 8.4-fold and 7.9-fold in tumor-free control and tumor-bearing mice, respectively (Fig. 5.6D). Transferred $Ly6G^{+}$ cells were increased by 31-fold and 55-fold in tumor-free control and tumor-bearing mice, respectively (Fig. 5.6E). These results suggest that the foreign body response to the material largely determines immune recruitment to the scaffold, as supported by previous studies [20, 134], and that the preexisting condition of the implant does not selectively control immune cell trafcking at the implant. Thus, the similarities in trafcking and phenotypic shifts in the scRNA-seq data illustrate that the synthetic niche provides both a predened site for disease-conditioned immune cells to aggregate, then further differentiate into metastasis-supportive populations.

5.4.4 Gene expression signatures monitor disease progression

We next developed a scoring system from our 10-gene panel that represented the progression of metastatic conditioning in tumor-bearing mice. We applied computational approaches to derive single-metric scores based on gene expression signatures from the tissue of biopsied implants, and thereby develop a predictive model for the probability that a mouse was either tumor bearing or a tumor-free control (Fig. 5.8). The computational reduction of gene expression signatures from primary tumor tissues to single-metric scores and predictions has guided clinical management of patients with breast cancer [144]. Two computational techniques were investigated in parallel (Fig. 5.9) as a spectrum of regression and modeling approaches provides a more robust interpretation of data and biological networks [145]. First, data dimensionality was reduced via an unsupervised matrix factorization (singular value decomposition, SVD) [146], which linearly transformed the data into eigengenes and eigenarrays that indicate gene signicance and sample grouping, respectively. The

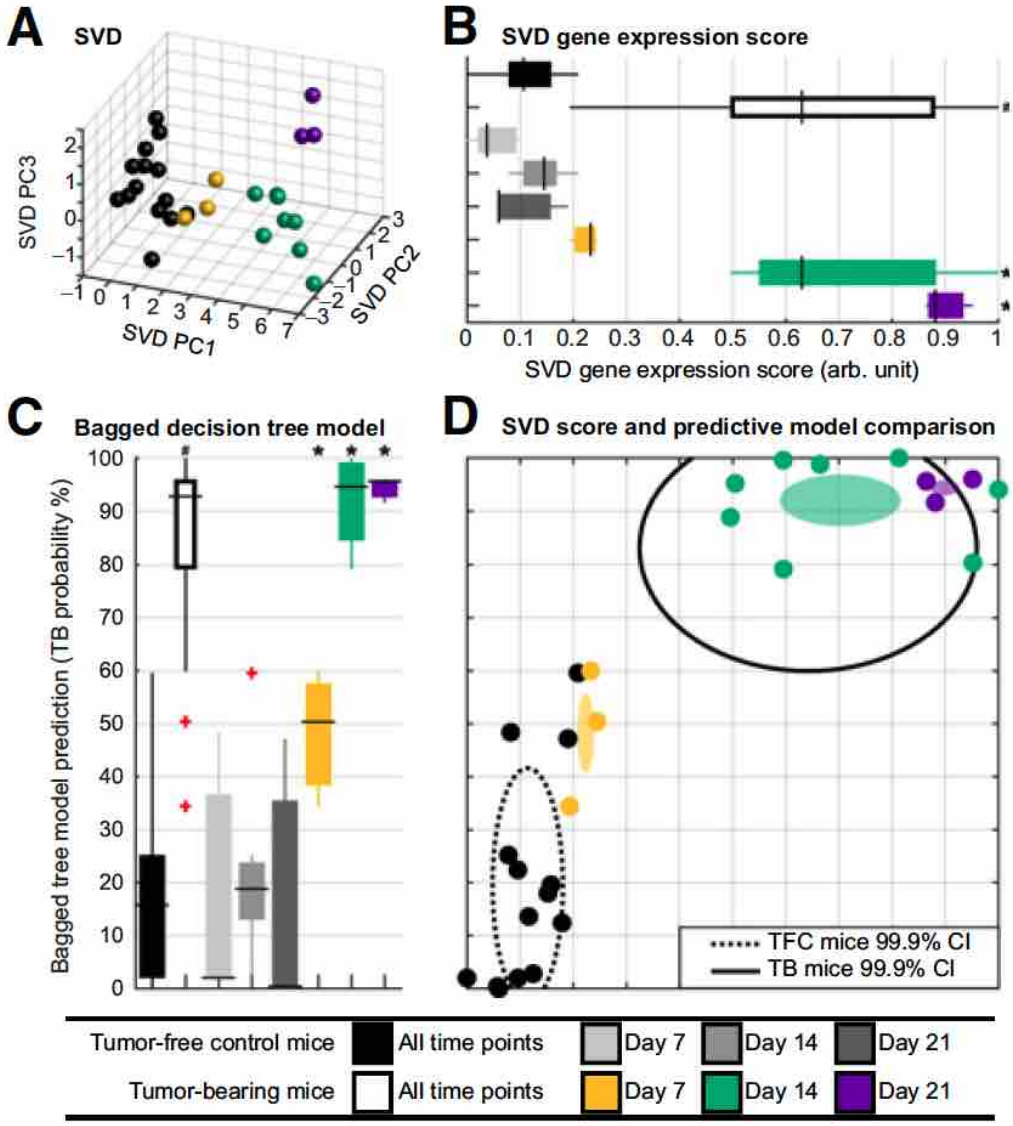

Figure 5.8: **Gene expression signatures reduced to scoring metrics and diagnostic predictions.** (A) and (B) Gene expression from analysis of implant-derived tissue was reduced to an unsupervised scoring metric through SVD, which was converted to a score by calculating Euclidean distance from the tumor-free control centroid to each sample. Scores were scaled between 0 and 1. (C) In parallel, gene expression data were used to train a bootstrap aggregated (bagged) decision tree ensemble with leave-one-out cross-validation to predict the likelihood that a mouse was tumor bearing. (D) Plot of the SVD score versus the bagged tree prediction. Dashed and solid line ellipses indicate the 99.9% confidence intervals for tumor-free control (TFC; n=14) and tumor-bearing (TB; n=14) cohorts, respectively. Filled ellipses indicate average and SEM for bagged tree and SVD data at days 7 (n=3), 14 (n=8), and 21 (n=3). A two-way MANOVA showed a significant interaction effect between condition and time [Pillai trace=0.568, $F(4,44)=4.361$, $P=0.005$]. Post hoc univariate ANOVA showed significant differences within the diseased cohort over time [indicated by #, df=(2,22), $P<0.001$]. Simple effects analysis showed significant differences between tumor bearing and time-matched tumor-free controls (indicated by $*$, *Šidák* adjusted $P<0.05$).

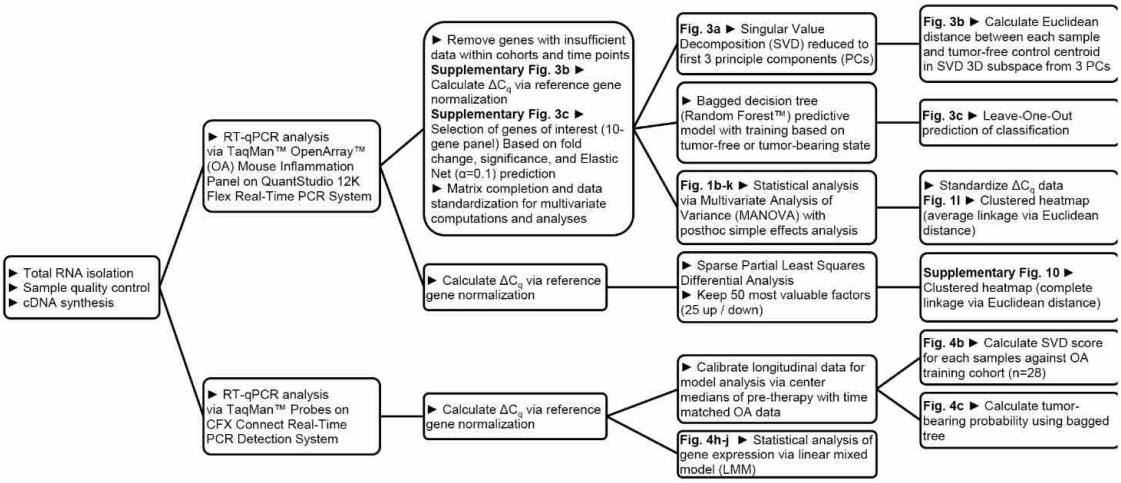

Figure 5.9: **Experimental timeline, gene expression analysis, singular value decomposition, and bagged decision tree analysis and computational pipelines.** Map of computational processes and the data outputs that are represented in the manuscript. For example, the calculation of the Euclidean distance from the principle components of the singular value decomposition (SVD) represented in Fig. 5.8B can be traced back through its processing steps to the total RNA isolation, quality control, and cDNA synthesis.

SVD separation of the samples in three-dimensional subspace (Fig. 5.8A) established a scoring metric by setting a reference point at the centroid of the tumor-free controls and calculating Euclidean distance to each sample data point (Fig. 5.8B; x-axis of 5.8D), scores are scaled between 0 and 1. Second, supervised machine learning created a predictive model via a bootstrap aggregated (bagged) decision tree ensemble (i.e., random forest) [147], which used a forest of decision trees based on a random selection of a gene from the 10-gene panel to predict a mouse status as tumor free or tumor bearing. For each sample, a prediction score (Fig. 5.8C; y-axis of 5.8D) was determined via leave-one-out analysis. In all models, the scores in tumor-bearing mice increased over time and corresponded with disease progression, while the scores in tumor-free control mice remained consistent (Fig. 5.8D). Thus, the metastatic conditioning of the implant was formulated into a trained model for monitor disease progression.

5.4.5 Monitor response to surgical excision and early identication of responders

We subsequently investigated the regression of disease following therapy to test and validate the disease-monitoring capabilities of the synthetic niche. Gene expression of synthetic niche was proled following excision of the tumor-bearing mammary gland. This procedure (analogous to a mastectomy in humans) was chosen as the intervention based on the role of surgery as a rst-line treatment for breast cancer. We have previously reported that surgery alone in mice receiving scaffolds resulted in 40% long-term survival, while the remaining mice recurred [22]. Following synthetic niche proling, samples were then classied on the basis of the model developed in Fig. 5.8. Note, this study serves as validation because the trained model is based on progression of disease burden, while the test analysis is based on disease regression.

Fourteen days following 4T1 tumor inoculation in BALB/c mice, tissue from the implant was biopsied (day 0 in Fig. 5.10A) and then immediately followed by an excision of the tumor-bearing mammary gland. Tumor-free control mice had a similar excision of the mammary gland. Implant biopsies were performed at weekly intervals following mammary gland excision (days 7, 14, and 21 post-excision in Fig. 5.10). Gene expression from the biopsies was quantied, and scores were derived from tumor-free control or tumor-bearing mice. Scores for each tumor-bearing animal showed a redirection toward the tumor-free control baseline 7 days after surgery for all mice (Fig. 5.10B). This difference was most evident at day 7 for the SVD (Fig. 5.10C) and at day 21 for the bagged tree prediction (Fig. 5.10D), with this difference originating from the distinct weighting of specic genes in the two computational approaches. We noted increased variability of scores at later time points with the SVD, which prompted an investigation of these metrics as a function of outcome.

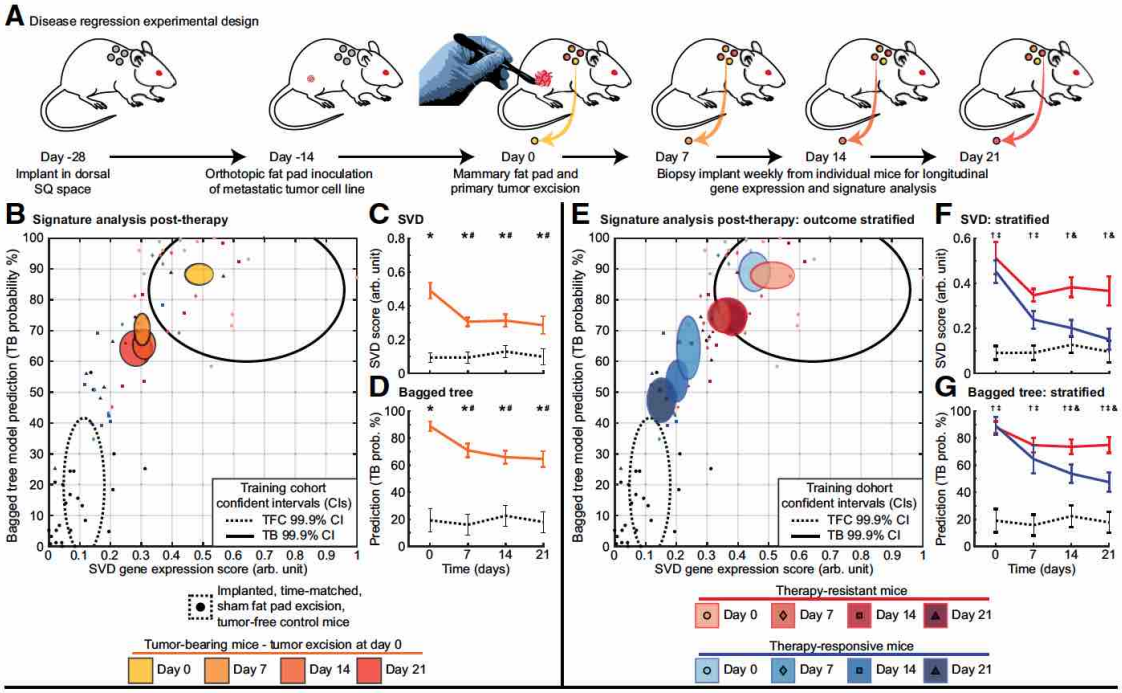

Figure 5.10: **Primary tumor excision redirects signature and score trajectories, which predicts therapeutic efficacy.** (A) Mice with an array of implants and a primary tumor in their 4th mammary fat pad (n=15 mice) had an implant surgically biopsied, then immediately had their primary tumor resected along with the surrounding fat pad (day 0, tumor burden equivalent to day 14 in Figs. 5.2 and 5.6). Tumor-free control (TFC) mice (n=7) received sham inoculation with PBS and a mammary gland excision. All mice where then monitored by weekly (days 7, 14, and 21) biopsy of tissue from the implant, then analyzed by qRT-PCR and reduction to a predictive score. (B)-(D) Signature analysis using the SVD and bagged tree algorithm that had been trained on the disease-progression group (Fig. 5.8) was used to classify each sample. Both SVD and bagged tree exhibited downward trends in the tumor-bearing cohort (n=15) following therapeutic tumor resection. Next, the analysis was stratified on the basis of classification as therapy resistant (n=9) or responsive (n=6), as determined by survival monitoring following excision of the primary tumor. (E)-(G) The predictive scores indicated a significant divergence between the resistant and responsive mice. Filled ellipses indicate the average and SEM for the bagged tree and SVD data at days 0, 7, 14, and 21. The cohort size for each group was decreased by one at day 21 due recurrence and animal censorship. For longitudinal data, statistics were performed via a linear mixed model. Post hoc simple effects analysis indicates significant differences ($P<0.05$) between tumor-free control ($*$) and tumor bearing (TB; collective, not stratified by outcome), tumor bearing and tumor bearing day 0 (preexcision;), tumor-free control and resistant (†), tumor-free control and responsive (), and resistant and responsive following significant (; $P<0.05$) or trending ($P<0.1$) interactions in a two-way ANOVA.

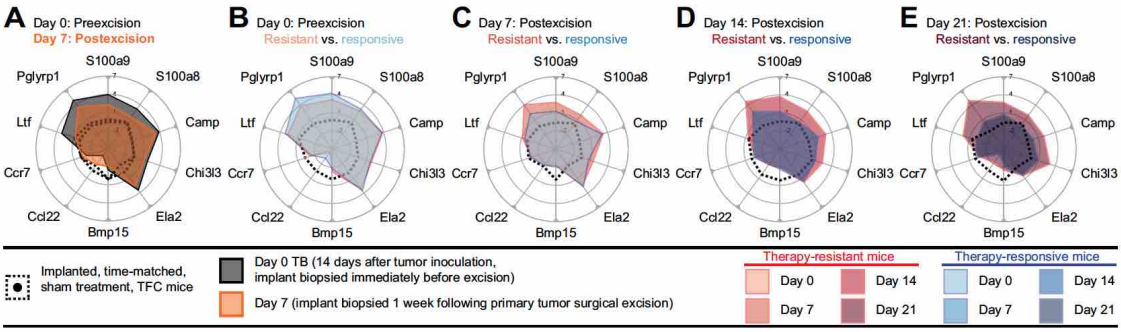

Figure 5.11: **Gene expressions corresponding to the post-therapeutic signature analysis shows a cumulative regression toward a tumor-free state following tumor resection and a subsequent bifurcation between several genes as a function of therapeutic outcome.** (A) For the 7 genes that showed an increased expression in the metastatic onset model (Fig. 5.5), there was an organized regression in expression 1 week after therapy. Tumor-free control (TFC), n=7; tumor-bearing (TB) mice, n=15. (B)-(E), Radar plots illustrate the bifurcation of specific genes as a function of therapeutic outcome, as determined by survival monitoring following excision of the primary tumor. While the decrease in expression continued for several genes, other genes like S100a8, S100a9, Pglyrp1, andLtf showed a rebound and increase in the resistant cohort after the initial decrease. tumor-free control, n=7; resistant, n=9; and responsive, n=6.

Scores were stratified on the basis of survival or recurrence outcomes (Fig. 5.10E-G). For mice that survived long-term post-excision, the regression toward the tumor-free control baseline continued over the subsequent 2 weeks (days 14 and 21 post-surgery), with no signs of recurrence through day 48. However, for the mice that developed disease recurrence, the scores remained signicantly elevated above the tumor-free control baseline and signicantly deviated from the scores of mice that survived long term. In the predictions obtained from the bagged decision tree, the average scores for mice that survived consistently indicated a lower degree of disease conditioning. The redirection in score and prediction trajectories of Fig. 5.10 is attributable to specic changes in gene expression. All genes from the panel with increased expression during tumor progression (*S100a8*, *S100a9*, *Pglyrp1*, *Camp*, *Ltf*, *Chi3l3*, and *Ela2*) regressed toward the tumor-free control baseline following tumor-

bearing mammary gland excision (Fig. 5.11A). Interestingly, the three genes strongly associated with MDSC cell phenotype in our scRNA-seq data (*S100a8*, *S100a9*, and *Pglyrp1*; Fig. 5.6B), also demonstrated a pronounced separation between mice that remained disease free and those animals that developed a recurrence (Fig. 5.11B-E; Fig. 5.12A-K). An interesting connection between data in Figs. 5.2F, 5.2H, 5.8B, and 5.11A-E is that *S100a8*, *S100a9*, *Pglyrp1*, and *Ltf* cluster together during disease progression, have the weakest correlation with blood, are upregulated in MDSCs, and are the earliest and most consistent predictors of survival in the therapeutic model. Results from the signature analysis, reduction to single-metric scores, and the gene expression components demonstrate that tissue from biopsied implants are a platform for monitoring context-specic pathological states.

5.5 Discussion

The synthetic metastatic niche is based on engineering a tissue within a porous scaffold that is inserted subcutaneously and is thus readily accessible for analysis, allowing for longitudinal monitoring without risk to a solid organ. Following treatment with surgery, chemo- and/or radiotherapy, scaffolds would be implanted into patients with aggressive cancer variants, who are at high risk for disease recurrence. Insertion and biopsy of a synthetic niche using a trocar would be comparable with procedures using a CNB. The microporous scaffold supports cell inltration from the host, which becomes vascularized within days [148]. In addition to the broblasts and endothelial cells, the biomaterial scaffold elicits a foreign body response that recruits immune cells from the vasculature. Immune cell inltration is highly dynamic during the acute phase (1-2 weeks after implantation) and is followed by a chronic phase that is rel-

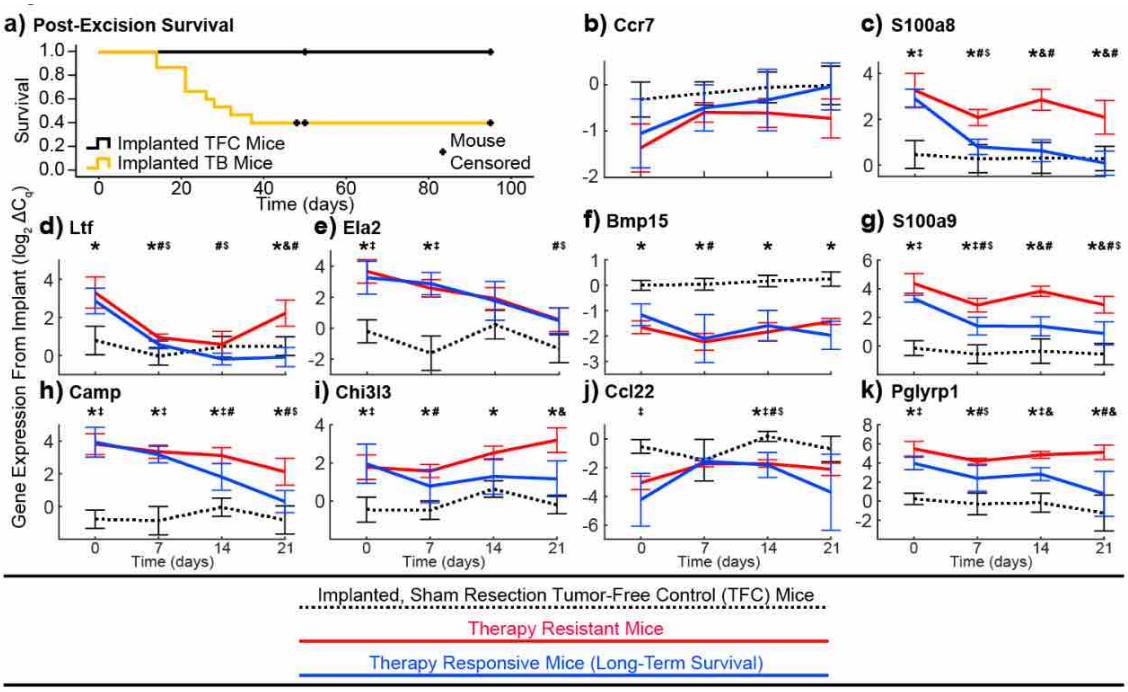

Figure 5.12: **Additional data from post-excision model demonstrating the cohort survival curve and gene expression trajectories.** (A) Kaplan-Meier survival analysis comparing TFC and TB mice that received mammary gland excisions. (B)-(K) Time course analysis for 10 gene panel. Error bars in line plots for gene expression and signature trajectory indicate SEM. The cohort size for each group is decreased by one at Day 21 due recurrence and animal censorship. For longitudinal data, statistics were performed via a linear mixed model. Post hoc simple effects analysis indicates significant differences ($p<0.05$) between ($*$) TFC and resistant, ($‡$) TFC and responsive, (&) resistant and responsive, (#) responsive and responsive Day 0 (pre-excision), and ($) resistant and resistant Day 0 (pre-excision) following significant ($p<0.05$) or trending ($p<0.1$) interactions in a two-way ANOVA.

atively stable. However, as the health status of the host changes, the immune cells and acellular material in the circulation may be altered, which alters recruitment to the scaffold and transforms the immune composition at the synthetic niche from that of a healthy individual to reflect the diseased state. This relationship between the foreign body response and disease state has emerged recently, with observations in the context of diabetes and neoplasia [138, 139]. In the work focused on neoplasia, Oliva and colleagues demonstrated that tissue adhesives perform differently in healthy, inamed, and neoplastic colon tissue, which were then used to inform the synthesis of disease-specic adhesives [138]. Our data builds on these observations by

demonstrating that the immune pathways in tissue localized at biomaterial implants may be exploited as a cancer diagnostic platform.

Changes in the gene expression of tissue biopsied from implants of tumor-bearing mice suggest the adoption of an immunosuppressive and hospitable environment for tumor cells, which is reflective of metastatic niche biology and primary tumor conditioning of distant vital organs. The increases in *S100a8/9* are hallmarks of premetastatic and metastatic niche formation in metastasis-targeted organs (e.g., lungs) and MDSC immunosuppressive functionality [137]. Accordingly, S100a8/9 expression leads to T-cell inhibitory/cytotoxic byproducts (e.g., reactive oxygen species) and tumor cell proliferation [149, 150]. Others have shown that tumor cells, specically 4T1 cells, lack production of *S100a8/9* [151], thus our results reect changes in immune cell dynamics and not the presence of metastatic tumor cells. An interesting discovery was that *S100a8/9* was also upregulated in macrophage and DC populations, supporting that multiple myeloid cell lineages are involved establishing the metastatic niche. Unlike the increase in *S100a8/9*, the increase in *Pglyrp1* has not yet been associated with the metastatic niche, although *Pglyrp1* expression correlation with *S100a8/9* was previously associated with bone marrow-derived granulocytic MDSCs and Th17 to regulatory T (Treg) cell transdifferentiation [152, 153]. Increases in *Ela2*, *Camp*, and *Ltf* had the greatest overall magnitude changes within the implant tissue at day 21. *Ltf* and *Camp* are upregulated in granulocytic MDSCs as compared with neutrophils, and increased levels of *Ela2* and Camp have been identied as drivers of metastasis, with *Ela2* associated with poor clinical outcomes and endocrine treatment failure [142, 154]. *Chi3l3* expression progressively increased in the tissue inltrate, and this finding is supported by recent reports that chitinase-knockout mice had decreased metastasis [155]. A decrease in *Ccr7* would limit the

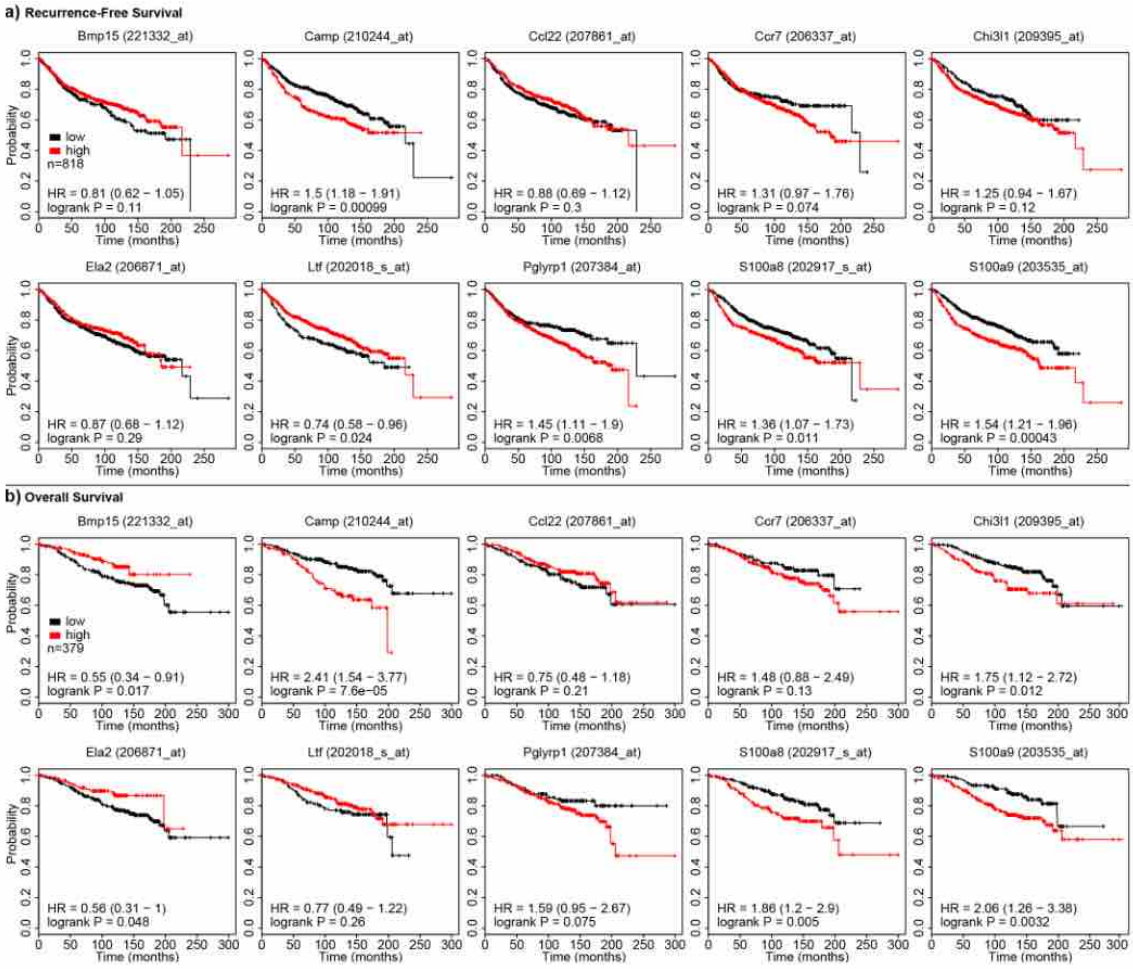

Figure 5.13: **Kaplan-Meier survival curves correlated with high and low gene expression from breast cancer patient samples.** (a) Microarray (GEO via KMPlot) and prognosis data were queried for genes selected for the 10-gene panel derived from tissue within implants to determine the expression level relevance in primary tumors on the clinical outcome of systemically untreated breast cancer patients (n=818). Kaplan-Meier plots indicate as separation of two profiles separating high and low gene expression that are automatically divided by the median expression of the genes for all samples. Plots indicate the Hazard Ratio (HR) which is highest for S100a9 and logrank significance comparing high and low expression as a function of recurrence-free survival. FDR 10% corrected significance ($p<0.011$) and FDR 5% corrected significance ($p<0.00099$). (b) Metrics on overall survival (n=379 patients) were calculated in the same manner as that for recurrence-free survival. FDR 10% corrected significance ($p<0.0123$) and FDR 5% corrected significance ($p<0.005$)

chemoattraction of T cells, reecting the decrease in $CD8^+$ and $CD4^+$ T cells in tissue at days 14 and 21, respectively [22, 156]. *Ccl22* expression can be upregulated in metastatic target organs and attracts Tregs in oncogenesis, thus the decrease in *Ccl22* expression during disease progression was novel and not anticipated [157]. Data accessed from a gene expression repository suggests that expression of *S100a8*, *S100a9*, *Pglyrp1*, and Camp in the primary tumors of patients with breast cancer is prognostic, which points toward some conserved biological mechanisms (Fig. 5.13A and B), yet these primary tumor measurements are limited to a single predictive measure and do not facilitate the monitoring of oncogenic changes over time. Collectively, data obtained from implants in the BALB/c-4T1 metastatic model indicate that the scaffold is conditioned by the primary tumor, leading to increased expression of genes associated with an immunosuppressive microenvironment.

Analysis of the scaffold provides data relevant to the elusive metastatic niche that is distinct from the information that obtained from a liquid biopsy. Information obtained from the metastatic niche could be used to generate tools that enable comprehensive analysis of the metastatic cascade to permit early detection. Primary tumor and sentinel lymph node data are attainable from tissue biopsies but are limited to providing only early stage disease findings. Liquid biopsies have utility, yet may reflect an intermediate or potentially clinically noncontributory step in the disease process. Cell migratory events, particularly events involving immune cells leaving the vascular and entering distal tissues, are associated with phenotypic changes. As the formation of the metastatic niche is stochastic in distal organs, the ability to predetermine the location of the metastatic niche enables the analysis of the microenvironments that support the survival of disseminated tumor cells. Importantly, for the 4T1 metastatic breast cancer model, this data showed that the conditioning

of the implant microenvironment was similar to the conditioning of the lung. Interestingly, the gene panel had several common responses in two distinct models of breast cancer metastasis to the lung. Thus, these findings point toward the development of an environment that can induce a common lung-tropic cellular phenotype in recruited cancer cells [158]. We do not anticipate that this implant replicates the biology of the lung, yet is capturing common aspects of metastatic conditioning. These results highlight the spectrum of immune states that sites distal from a primary tumor exhibit following therapy and during cancer progression. Through the targeting of early immunologic events using immune modulatory agents, these dynamics could potentially be exploited [159]. In addition, these treatments could be used in conjunction with anticancer therapies that focus on the cellular weaknesses gleaned from the analysis of tumor cells captured within the scaffold. The expectation that combinatorial approaches would be necessary to address different cancer subtypes will help to realize the promise of personalized medicine.

Analysis of the scaffold following surgical excision of the primary tumor allowed for monitoring of response to this therapy, and stratified the tumor-bearing treatment group based on survival outcomes. Predictive scores were derived from gene expression signatures to track disease status and enable longitudinal monitoring of individual mice before and after surgical treatment. One of the most interesting observations was the sharp regression in tumor-promoting gene expression in the implants following cancer excision of the tumor-bearing mammary fat pad. On the basis of scRNA-seq data, this rapid change in gene expression likely results from changing immune cell populations or altered phenotypes within the implant. This dynamic nature of immune cells at the implant underpins the concept of the synthetic niche, which could inform the initiation of novel therapeutic interventions. In the last

year, novel therapies have become available for the treatment of hormone insensitive and HER2 receptornegative breast cancer. Olaparib, a PARP inhibitor, has shown efficacy in extending progression-free survival for patients with metastatic, BRCA mutationpositive, and triple-negative breast cancer [160]. In addition, an anti-PD-L1 antibody, atezolizumab, was also recently found to be efficacious in extending survival for patients with PD-L1expressing metastatic triple-negative breast cancer [161]. Accelerating the initiation time of these promising treatments, through early-detection diagnostic platforms, could improve disease-specic outcomes by allowing therapeutics to function when the burden of metastatic disease and heterogeneity of cancer mutations are relatively low. Furthermore, the niche can be analyzed for the presence of immunosuppressive macrophages and DCs, which presents unique diagnostic avenues and therapeutic targets for tumors that are driven by these myeloid subsets and complements efforts to characterize and overcome MDSC immunosuppression.

The application of tissue engineering for cancer diagnostics represents a novel approach to engineer a system that reports on early metastatic sites. Our data indicate the ability to capture disease progression or regression, suggesting that the foreign body response has the potential to capture both immune activation and suppression, which may enable their application to a range of immunologic disorders. Collectively, our data indicate that the tissue within implants is dynamic, with a context-dependent prole that reects disease course and response to tumor excision. Broadly, the concept of synthesizing tissues that are difcult to assess, such as the lung or central nervous system tissue, may enable diagnostics that have broad application for monitoring immunologic diseases.

5.6 Materials and Methods

5.6.1 Microporous PCL scaffold fabrication

Poly(ϵ-Caprolactone) (PCL) microspheres were prepared by emulsifying (homogenization at 10,000 rpm for 1 minute) a 6% (w/w) solution of PCL (Lactel Absorbable Polymers) in dichloromethane in a 10% poly(vinyl alcohol) solution, which was then stirred in DI water for 3 hours. Particles were collected by centrifugation, serially washed with MilliQ filtered water, then lyophilized. Salt porogen (NaCl) with a size range of 250-425 m was selected through sieving. PCL microspheres and NaCl were then mixed in a 1:30 (w/w) ratio and pressed at 1,500 psi in a stainless-steel die (International Crystal Laboratories) for 45 seconds. The volume and die size used results in a PCL/NaCl disc that is 5 mm wide and 2 mm thick (Fig. 5.2A). PCL/NaCl discs were heated on disinfected glass slides to 135°C for 5 minutes per side. NaCl was then removed via leaching in MilliQ water for 1.5 hours. The resulting microporous PCL scaffolds were disinfected in 70% ethanol then serially rinsed in sterile filtered MilliQ water. Scaffolds were dried on a sterile gauze and stored at -80°C until time of implantation.

5.6.2 Animals and scaffold implantation

Microporous PCL scaffolds were implanted in the subcutaneous space of female mice to facilitate cellular infiltration and development of a foreign body response for subsequent isolation and analysis. All animal studies were performed in accordance with institutional guidelines and protocols approved by the University of Michigan Institutional Animal Care and Use Committee. Female mice of the BALB/c and C57BL/6 strains were purchased from Jackson Laboratories at an age of 8 weeks.

For implantation, mice were administered the analgesic Carprofen (5mg/kg) prior to and 24 hours after surgery. Mice were anesthetized under isoflurane (2.0-2.5%) and assessed by toe pinch reflex for level of sedation. The upper dorsal area above the scapula was then shaved and prepared using betadine and ethanol swabs. An incision (approximate 7-10 mm from anterior to posterior) was made in the upper dorsal area. A subcutaneous cutdown created a pocket in the lateral direction on the left and right sides of the mouse. A single scaffold was then inserted into each pocket. Two scaffolds were implanted for mice used to identify the initial gene expression changes and develop a signature. The incision line in these mice was closed with 7 mm stainless-steel wound clips (Roboz Surgical Instrument Co.). An array of eight scaffolds was implanted in mice used for longitudinal monitoring of disease course after therapy. Skin in these mice was closed with suture (MONOCRYL-poliglecaprone 25, Ethicon, Inc.).

5.6.3 Metastatic tumor cell lines and animal inoculation

Orthotopic inoculation of tumor cells was performed 2 weeks after scaffold implantation. 4T1-luc2-tdTomato cells were obtained from Perkin Elmer which had been authenticated previously via short tandem repeat (STR) and comparison with ATCC STR database. E0771 GFP^+ cells were a kind gift from the Laboratory of Gary and Kathryn Luker at the University of Michigan Center for Molecular Imaging. To develop a more aggressive metastatic cell line, we employed a serial inoculation strategy that began when a C57BL/6 mouse inoculated with the parental line exhibited secondary metastatic growths at many sites including: lung, brain, mesentery, and diaphragm. Cells derived from the original lung (Lu.1) and brain (Br.1) metastases were then inoculated via intracardiac injection, which resulted in

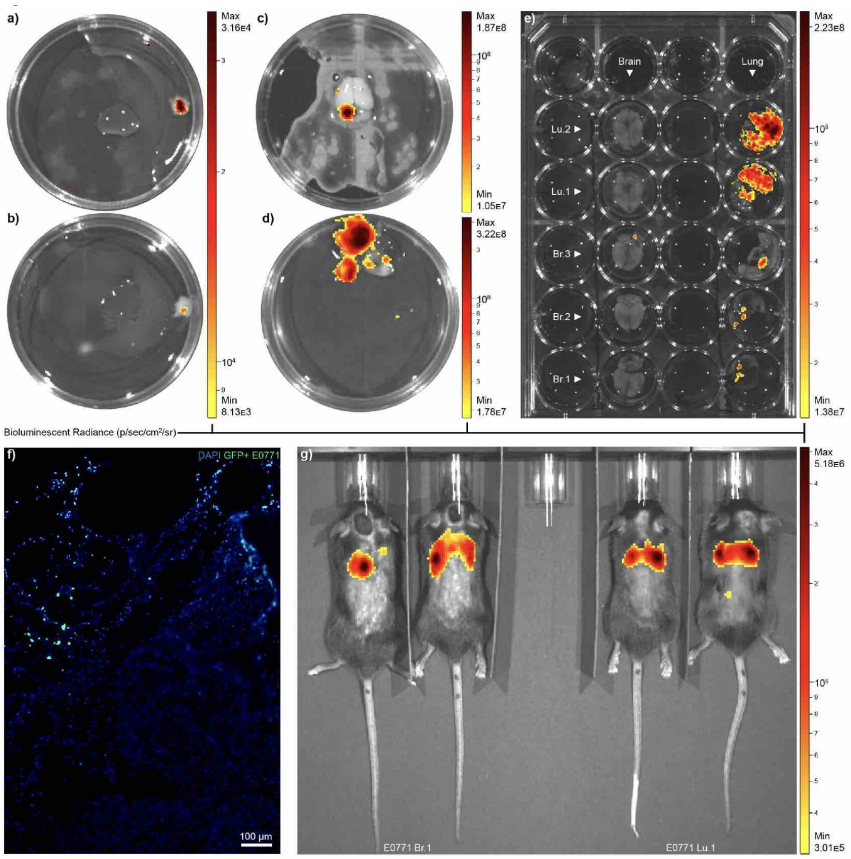

Figure 5.14: **Scaffolds from (A) left and (B) right side of a mouse inoculated with parental E0771 which developed a high metastatic burden which metastases present in the (C) brain and (D) lungs.** Metastatic lines Br.1 and Lu.1 were derived from the tumor cells from these brain and lung metastases, respectively. Serial inoculation via intracardiac injection and isolation of developed metastases (E) indicated a propensity for the lung derived metastases have an organotropic bias toward lung tissue. (F) Confirmation of fluorescent tumor cells in the scaffolds from (A)-(B) was verified by fluorescent microscopy of scaffold tissue sections. (G) *In vivo* imaging of Br.1 and Lu.1 line 11 days following intracardiac inoculation.

brain and lung metastases that were again isolated as Lu.2 and Br.2. Both Lu.1 and Lu.2 showed a stronger inclination for metastatic colonization of the lung (Fig. 5.5E), similar to reports on 4T1 phenotype. 4T1-luc2-tdTomato (BALB/c) or E0771 Lu.2 (C57BL/6) syngeneic tumor cells were orthotopically inoculated at a density of 40,000 cells/μL for a total of 800,000 in 20 μL of sterile Dulbeccos phosphate buffer saline (DPBS; Gibco). Inoculation was performed by making a small incision (5 mm dorsal to ventral) above the 4th right mammary fat pad. The mammary fat pad was

exposed, injected, then the skin was closed with tissue adhesive (3M Vetbond^{TM}). Tumor measurements were taken daily, starting at Day 7, and calculated with the conventional ellipsoid equation (width^2*length)/2.

5.6.4 Biopsies tissue of scaffold, blood, and lung tissue

Biopsies of tissue from microporous scaffolds, leukocytes from blood, and lung tissue were isolated to study gene expression changes due to disease progression. Microporous scaffolds that had been implanted for either 7, 14, or 21 days following inoculation of primary tumors (as indicated in figures) were surgically biopsied following isoflurane (2.0-2.5%) sedation by making an incision adjacent to the implant site and removing the implant without taking surrounding tissue. Using this surgical biopsy ensure we sampled the implant and eliminated caveats associated with biopsies of regenerated tissue in the implant, yet this aspect would need to be analyzed for translation. For core-needle biopsy (CNB) of the implant, a disposable CNB tool (Bard® Mission® Disposable Core Biopsy Instrument) was inserted through the skin and used to isolate a portion of the implant and infiltrating tissue (Fig. 5.15B), which enables minimally invasive retrieval of samples. Leukocytes were isolated from blood via an intracardiac blood draw stabilized by EDTA. Erythrocyte lysis in EDTA-treated blood samples was performed with Ammonium-Chloride-Potassium (ACK) Lysing Buffer (Gibco) with serial washes in DPBS. Lung tissue from time-matched healthy control and tumor-bearing mice at Day 21 were isolated for endpoint comparative analysis following euthanasia.

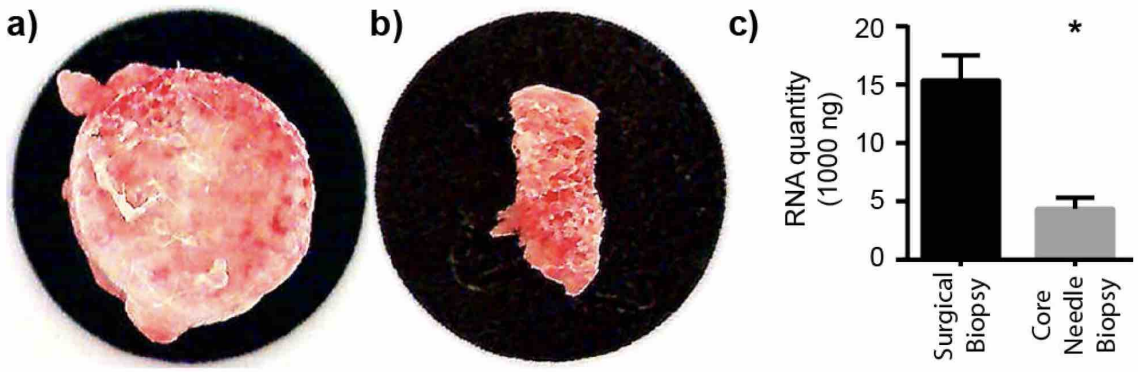

Figure 5.15: **Implant microenvironment exhibits good tissue ingrowth and facilitates surgical and core-needle biopsies to acquire RNA for transcriptomic or gene expression analysis.** (A) A surgically-biopsied implant illustrating the intact, frozen condition prior to RNA isolation and RT-qPCR assessment. (B) A sample derived from a scaffold using a core needle biopsy (CNB, Bard® Mission® Disposable Core Biopsy Instrument) which enables minimally invasive retrieval of samples, similar to clinical approaches for sampling suspicious tissue. In both samples tissue ingrowth into the microporous structure is evident but especially in the CNB as the cutting plane transected the inner core of the implant. Scaffolds as shown are in -80^{c}ircC frozen state. Diameter of the black background circle is 7.5 mm. (C) Comparing the RNA isolated from the full surgically biopsied scaffold compared to the CNB sample, there is a significant -1.812 log-transformed fold change, but sufficient material for numerous gene expression assessments (RT-qPCR, RNAseq, etc.) with the CNB samples containing an average of 4376 ng of total RNA. indicates differences between surgically biopsied and CNB samples from an unpaired t-test ($p<0.05$, n=8).

5.6.5 Surgical resection of primary tumor and longitudinal tracking

To test the responsiveness of the tissue biopsied from implants to therapeutic treatment mammary gland removal was performed on the 4T1 primary tumor that had been inoculated in the 4th right mammary fat pad of BALB/c mice. In this model, the primary tumor was resected 14 days after inoculation, which aligns with the time point for the initial set of experiments to study the progressive changes in the tissue within implants as a function of disease course. The skin above the primary tumor was prepared by swabbing with betadine and ethanol. A dermal incision was made adjacent to the primary tumor for the length of the primary tumor and mammary fat pad (approximately 1 cm). Large vessels surrounding the primary tumor were cauterized using a Gemini Cautery System (Roboz Surgical Instrument Co.).

Iris scissors were used to cut connective tissue to separate the mammary fat pad and contained primary tumor from the superficial dermal and underlying body cavity wall. The dermal incision was closed using suture (MONOCRYL-poliglecaprone 25, Ethicon, Inc.). Following tumor resection and mammary gland removal, animal health was monitored daily for activity and responsiveness, including posture, mobility, body weight, grooming behavior, and respiratory conditions. Animals were euthanized if found in a moribund condition or when a primary tumor regrowth was positively identified.

5.6.6 RNA isolation, purity, integrity, and cDNA synthesis

Total RNA was isolated from tissue biopsied from implants, lung tissue, and leukocytes from blood. Frozen (-80°C), surgically biopsied scaffolds were immersed in monophasic solution of phenol and guanidine isothiocyanate (TRIzol® reagent, Thermo Fisher Scientific, Waltham, MA) at 4 °C, then homogenized with a rotor stator homogenizer (T25, S25N8GST dispersing element, IKA® Works, Inc.). Samples were then centrifuged at 10,000g to remove particulate, and the TRIzol® containing genomic content from the scaffold was then processed in a silica-based matrix spin column (Direct-zol™ RNA Miniprep Plus, Zymo Research Corp., 110 Irvine, CA) with DNase I treatment to isolate total RNA. Concentration (modified Beer-Lambert at 260nm) and purity (260nm/280nm absorbance ratio) of the RNA isolation was assessed by light absorbance via a NanoDrop 2000c (Thermo Fisher Scientific). Additionally, RNA integrity number (RIN) analysis was obtained through RNA fragment analysis (RNA 6000 Nano Kit on a 2100 Bioanalyzer, Agilent Technologies, Inc., Santa Clara, CA). RIN for samples used in high-throughput RT-qPCR ranged from 8.2-9.7. Generation of first strand cDNA was performed through reverse transcrip-

tion (RT, SuperScript™ VILO™ cDNA Synthesis Kit, ThermoFisher Scientific). For all RT-qPCR of tissue biopsied from implants, RT was performed with an RNA concentration of 200 ng/μL. cDNA was either used immediately for RT-qPCR or stored at -80°C. Frozen lung tissue biopsy RNA was isolated in similar fashion to implants with RT performed at an RNA concentration of 200 ng/μL. Blood leukocyte RNA was isolated by thoroughly mixing blood leukocytes following ACK lysis in TRIzol, then processing for RNA and performing RT at 100 ng/μL due to limited quantities of total RNA. RNA concentration was increased to 200 ng/μL (niches and lungs) or 100 ng/μL (blood) using a RNA clean-up kit (RNA Clean & Concentrator-5, Zymo Research Corp.) for samples below these thresholds.

5.6.7 OpenArray™high-throughput RT-qPCR

Tissue biopsied from implants was analyzed for gene expression with OpenArray® (OA), a high-throughput RT-qPCR platform that analyzes 648 genes per sample in parallel, in accordance with the standard OA protocol. All materials used in this section were purchased from Thermo Fisher Scientific. Briefly, the genes for this study were focused on the immune pathways and included a panel of 16 reference (housekeeping) genes per sample (Applied Biosystems™ TaqMan™ OA Mouse Inflammation Panel, Cat. No. 4475393). cDNA from tissue biopsied from implants in tumor-free healthy controls (n=14 total tumor-free control) and tumor-bearing mice (n=14 total tumor-bearing) across the three time points of 7 (n=3), 14 (n=8), and 21 (n=3) days were mixed with 2X TaqMan® OA Real-Time Master Mix then loaded onto the OA panels via a robotic OA AccuFill™ System in an order that staggered conditions and time points across the panels analyzed. The OA RT-qPCR

run (QuantStudio 12K Flex Real-Time PCR System, ThermoFisher Scientific) and sample quality control were performed by the Affymetrix Group at the University of Michigan DNA Sequencing Core. In accordance with OA standard operating procedure, C_q was calculated as C_rt, a curve-specific method.

5.6.8 Analysis of gene expression and selection of genes of interest

Gene expressions from OA was screened to identify genes of interest during disease course. First, genes with insufficient data within samples (missing greater than 4/14 per cohort or 2/3 per time-point) were dropped from the study, resulting in 559 genes for full analysis. Next the 16 reference genes were ranked according to their expression stability compared to each other and as a function of experimental design (NormFinder Algorithm), which led to the selection of *Gapdh*, *Tbp*, *Ywhaz*, *Hmbs*, and *Ubc*. ΔC_q values were calculated against the average of the reference genes, centered on median of time-matched tumor-free controls, then standardized for cluster and multivariate statistical analysis. From ΔC_q data fold change, significance (uncorrected p and false-discovery rate corrected q), at Days 7, 14, and 21 were calculated. For computational analysis ΔC_q values are log2 transformed and centered on the healthy, tumor-free control time-matched median as reflected in the figure box plots, which show the median, 25th-75th percentiles and most extreme data points not considered outliers (outliers are visually indicated by +). Management of non-detects within the OA data was handled in two manners: for multivariate statistical analysis non-detects were interpolated based on the ΔC_q average across all cohorts and time points, and for signature construction non-detects were interpolated based on the ΔC_q average for a specific cohort at a specific time point.

5.6.9 10-gene panel RT-qPCR analysis in 96-well format

Experiments for signature validation, analysis of blood, lung and post-excision monitoring was performed by RT-qPCR analysis in 384-well and 96-well plate formats using matched Taqman® probes from the OA platform (see Supplementary Data 1 for probe details). Like the OA RT-qPCR, samples were staged within plates alternating between tumor-free control and tumor-bearing. The same 5 reference genes (*Gapdh*, *Tbp*, *Ywhaz*, *Hmbs*, *Ubc*) were run in parallel with the 10 target genes of interest (*Bmp15*, *Camp*, *Ccl22*, *Ccr7*, *Chi3l3*, *Ela2*, *Ltf*, *Pglyrp1*, *S100a8*, *S100a9*) for all studies in BALB/c mice. *Ywhaz* and *Ubc* were only used for the C57BL/6-E0771 analysis due to poor detection and poor stability in *Gapdh*, *Tbp*, and *Hmbs* reference genes. Analysis was performed on a CFX Connect™ Real-Time PCR Detection System (Bio-Rad Laboratories, Inc., Hercules, CA) with CFX Manager Software that calculated the C_q values based on the regression analysis mode, which applies a multivariable, nonlinear regression model to each well trace. For signature computation and multivariate statistics, non-detects were interpolated based on Cq average across all cohorts and time points to limit predictive bias, which could be exaggerated by use of a static, arbitrary ΔC_q. Non-detects were left blank for univariate, multiple comparison, and linear mixed model analysis. The gene expression dynamics of tissue biopsied from implants and blood gene expression dynamics were compared by goodness of fit using a normalized root mean square error cost function on a linear polynomial curve fit between Days 7, 14, and 21. Cohort centering was used to align the longitudinal data from the therapy study for subsequent signature analysis. The median of the therapy cohorts Day 0 pre-excision was centered on the OA Day 14 data median, which was experimentally equivalent. The calibration factor used for aligning therapy cohorts Day 0 to OA Day 7 was applied to all successive

time points.

5.6.10 Single-cell RNA-seq of immune cells in tissue biopsied from implants

Scaffolds were implanted in BALB/c mice 14 days before the mice were inoculated with 4T1 metastatic triple negative breast cancer cells in the fourth right mammary fat pad. After an additional 14 days, the scaffolds were removed and digested in order to obtain a single-cell suspension. Erythroblasts were lysed through sequential exposure to 0.2% NaCl and 1.6% NaCl. The cells were prepared for single-cell sequencing using Drop-Seq.

mRNA was collected from each cell and subsequently converted to cDNA before being taken through tagmentation and PCR. Sample quality and DNA concentration were assessed with a Bioanalyzer 2100 before submission to the DNA Sequencing Core at the University of Michigan. Samples were pooled and sequenced on the Illumina HiSeq-4000. The final reads were mapped to the mm10 mouse reference genome to quantify gene expression and a read-count matrix was assembled. Single-cell gene expression was conducted using Seurat, an 180 open source program in R developed by the Satija lab at the New York Genome Center. The matrix was filtered, normalized and scaled before using PCA and tSNE to identify clusters. Identification of each cluster was conducted using known cell markers.

5.6.11 Adoptive transfer and implant trafficking analysis of Ly6G$^+$ and Gr-1$^+$ Ly6G$^-$immune populations

Splenocytes were isolated from 4T1 tumor-bearing BALB/c mice. G-MDSCs (Ly6G$^+$) and M-MDSCs (Gr1$^+$ Ly6G-) were taken from splenocytes by magnetic

bead separation using the Myeloid-Derived Suppressor Cell Isolation Kit (Miltenyi Biotec). G-MDSCs and M-MDSCs were labeled with lipophilic membrane dyes DiD and DiO (ThermoFisher), respectively. Cell staining was performed at a concentration of 2E6 cells/mL in 5μM dye solution at 37°C for 20 minutes. Cells were quantified after staining, and 5E6 live labeled G-MDSCs and 5E6 live labeled M-MDSCs were injected i.v. into disease-free or Day 7 tumor-bearing recipient mice. Recipient BALB/c mice had been implanted with scaffolds 21 days prior to adoptive transfer of labeled cells. Scaffolds were isolated 36 hours after adoptive transfer, and labeled G-MDSCs and M-MDSCs in the scaffold were quantified by flow cytometry.

5.6.12 Gene expression dimensionality reduction and classification

Genes of interest were identified based on fold-change, level of significance, and expression stability over time. Expression stability was defined as a continuous trajectory for the expression of a gene. Panel selection was confirmed by an Elastic Net regularization, which identified how predictive a gene was of the tumor-bearing state, irrespective of timepoint. Elastic Net regularization, a variation of the LASSO (least absolute shrinkage and selection operator) algorithm with an α=0.1 and leave-one-out cross validation, was employed using the Matlab lasso function on the ΔC_q of the 559 genes with sufficient data. This data indicated the predictive nature of genes for tumor-bearing classification at specific time points (Fig. 5.15B). Clustering of samples was performed with the Matlab clustergram function on standardized ΔC_q data. Dendrograms indicate clustered genes and samples, in which samples are indicated on the x-axis and genes expressed are indicated on the y-axis with a complete linkage and a display range of -3.5 to +3.5. Unsupervised dimensionality reduction was performed using singular value decomposition (X=USVT) with the Matlab svds

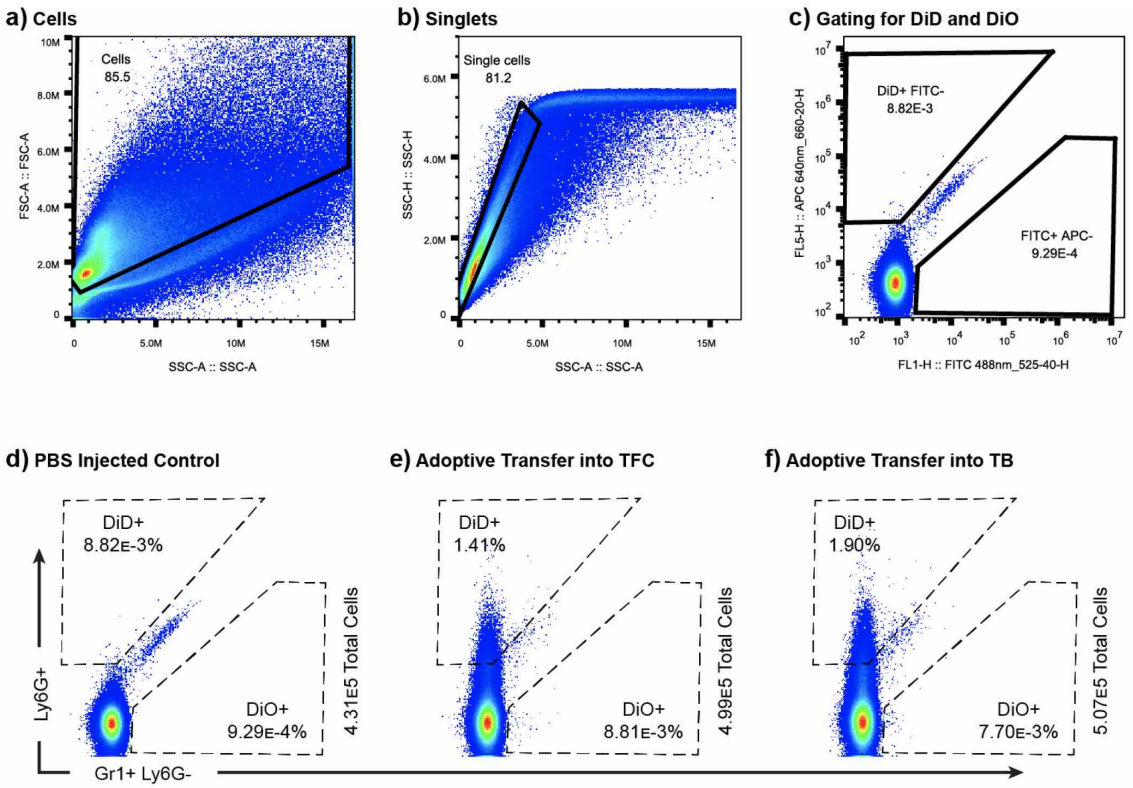

Figure 5.16: **Gating scheme for flow cytometry analysis of adoptive transferred cells.** These plots indicate the (A) cells and (B) singlet gating prior to (C) gating for DiO and DiD fluorescent lipophilic dyes. Axes in(c) are identical to those in panels (D)-(F). Numbers on plots indicate percentage of gated cells in comparison to (A) total events, (B) gated cells, and (C) single cells. Representative flow cytometry plots and gating for (D) PBS injected control mice and adoptively transferred $Ly6G^{+}$ and $Gr1^{+}Ly6G^{-}$populations into (E) TFC and (F) TB mice.

function on the 10-gene and 4-gene panels standardized ΔC_q values centered on the time-matched tumor-free controls. The first 3 principle components (PCs) were computed from the first 3 left singular vectors (columns of U, eigenassays) and singular values (diagonal matrix S). Unsupervised separation of the samples was visualized by plotting the PCs in 3D scatter, which was quantified by calculating the Euclidean distance in PC1 and PC3 to each sample from the centroid of all the tumor-free controls. Distance calculations were scaled between 0 and 1. A supervised machine learning algorithm, bootstrap aggregated (bagged) decision tree ensemble (i.e., Random Forest^{TM}), was used to construct a predictive model based on the 10-gene and

4-gene panels standardized ΔC_q values centered on the time-matched tumor-free controls. The model was constructed using the Matlab core fitcensemble function with the Bag method. Decision tree depth was limited by the number of splits to 1.5 times the number of input predictors (genes). The number of learning cycles for final model was set to 250 cycles. A partitioned model and leave-one-out cross-validation was performed using the Matlab crossval and kfoldPredict functions, which returned the posterior probability for classification of each sample.

5.6.13 Statistics

This section details the statistical tests used to evaluate the hypotheses. Error bars are defined within figure legends, with all line plots indicating standard error of the mean. The exact n for each test is detailed in the legends along with the methods for multiple comparisons corrections. All n throughout the manuscript indicate biological replicates from different mice. During the initial screen of the OA data and selection of genes of interest, a false-discovery rate corrected two-tailed t-test using a linear step-up procedure to account for all genes analyzed (559 total following elimination of genes that did not contain sufficient sample) contrasted samples from tumor-bearing mice and healthy time-matched tumor-free controls. These tests were carried out in Matlab using the mattest and mafdr functions. All statistical indicators within the manuscript were computed using packages and syntax in the Statistical Package for the Social Sciences (SPSS, International Business Machines Co., Armonk, NY). Multiple comparisons analysis for comparisons with an individual time point were compared via an independent Students two-tailed t-test with Dunn-*Šidák* correction for multiple comparisons resulting in a $p<0.0051$ being considered significant. Two-way multivariate analysis of variance (MANOVA) for genes

of interest and reduced dependent variables (SVD score or bagged tree prediction) were performed within the generalized linear model (GLM) syntax package using the BY command for condition and time. First, Pillais Trace statistic ($p<0.05$) was used to determine MANOVA significant interaction effects. Second, fixed-effects ANOVA was used to assess univariate interaction effects. Last, following determination of multivariate and univariate interaction effects, a post-hoc simple effects analysis was computed with *Šidák* correction from an initial $p<0.05$ for multiple comparisons to determine within groups over time and between groups at Days 7, 14, and 21. To analyze the differences within mice tracked longitudinally before and after a therapeutic tumor excision a Linear Mixed Model (LMM) was employed. The SPSS syntax for the LMM is available in the prepress repository. First, two-way ANOVA within the LMM was assessed for significant ($p<0.05$) or trending ($p<0.1$) interactions. Last, post hoc simple effects analysis indicated significant differences ($p<0.05$) within groups over time and between groups at Days 7, 14, and 21. Within the figures the focus for within group effects was how the gene expression, SVD, or bagged tree data changed from pre-excision (Day 0) to post-excision (Days 7, 14, and 21).

5.6.14 Breast cancer patient microarray Kaplan-Meier correlation

A repository of human patient microarray data was analyzed for gene expressions correlations with high or low gene expression and patient recurrence free survival (RFS). Microarray data from Gene Expression Omnibus (GEO) via Kaplan-Meier Plotter (KMPlot, kmplot.com/analysis/) and prognosis data were queried for the 10-gene panel from the implant-derived data to determine the expression level relevance in primary tumors on the clinical outcome of systemically untreated breast cancer patients. Separation of high and low gene expression profiles was automat-

ically divided by the median expression of the genes for all samples – n = 818 for recurrence-free survival and n = 379 for overall survival. Redundant and outlier microarrays were excluded, and only breast cancer patients that were systemically untreated were included. Data outputs for Hazard Ratio (HR) and logrank significance are indicated in plots with multiple comparisons corrected using the KMPlotter tool for false-discovery rate (FDR) with FDR 10% corrected significance FDR 5% corrected significance.

5.6.15 Protocol and material availability

Many of the experimental protocols including scaffold fabrication, RNA isolation, and RT-qPCR follow previously published or manufacturer recommended guidelines and additional specifics are available from authors. The lung-topic Lu.2 cell line derived from the parental E0771 tumor cell line is available from the authors.

5.6.16 Data availability

OpenArray^{TM} raw C_q, ΔC_q, and $\Delta\Delta C_q$ data is prepared for deposition in the National Center for Biotechnology Information (NCBI) Gene Expression Omnibus (GEO). OA .eds files are available from authors upon request if access to quality controls (e.g., C_q confidence), amplification plots and C_q indicators are desired. All other data supporting the findings in this study are available within the paper and the supplementary data files. Single cell RNA-seq metadata, raw data, and processed data will be deposited in the ArrayExpress according to the Annotare sequencing template for single-cell submission. This includes cell-gene count matrix, cluster identifications, markers for identification, and the compressed raw sequence read

files in the fastq.gz format. ArrayExpress and GEO repositories comply with MINSEQE and MIAME, respectively.

5.6.17 Code availability

Code that used built-in Matlab packages is available in the supplementary data files alongside the raw data. The Matlab code and data output is available as the .m file but has been converted to an html with table of contents to simplify review of computational steps. SPSS syntax used for statistical analysis is available alongside the statistical outputs with full descriptive statistics and indications of significance or trends. The data output is organized by sheet to reflect each statistical analysis for the OA gene expression MANOVA, OA signature MANOVA, C57BL/6-Lu.2 model multiple comparisons t-tests, LMM output for excision 10/4-gene signatures and gene expression data, blood MANOVA, and lung multiple comparisons. The .xlsx output is in the supplementary data files alongside the raw data and code.

CHAPTER VI

The Role of Gr-1$^+$ Cells at Metastatic Sites Changes with Disease Progression

6.1 Authors

Yining Zhang, Jing Wang, Sophia M. Orbach, Ravi M. Raghani, Jacqueline S. Jeruss, Lonnie D. Shea

6.2 Abstract

Myeloid-derived suppressor cells (MDSCs) have been shown to contribute to the lack of response for a number of immunotherapies for cancer. As such, they present potential as diagnostics and therapeutic targets. The phenotype of MDSCs has been well-characterized *in vitro* and within various tissues, though relatively little is known about their dynamics and behavior specifically at metastatic sites. Herein, we used polymer scaffolds to investigate the phenotypic changes that Gr-1$^+$ cells undergo throughout metastatic disease progression. Porous polymer scaffolds implanted into tumor-bearing mice recruit immune cells and subsequently metastatic tumor cells, forming a microenvironment that has been shown to reflect the disease state of the animal. These scaffolds provide a pre-defined location for metastatic events, which can be used to isolate Gr-1$^+$ cells for further study. We observed that the phenotype

of Gr-1$^+$ cells across different tissues change with disease progression, and found that the changes observed at the scaffold are more similar to the metastatic lung than to the spleen.

6.3 Introduction

Recent advances in the understanding of immune-tumor cell interactions has led to the development of immunotherapies such as immune checkpoint blockade, CAR T cells, and cancer vaccines. The efficacy of these therapies rely on their ability to induce or improve the CD8$^+$ T cell capacity for killing of tumor cells. However, it has been shown that the presence of pro-tumor innate immune cells suppresses T cell function, limiting the efficacy of these the therapies. Myeloid-derived suppressor cells (MDSCs), in particular, have been identified as a major contributor to the observed immunosuppression. MDSCs are a heterogeneous population of immature innate cells. In mice, they are identified by their surface markers CD11b and Gr-1 (Ly6C/Ly6G).

The role of Gr-1 cells has been extensively studied in the past decade, especially in the context of developing methods of counteracting their immunosuppression [4, 5, 7, 13]. Several studies have reported the different roles of distinct MDSC populations in aiding metastatic seeding, niche maintenance, and primary tumor growth [4], as well as the tissue-dependence of MDSC phenotype [5].

We hypothesized that Gr-1$^+$ cells at metastatic sites are also functionally distinct from those within the spleen, and that the phenotypes of Gr-1$^+$ cells change with disease progression across different tissues. Due to the challenges of studying Gr-1$^+$ cells *in situ* and longitudinally, the changes in Gr-1$^+$ cell phenotype over time

remains largely unexplored.

Polymer scaffolds that recruit immune and tumor cells *in vivo* have been used to study metastatic cells [20, 21, 22, 134], and the microenvironment at the scaffold has been shown to reflect the disease state of the animal [159]. These scaffolds recapitulate many aspects of metastatic sites, and are thus likely to recruit Gr-1$^+$ cells that are functionally similar to those at metastatic sites.

In this study, we investigate whether the MDSCs responsible for early metastatic events are phenotypically distinct from those that persist at later timepoints, and utilize the scaffold to further investigate Gr-1$^+$ cells at metastatic sites. Anti-Gr-1 antibody (RB6-8C5), which depletes Gr-1$^+$ cells, has been utilized to assess the functional contribution of Gr-1$^+$ cells in cancer, and has been explored as a therapy [162]. Here, we also use antibody depletion at various timepoints throughout disease progression to investigate the disease state-dependence of Gr-1$^+$ cells phenotype.

6.4 Results

6.4.1 Tissue-specific and time-dependent functional phenotype of Gr-1$^+$ cells

We first investigated the phenotypes of tumor-induced Gr-1$^+$ cells within various tissues and disease states *in vitro*. We assessed the tissue-specific differences of Gr-1$^+$ cells isolated from different organs with a trans-endothelial tumor cell migration assay. Conditioned media was collected from Gr-1$^+$ cells of the spleen, lung, and scaffold of tumor-bearing mice, and tumor cell migration across an endothelial cell layer toward the conditioned media was studied. Conditioned media generated from Gr-1$^+$ cells isolated from the lung and the scaffold induced migration of tumor cells, whereas those from the spleen and tumor free control did not (Fig. 6.1), indicating

differential secretion of chemoattractants and/or other factors that are able to directly influence tumor cells.

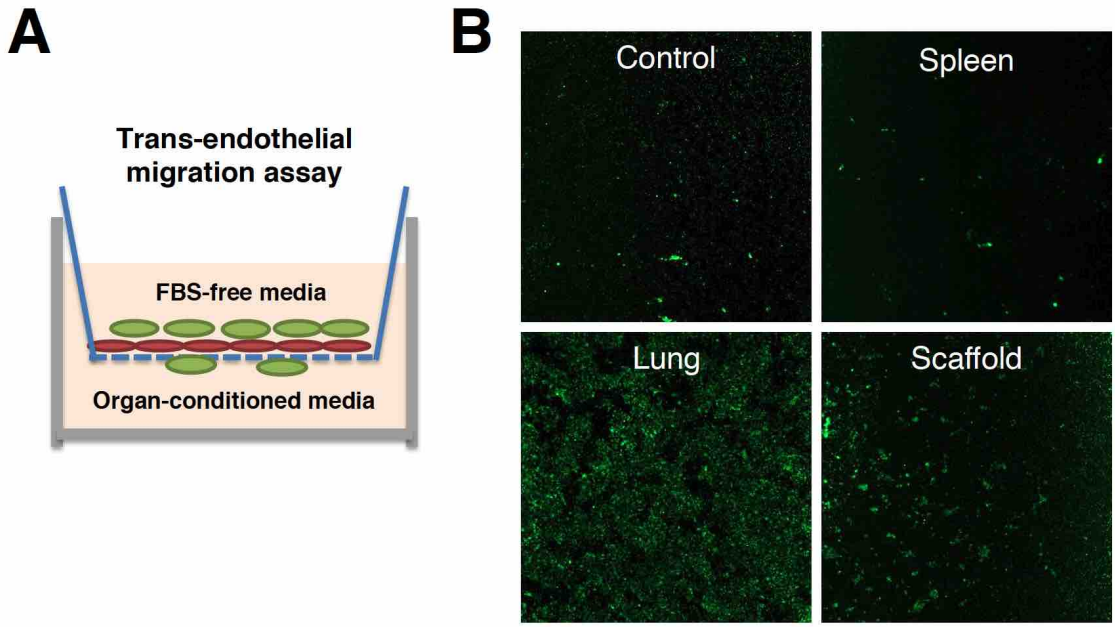

Figure 6.1: **Gr-1$^+$ cell secreted factors induce transendothelial migration.** A) Transendothelial migration assay design. B) Microscopy images of tumor cells (green) that have migrated across the endothelial transwell cell layer toward conditioned media isolated from Gr-1$^+$ cells within spleen, lung, and scaffolds of tumor-bearing mice.

Changes in Gr-1$^+$ cell phenotype and their interactions with anti-tumor immune cells as functions of disease state were also investigated. The ability of these cells to inhibit T cell proliferation was assessed with a T cell suppression assay. Gr-1$^+$ cells isolated from organs at day 3 (pre-metastatic) or day 10 (early metastatic) time-points were cocultured with stimulated T cells and subsequent T cell proliferation was quantified by flow cytometry (Fig. 6.2A). A decrease in suppressive capacity of lung Gr-1$^+$ cells was seen at day 10 post inoculation compared with day 3, yet this change not observed in the other tissues (Figs. 6.2B and C).

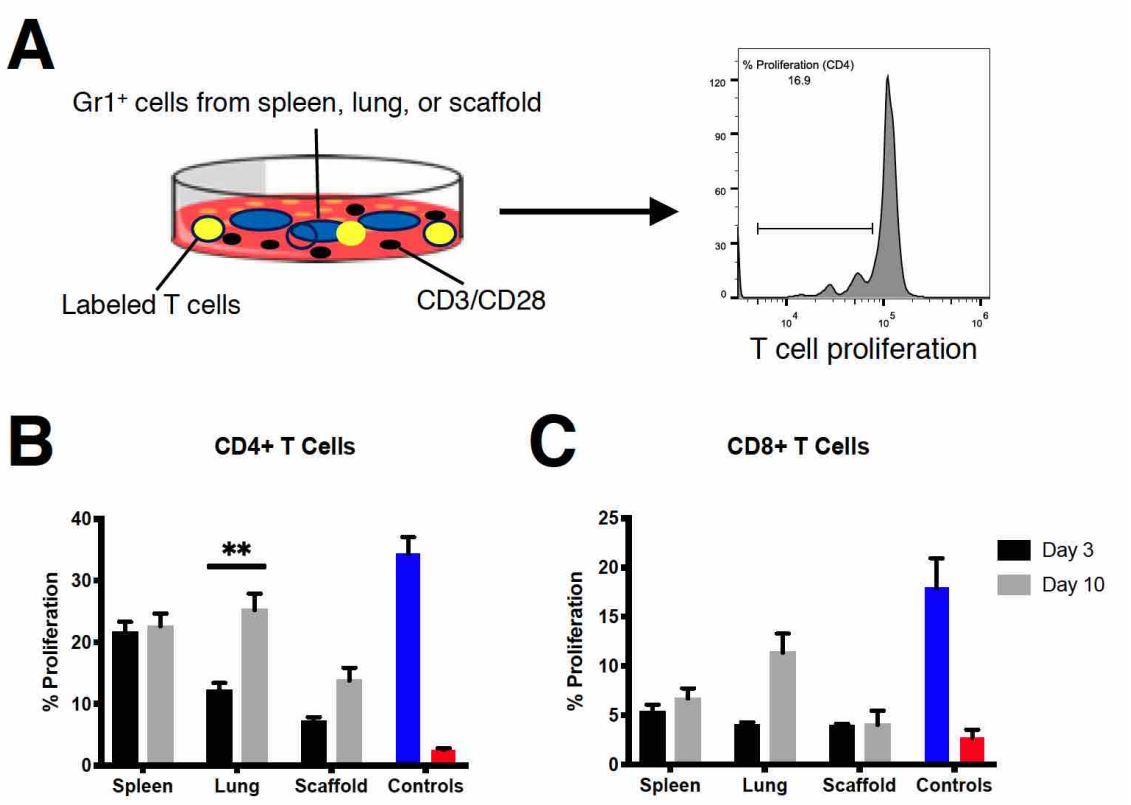

Figure 6.2: **Suppression of T cell proliferation by Gr-1$^+$ cells.** A) Schematic of T cell suppression assay. Suppression of B) CD4$^+$ T cell and C) CD8$^+$ T cell proliferation following coculture with Gr-1$^+$ cells.

6.4.2 Depletion of Gr-1$^+$ cells on disease progression

Next, systemic depletion with anti-Gr-1 antibody was employed to study the contribution of Gr-1$^+$ cells to disease progression and metastasis to *in vivo*. At both the pre-metastatic and early metastatic time points, anti-Gr-1 was able to deplete Gr-1$^+$ cells systemically and within tissues, though a fraction was detectable in the primary tumor with early metastatic treatment (Fig. 6.4). An intracardiac model wherein labeled tumor cells were injected into circulation following anti-Gr-1 treatment (Fig. 6.4A) did not indicate a difference in tumor cell accumulation at the scaffold (Fig. 6.4B) or the lung (Fig. 6.4C).

To examine the influence of Gr-1$^+$ cells on survival, tumor-bearing mice were

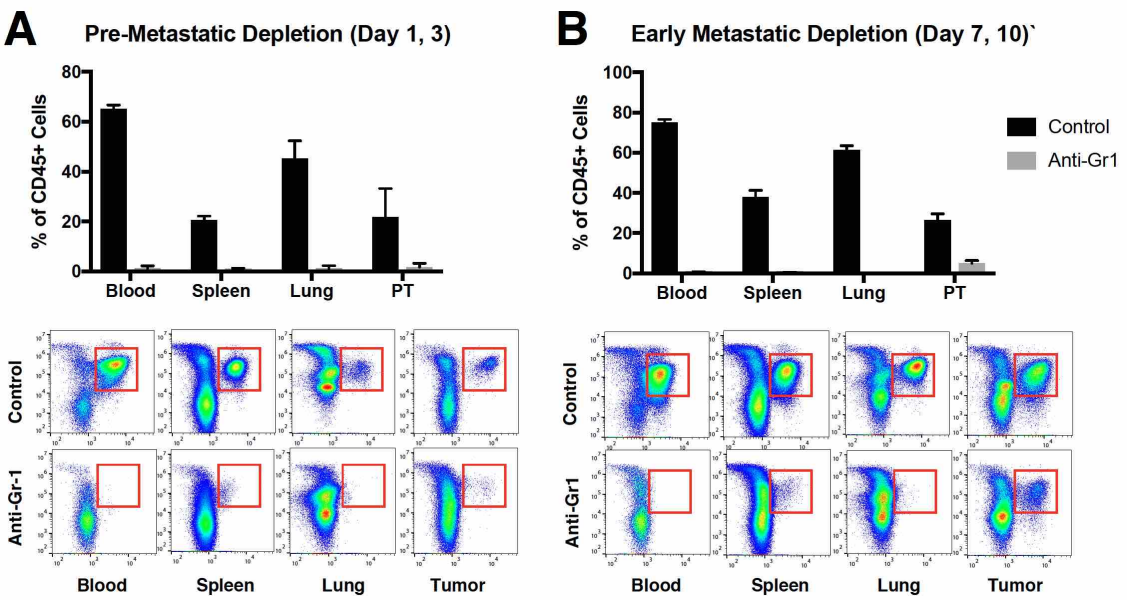

Figure 6.3: **Anti-Gr-1 depletes Gr-1$^+$ cells completely within tissues.** Following anti-Gr-1 treatment at (A) pre-metastatic and (B) early metastatic timepoints, Gr-1$^+$ cells were no longer detectable in nearly all tissues evaluated.

treated with anti-Gr-1 antibody at pre-metastatic (day 1, 4), early metastatic (day 7, 10), or late metastatic (day 14, 17) (Fig. 6.5A). Anti-Gr-1 treatment at the pre-metastatic timepoint resulted in increased metastasis and reduced survival time, while no survival benefit was observed with early-metastatic treatment (Figs. 6.5B and C). Late-metastatic treatment resulted in death of the animals within hours of injection, possibly due to massive cell loss that compromised organ function.

6.4.3 Tissue-specific and disease state-dependent gene expression changes in Gr-1$^+$ cells

Gene expression analysis by RNA-seq was employed to assess transcriptomic differences between Gr-1 cells at the various disease states and within different tissues (Fig. 6.6A). Gr-1$^+$ cells were isolated from the lung, spleen, and scaffolds of tumor-bearing mice by antibody-based magnetic bead separation (MACS) at days 3, 10, and 17 post inoculation. Principal component analysis delineated organs into sepa-

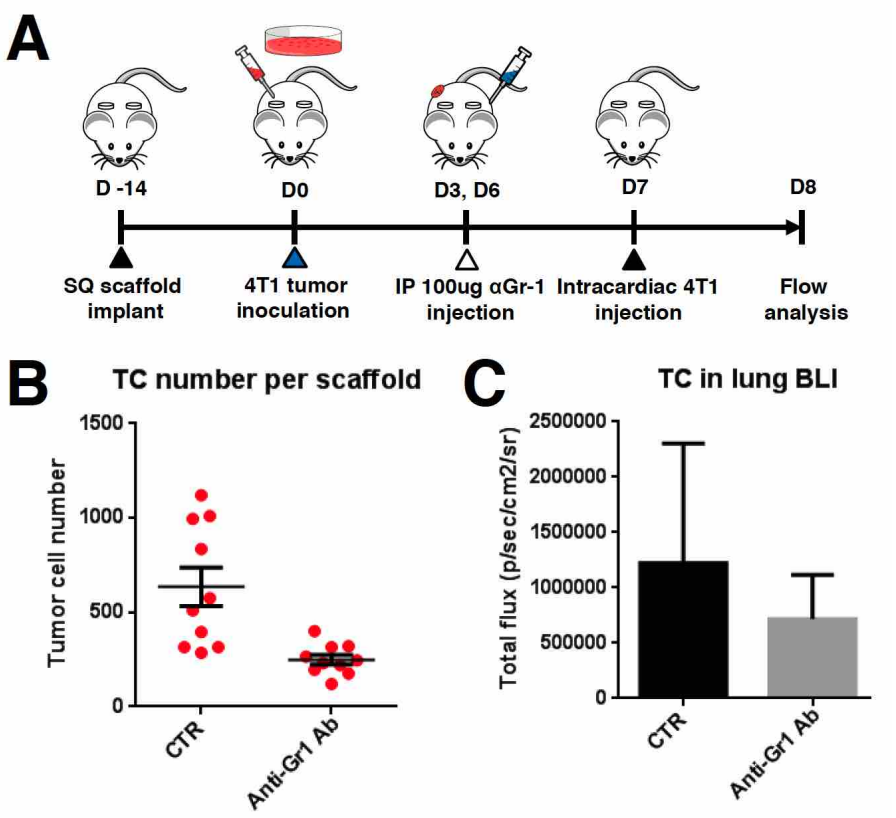

Figure 6.4: Intracardiac injection of Gr-1 cells following anti-Gr-1. (A) Schematic of intracardiac injection model for assessing tumor cell recruitment. (B) Quantification of tumor cells in scaffolds by flow cytometry. (C) Quantification of relative tumor cell abundance in the lung by IVIS.

rate populations, though overlap is observed for cells from the spleen at day 0 and day 3 post inoculation with cells from the lung at day 10 (Fig. 6.6B). Changes in pathway regulation over time was also examined using GSEA, and hierarchical clustering indicated that Gr-1$^+$ cells from scaffolds and lungs clustered more closely together than with the spleen (Fig. 6.7).

The most highly differentially-expressed pathways were identified and are shown in Figure 6.8. Cells within all three tissues showed a decrease in proliferation pathways from day 3 to day 10, and an increase from day 10 to day 17. The scaffold exhibited relative upregulation in inflammation pathways from day 3 to day 10, as well as a subsequent downregulation in those pathways from day 10 to 17. This trend

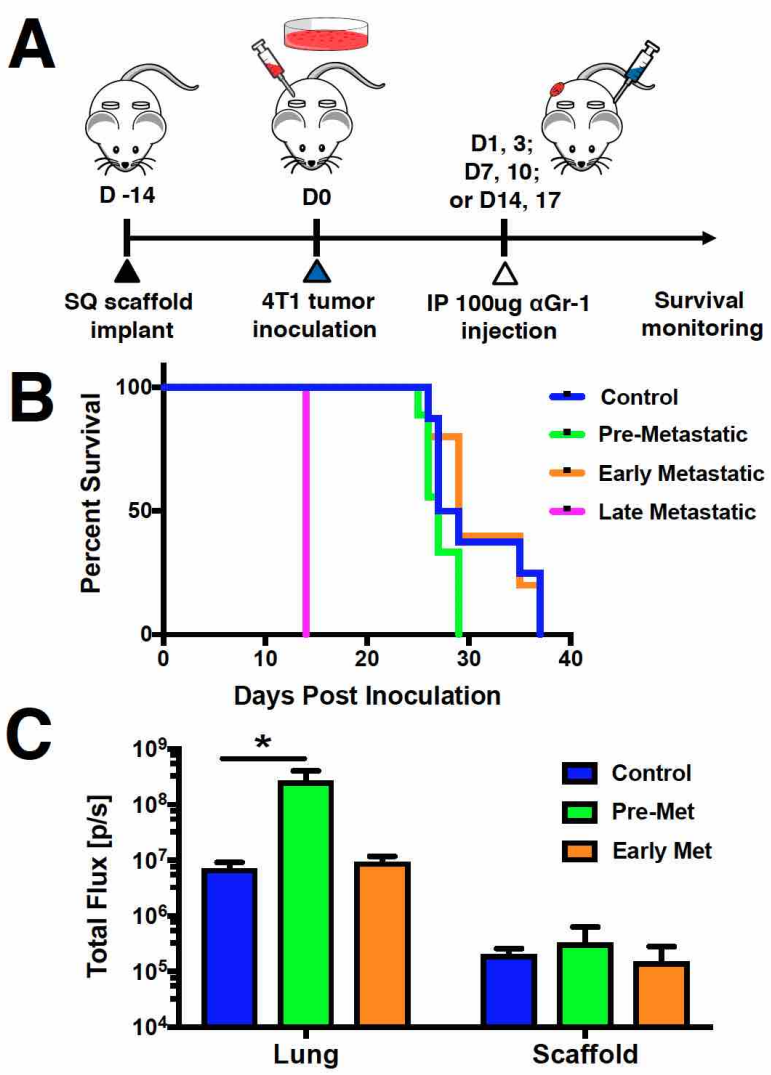

Figure 6.5: **Anti-Gr-1 exacerbates disease progression depending on time of treatment.** Mice were treated with 2 doses of anti-Gr-1 antibody starting at day 1 (pre-metastatic, day 7 (early metastatic), or day 14 (late metastatic). B) Pre-metastatic treatment resulted in accelerated disease progression compared with the untreated cohort. Animals treated at the late metastatic timepoint died following the first dose. C) An increase in lung metastasis was observed with pre-metastatic treatment.

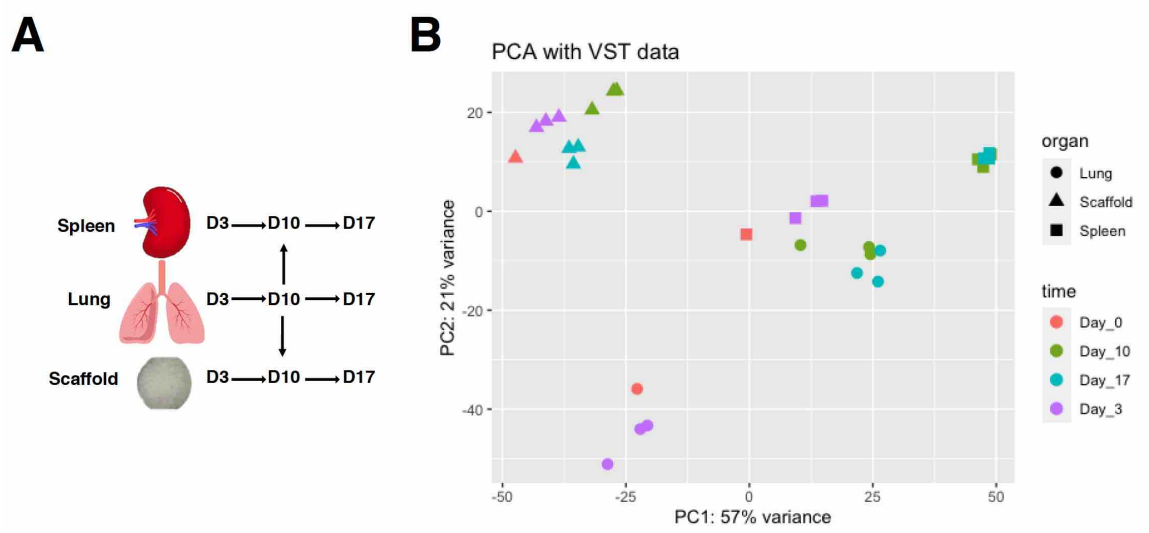

Figure 6.6: **Gene expression comparisons made and principal component analysis of RNAseq data for each organ and timepoint**.

was also observed in the spleen, though not in the lung. In addition, downregulation of T cell-related pathways was observed in the spleen throughout disease progression, while the lung and scaffold remained relatively unchanged.

6.5 Discussion

MDSCs, or Gr-1$^+$ cells, are an important part of the tumor microenvironment and have been shown to be involved in metastatic processes by promoting tumor growth and migration while inhibiting anti-tumor immune cell function [4, 5, 13]. As such, there has been much interest in using these cells for diagnostics as well as therapeutic targets [96, 162]. Much of what is known about the phenotype of Gr-1$^+$ cells is the result of *in vitro* functional assays, which often don't take into account the dependence of cell phenotype on the tissue of origin. It has been shown that Gr-1$^+$ cells within the spleen is functionally distinct from those within the primary tumor [163]. In this study, we used biomaterial scaffolds that recapitulate metastatic

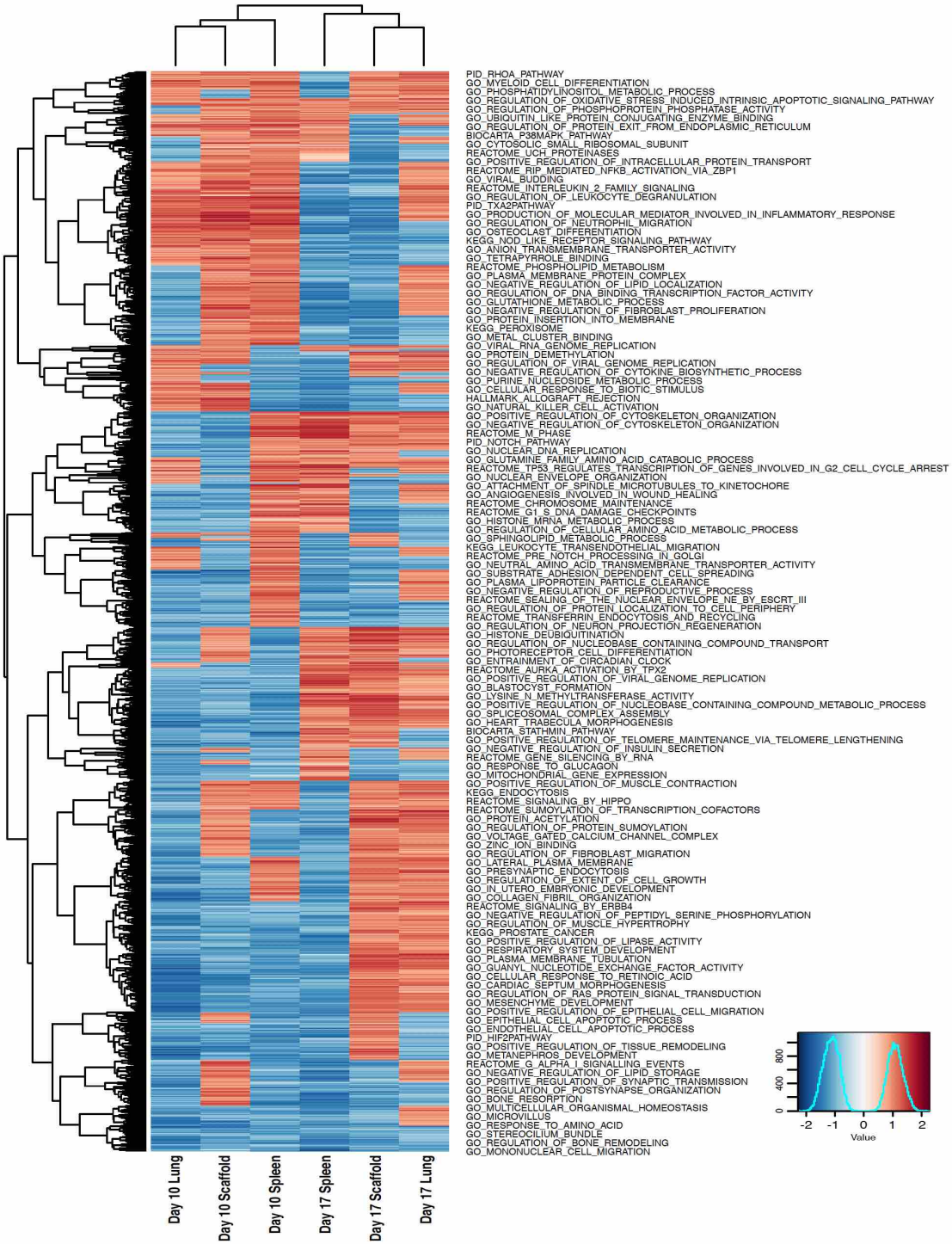

Figure 6.7: **Gene Set Enrichment Analysis of gene expression changes in Gr-1$^+$ cells over time and hierarchical clustering.**

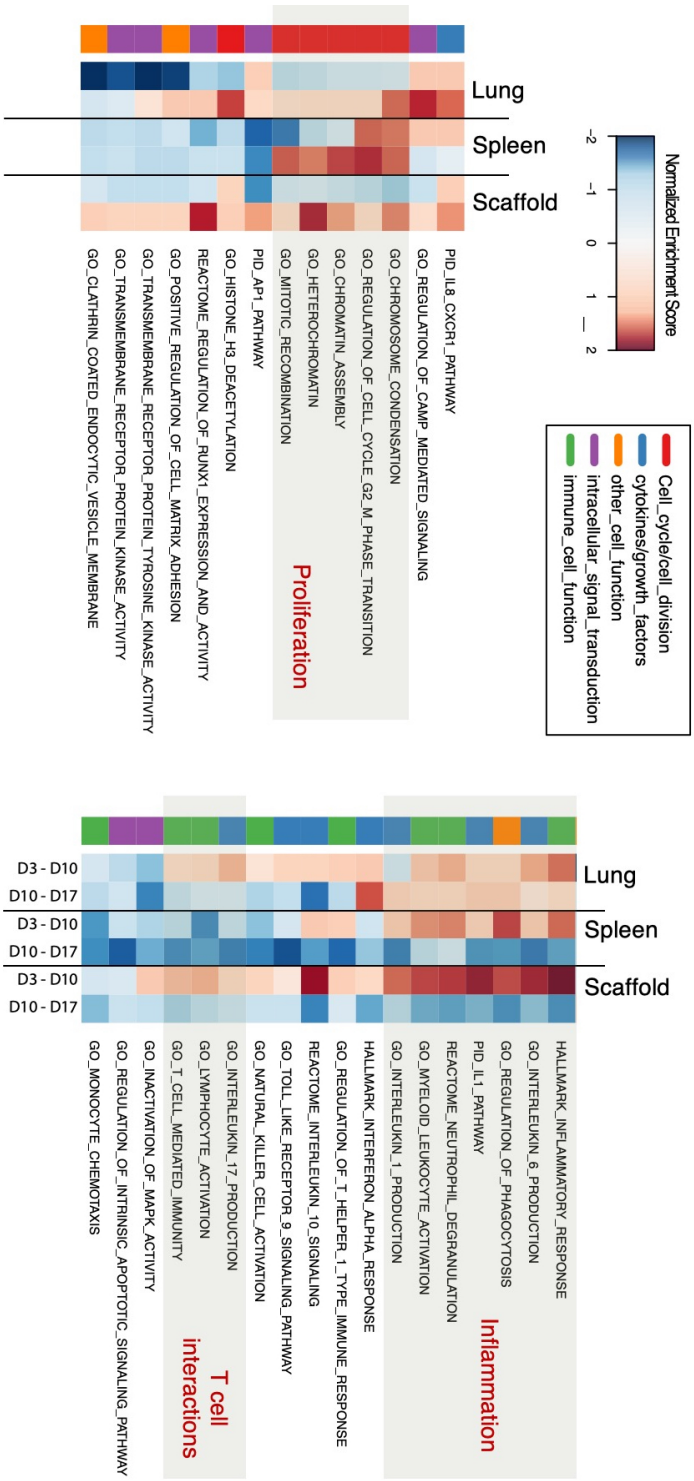

Figure 6.8: **Changes in select gene sets of interest for Gr-1$^+$ cells.**

sites to be able to more readily isolate and study Gr-1$^+$ cells at metastatic sites at various timepoints throughout disease progression.

We first compared conditioned media generated from Gr-1$^+$ cells of different tissues, and observed that cells from the lung and scaffold were able to recruit tumor cells in a transendothelial migration assay while those from the spleen were not. This difference is likely due to the secretion of different factors, which has previously been described between the spleen and tumor [163]. Of note, no changes in the ability to suppress T cell proliferation was observed over time in the spleen and scaffold, while there was a decrease in suppressive function at the lung.

We also employed RNA-sequencing to better understand the phenotypic differences between Gr-1$^+$ cells isolated from different organs and at different disease states. Pathway analysis was used to identify differences in proliferation, inflammatory function, and T cell interactions across the tissues and over time, adding to what is already known about functional differences between Gr-1$^+$ cell subsets. These results also indicate that Gr-1$^+$ cells that are recruited to the scaffold are more similar in phenotype to those at the metastatic lung than to those at the spleen, which suggests that the scaffold site can be used as a surrogate for studying metastatic sites *in situ*.

As MDSCs are being explored as diagnostics for cancer and metastasis, better understanding of Gr-1$^+$ cell function is needed. This study highlights the need to consider tissue of origin as well as disease state when assessing the function of MDSCs for diagnostics and treatment. Of note, depletion of Gr-1$^+$ cells at early disease states exacerbated disease and increased metastatic burden, and no therapeutic benefit was observed in any treatment group. In addition, treatment with anti-Gr-1 resulted in the death of all animals within the cohort upon late metastatic treat-

ment. These observations stand in contrast with the therapeutic benefit that been previously reported with targeting Gr-1$^+$ cells [162, 164]. As such, this study also brings to light the severe off-target effects that can potentially occur when broadly targeting Gr-1$^+$ cells.

6.6 Materials and Methods

6.6.1 Scaffold fabrication and implantation

Poly(ϵ-caprolactone) (PCL) microparticles, 4-8 um in diameter, were first synthesized prior to scaffold fabrication. PCL was dissolved in DCM at 6 w/w% at 4C overnight and mixed with 10 w/v% poly(vinyl alcohol) (PVA; 80% hydrolyzed, MW 9-10k; Sigma Aldrich) solution in water at 3:20 PCL:PVA volume ratio. The solution was then homogenized at 10,000 rpm for 1 minute to form the microparticles and immediately mixed with deionized (DI) water. The mixture was stirred, and the solvent was evaporated overnight. Microparticles were then washed 3 times with centrifugation and resuspension in DI water prior to lyophilization and long-term storage in a desiccator. Microparticles were used to fabricate 5 mm scaffolds as previously described [22]. Briefly, 2.5 mg of PCL microparticles was mixed with 75 mg of NaCl and pressed into a disc. Scaffolds were then melted 60°C and salt was leached from the scaffolds in MilliQ water. Leached scaffolds were disinfected in sterile-filtered 70% ethanol, rinsed in sterile MilliQ water, then dried and stored at -80°C. Frozen scaffolds were left on dry ice until implantation into the dorsal subcutaneous space. Each animal received 4 scaffolds. All animal procedures were performed in accordance with guidelines set by the Institutional Animal Care and Use Committee and Animal Care and Use Office at the University of Michigan. Mice

were anesthetized with 2% isoflurane during surgical procedures and received peri- and post-operative carprofen intraperitoneally at 5 mg/kg (Zoetis Inc.).

6.6.2 Tumor cell culture and inoculation

4T1-luc2-tdTomato cells (Perkin Elmer) were expanded in RPMI 1640 + GlutaMAX (Thermo Fisher Scientific) with 10% FBS for 5 days at 37°C and 5% CO_2 prior to inoculation. Cells were removed from culture flasks by incubation with trypsin for 10 minutes at 37°C and resuspended in RPMI 1640. Cells were then pelleted by centrifugation at 300 x g and washed with DPBS, and resuspended at 1 x 10^7 cells/mL of DPBS. Orthotopic tumor inoculations were performed by injection of 5 x 10^5 tumor cells resuspended in 50 μL DPBS (Life Technologies) into the fourth right mammary fat pad of 8- to 10-week-old female BALB/c mice (Jackson Laboratory). The cell line was confirmed to be pathogen free and authenticated by short tandem repeat DNA analysis and compared to the ATCC STR profile database (DDC Medical). For scaffold-implanted mice, tumor inoculation was performed 14 days post implant to allow for initial wound healing and tissue infiltration [22].

6.6.3 Gr-1$^+$ cell depletion and survival studies

Mice were treated twice with 100 ug of InVivoMab anti-mouse anti-Gr-1 (anti-Ly6C/Ly6G) antibody (clone RB6-8C5, Bio X Cell). Pre-metastatic treatment occurred on days 1 and 4 post tumor inoculation, early metastatic treatment occurred on days 7 and 10, and late metastatic treatment occurred on days 14 and 17. Antibody was diluted in DPBS to a final concentration of 1 mg/mL immediately prior to i.p. injection. For survival studies, mice were monitored for tumor size and body

conditioning. Mice were euthanized if any of the following criteria were met: tumor size of > 2 cm in any dimension, ulceration of more than 50% of the visible tumor area, partial paralysis due to tumor invasion of hind limb muscle, labored breathing, ascites, lethargy, or visible weight loss.

6.6.4 Intracardiac injection model of metastatic seeding

In the intracardiac model, mice were implanted with scaffolds as described above and inoculated with unlabeled 4T1 tumor cells, which were cultured as described above. Anti-Gr-1 was administered i.p. on days 3 and 6 post inoculation, following the formation of a primary tumor comprised of unlabeled 4T1 cells. 10^6 4T1-Luc2-tdTomato (labeled) cells were delivered by intracardiac injection. Flow cytometry was performed 24 hours post intracardiac injection to quantify the amount of labeled tumor cells within tissues to assess the ability of the tissues to recruit metastatic cells.

6.6.5 *Ex vivo* bioluminescence imaging

Metastatic tumor burden of luciferase-expressing tumor cells (4T1-Luc2-tdTomato) in explanted lungs and livers was measured by bioluminescence imaging with IVIS. Tissues were incubated in 50 μM d-luciferin (Caliper) at room temperature for 10 minutes prior to imaging. Imaging was performed with large binning, and exposure was automatically determined by the instrument to prevent signal saturation. Bioluminescence signal intensity is reported as integrated light flux (photons/sec) as calculated by the Living Image Software (Caliper Life Sciences).

6.6.6 Flow cytometry

Flow cytometry was performed on primary cells obtained from explanted spleens, lungs, primary tumors, and livers. Tissues were minced and enzyme digested with Liberase TL or TM (Roche), then filtered through a 70 μm cell strainer (Corning) to obtain a cell suspension. Whole blood was collected by cardiac puncture and mixed with 10 v/v% 25mM EDTA (Life Technologies). Red blood cell lysis of whole blood, spleens, and lungs was performed with ACK Lysing Buffer (Life Technologies). Cells were pelleted by centrifugation at 400 x g for 5 minutes and resuspended in MACS buffer. Nonspecific staining was blocked with anti-CD16/32 (Biolegend) and samples were stained for innate immune markers with anti-mouse CD45 AF700, F4/80 PE-Cy7, Ly6G PacBlue, Ly6C FITC (Biologend), and CD11b BV510 (BD Biosciences). Stained samples were analyzed using the MoFlo Astrios Flow Cytometer or CytoFLEX (Beckman Coulter), and data were processed using FlowJo software (BD).

6.6.7 Gr-1$^+$ cell sorting

Gr-1$^+$ cells were isolated by MACS from lungs, spleens, and scaffolds of tumor-bearing mice at 3, 10, and 17 days post tumor inoculation. Tissues were explanted, and a cell suspension was obtained for each tissue as described above. Red blood cell lysis was performed on lung and spleen samples with ACK Lysing Buffer (Life Technologies). Cells from multiple scaffolds in the same animal were pooled together. Cells were incubated with anti-Gr-1 antibody-conjugated magnetic microbeads from the mouse Myeloid-Derived Suppressor Cell Isolation Kit (Miltenyi), then passed through LS MACS Columns (Miltenyi) as per manufacturers instructions. The sorted

cells were washed and pelleted, then frozen and stored at -80C prior to gene expression analysis.

6.6.8 Gene expression analysis by RNA-seq

RNA was extracted from frozen Gr-1^+ cells that were sorted from lungs, spleens, and scaffolds as described above with the RNeasy Plus Mini spin column kit (Qiagen). Purified RNA concentration was measured by UV spectroscopy using a Nanodrop 2000c (Thermo Scientific) to confirm all samples had concentrations 10 ng/L. RNA quality control, QuantSeq 3' mRNA-seq library prep and quality control, and sequencing were all performed by the Advanced Genomics Core at the University of Michigan. Samples were sequenced using the Illumina NextSeq 550 sequencer. Raw sequencing counts were normalized and differential gene expression was calculated in R and using DESeq2 [95]. Normalization of raw counts was performed for principal component analysis [119] and genes with differential expression ($p_{adj} < 0.05$) were identified. To perform pathway analysis, mouse gene symbols for counts obtained through RNA-seq were first converted to human gene symbols using the biomaRt package in R. Gene Set Enrichment Analysis (GSEA) was performed on DESeq2-normalized counts and the corresponding human gene symbols for a total of 5,944 MsigDB gene sets (Hallmark, Reactome, PID, and Gene Ontology (GO)). A positive normalized enrichment score (NES) indicates enrichment compared to the control cohort.

6.6.9 Statistical analysis

One-way or two-way ANOVA and Tukeys multiple comparisons tests were performed on groups with more than 2 conditions. Two-tailed unpaired t test was used for single comparisons between two conditions. Median survival and survival curves were analyzed with the log-rank (Mantel-Cox) test for statistical significance. Following normalization of RNA-seq gene expression data with DESeq2, genes with adjusted p-value < 0.05 were considered differentially expressed. Statistical analyses were performed using Prism 8 (GraphPad Software). A p-value < 0.05 was considered to be statistically significant and all values are expressed in mean standard deviation (SD). Error bars on plotted data represent standard error of the mean (SEM).

CHAPTER VII

Conclusions and Future Directions

7.1 Summary of Findings

The work presented here describes the development and application of two biomaterial strategies that can be used to monitor and treat metastatic cancer as well as other immune-related disorders. Innate immune cells play a critical role in numerous disease states ranging from cancer to autoimmune disease, and even spinal cord injury. In spinal cord injury, neutrophils and monocytes are recruited to the injury site and cause inflammation that results in scarring and prevents tissue regeneration. The nanoparticles redirected and reprogrammed these innate cells, as evidenced by a reduction in the number of innate cells and inflammatory factors at the injury site, as well as an increase in pro-regenerative factors. Furthermore, nanoparticles improved myelination and resulted in motor function recovery.

In metastatic cancer, tumor cells secrete factors that induce proliferation and activation of suppressive innate immune cells, which inhibit T cell and NK cell killing of tumor cells. PLG nanoparticles were also shown to target disease-induced myeloid cells and decrease the abundancy of myeloid-derived suppressor cells at the metastatic organ and in circulation. Particle internalization appears to reprogram the cells to become more inflammatory, overcoming tumor-induced immunosuppression at the

tumor and lung. Furthermore, combination therapy of nanoparticles with anti-PD-1 increased IL-2 production in the lung, and increased cell killing at the tumor, resulting in slower growth of the primary tumor and lower metastatic burden in the lung.

This work also expands upon the applications of the PCL scaffold previously developed in the Shea lab. These scaffolds have previously been shown to recruit immune and tumor cells. The immune cells actively traffic to the scaffold due to the presence of the primary tumor, and as such, can be used as an indicator of disease progression. Gene expression analysis identified a panel of 10 genes that was able to capture systemic and disease-specific immune changes, and expression of these genes could be reduced to a scoring system that can be used to predict and monitor lung metastasis following resection of the primary tumor.

The scaffold was also used to study the phenotypes of Gr-1^+ cells within tissues and across multiple time points in the context of disease progression and metastasis. Anti-Gr-1 eliminated Gr-1^+ cells in the lung, liver, and spleen, while a fraction remained in the tumor, yet was shown to exacerbate tumor growth and metastasis when administered early. The phenotype of Gr-1^+ cells is shown to be dynamic with disease state (pre-, early, or late metastasis) as well as depend on the tissue of origin (scaffold, lung, or spleen), as indicated by their ability to suppress T cell proliferation and tumor cell recruitment, as well as by changes in their gene expression and pathway regulation.

7.2 Significance and Impact

This thesis highlights novel ways in which we can leverage biomaterial-immune interactions to address both acute inflammation in spinal cord injury and immunosuppression in metastatic cancer. We demonstrated targeting of the disease-induced innate immune cells in these models based on phagocytic phenotype alone rather than with targeting ligands, and observed phenotypic reprogramming of the immune cells that internalize them. Interestingly, the effect of PLG nanoparticles on immune cells appears to depend on the disease state of the animal. While nanoparticles reduced inflammation in the context of spinal cord injury, they appeared to increase inflammatory gene expression at the primary tumor and metastatic sites. These nanoparticles can easily be manufactured and are stable for long periods of time. This flexibility and potential tunability, combined with safety make nanoparticles a promising therapy for a wide variety of immune-related disorders.

In metastatic cancer, PCL scaffolds facilitate the formation of a local microenvironment that reflects immune changes at metastatic sites, which have previously studied only with biopsies of metastatic tissue. This work not only introduces a potential diagnostic or sensor for metastasis, but also adds to the understanding of immunosuppressive phenotypes of immune cells within metastatic sites. We observed that depletion of Gr-1$^+$ cells with anti-Gr-1 at early timepoints exacerbates disease and increases metastasis, and observed severe off-target effects with other treatment schedules. These negative outcomes may be under-reported as we were able to find only one other study that reported similar findings when using anti-Gr-1. The negative outcomes seen with anti-Gr-1 at certain timepoints highlight the need for the development of companion diagnostics and/or careful consideration of appropriate

dosing schedules in addition to the types of therapies that can target MDSCs and other innate immune cells.

7.3 Future Directions

7.3.1 Understanding the heterogeneity of Gr-1$^+$ cells within metastatic sites

MDSCs are known to be comprised of both granulocytic (G) and monocytic (M) populations, and that the two are phenotypically distinct. The relatively low abundance of M-MDSCs makes them difficult to sort by surface markers in order to study their gene expression in bulk. A recent study examined Gr-1$^+$ cells sorted from the spleen using single-cell RNA sequencing (scRNAseq) and identified previously unknown cell surface markers specific for a population of MDSCs within the spleen [165]. Applying scRNA to Gr-1$^+$ cells at the scaffold compared to those at the lung and spleen would help to elucidate whether the change in bulk gene expression with disease progression is due to changes in the relative abundance of Gr-1$^+$ populations or due to the appearance of a distinct population of Gr-1$^+$ cells at the early metastatic timepoint. In addition, scRNAseq may be able to identify unique druggable targets or surface receptors for pro-tumor Gr-1$^+$ cells to avoid off-target effects and negative outcomes observed with anti-Gr-1. In our studies, we assessed functional phenotype of Gr-1$^+$ cells based on their ability to suppress T cell proliferation. Additional functional studies such as quantifying production of nitric oxide or reactive oxygen species can be useful in further characterizing the dynamics of Gr-1$^+$ cells.

7.3.2 Optimizing nanoparticle properties for targeting specific cell types

As more is uncovered about the phenotype of the pro-tumor or pro-disease innate immune cells, more specific targeting of these cell types will likely be required. The work presented here took a first step at tuning PLG nanoparticles for preferential internalization by Ly6C^{hi} monocytes and MDSCs. As briefly described in Chapter IV, particle uptake can be tuned by physicochemical properties such as surface charge and particle size. Surface modification such as PEGylation of nanoparticles has also been explored by our group and others. To approach this, we can create a combinatorial library of rationally designed nanoparticles by using polymers with different molecular weights and varying surfactants.

Though intravascular infusion of nanoparticles is already a currently used and translatable method, we can also explore other routes of administration. Inhalable nanoparticles, for example, may be more effective for targeting the lung. However, where the cells are internalizing particles and where the cells accumulate if they leave the lung or circulation is a remaining question. To investigate this, we can incubate blood leukocytes with labeled nanoparticles and adoptively transfer them into mice that did not receive particle treatment to asses if particle biodistribution is different from that of mice injected with particles.

7.3.3 Monitoring of therapeutic response in other disease models

We demonstrated here that the scaffold facilitates the formation of an immune microenvironment that reflects disease-induced immune cell changes, but it is not known to what extent these changes can be detected. Recent studies suggest that these scaffolds are able to sense and predict the onset of relapse in a model of relapsing-

remitting multiple sclerosis (Morris et al., unpublished), even when there were no detectable changes in immune cell abundance or phenotype. These findings indicate the potential utility of the scaffold in a range of immune disorders. One such use may be to detect therapeutic efficacy for cancer vaccines. Robust T cell responses are necessary to generate tumor cell-specific immunity that results in tumor regression or prevention of metastasis. As such, it may be helpful to detect T cell changes or changes in other immune cells that engage with T cells in order to monitor therapeutic efficacy.

BIBLIOGRAPHY

BIBLIOGRAPHY

[1] Stephen Paget. THE DISTRIBUTION OF SECONDARY GROWTHS IN CANCER OF THE BREAST. *The Lancet*, 133(3421):571–573, 1889.

[2] Rosandra N. Kaplan, Rebecca D. Riba, Stergios Zacharoulis, Anna H. Bramley, Loïc Vincent, Carla Costa, Daniel D. MacDonald, David K. Jin, Koji Shido, Scott A. Kerns, Zhenping Zhu, Daniel Hicklin, Yan Wu, Jeffrey L. Port, Nasser Altorki, Elisa R. Port, Davide Ruggero, Sergey V. Shmelkov, Kristian K. Jensen, Shahin Rafii, and David Lyden. VEGFR1-positive haematopoietic bone marrow progenitors initiate the pre-metastatic niche. *Nature*, 438(7069):820–827, 2005.

[3] Gavin P. Dunn, Lloyd J. Old, and Robert D. Schreiber. The Immunobiology of Cancer Immunosurveillance and Immunoediting. *Immunity*, 21(2):137–148, 2004.

[4] Takanori Kitamura, Bin-Zhi Qian, and Jeffrey W. Pollard. Immune cell promotion of metastasis. *Nature Reviews Immunology*, 15(2):73–86, 2015.

[5] Dmitry I. Gabrilovich and Srinivas Nagaraj. Myeloid-derived-supressor cells as regulators of th eimmune system. *Nature Reviews Immunology*, 9(3):162–174, 2009.

[6] Bethan Psaila and David Lyden. The metastatic niche: adapting the foreign soil. *Nature Reviews Cancer*, 9:285–293, 2009.

[7] Jaclyn Sceneay, Melvyn T. Chow, Anna Chen, Heloise M. Halse, Christina S.F. Wong, Daniel M. Andrews, Erica K. Sloan, Belinda S. Parker, David D. Bowtell, Mark J. Smyth, and Andreas Möller. Primary tumor hypoxia recruits CD11b+/Ly6Cmed/ Ly6G+ immune suppressor cells and compromises NK cell cytotoxicity in the premetastatic niche. *Cancer Research*, 72(16):3906–3911, 2012.

[8] Rosandra N. Kaplan, Bethan Psaila, and David Lyden. *Cancer and Metastasis Reviews.*

[9] Janine T. Erler, Kevin L. Bennewith, Thomas R. Cox, Georgina Lang, Demelza Bird, Albert Koong, Quynh-Thu Le, and Amato J. Giaccia. Hypoxia-Induced Lysyl Oxidase Is a Critical Mediator of Bone Marrow Cell Recruitment to Form the Premetastatic Niche. *Cancer Cell*, 15(1):35–44, 2009.

[10] Xiaoyu Xiang, Anton Poliakov, Cunren Liu, Yuelong Liu, Zhong-bin Deng, Jianhua Wang, Ziqiang Cheng, Spandan V. Shah, Gui-Jun Wang, Liming Zhang, William E. Grizzle, Jim Mobley, and Huang-Ge Zhang. Induction of myeloid-derived suppressor cells by tumor exosomes. *International Journal of Cancer*, 124(11):2621–2633, 2009.

[11] Héctor Peinado, Maša Alečković, Simon Lavotshkin, Irina Matei, Bruno Costa-Silva, Gema Moreno-Bueno, Marta Hergueta-Redondo, Caitlin Williams, Guillermo García-Santos, Cyrus M. Ghajar, Ayuko Nitadori-Hoshino, Caitlin Hoffman, Karen Badal, Benjamin A. Garcia, Margaret K. Callahan, Jianda Yuan, Vilma R. Martins, Johan Skog, Rosandra N. Kaplan, Mary S. Brady, Jedd D. Wolchok, Paul B. Chapman, Yibin Kang, Jacqueline Bromberg, and David Lyden. Melanoma exosomes educate bone marrow progenitor cells toward a pro-metastatic phenotype through MET. *Nature Medicine*, 18(6):883–891, 2012.

[12] Ayuko Hoshino, Bruno Costa-Silva, Tang-Long Shen, Goncalo Rodrigues, Ayako Hashimoto, Milica Tesic Mark, Henrik Molina, Shinji Kohsaka, Angela Di Giannatale, Sophia Ceder, Swarnima Singh, Caitlin Williams, Nadine Soplop, Kunihiro Uryu, Lindsay Pharmer, Tari King, Linda Bojmar, Alexander E. Davies, Yonathan Ararso, Tuo Zhang, Haiying Zhang, Jonathan Hernandez, Joshua M. Weiss, Vanessa D. Dumont-Cole, Kimberly Kramer, Leonard H. Wexler, Aru Narendran, Gary K. Schwartz, John H. Healey, Per Sandstrom, Knut Jørgen Labori, Elin H. Kure, Paul M. Grandgenett, Michael A. Hollingsworth, Maria de Sousa, Sukhwinder Kaur, Maneesh Jain, Kavita Mallya, Surinder K. Batra, William R. Jarnagin, Mary S. Brady, Oystein Fodstad, Volkmar Muller, Klaus Pantel, Andy J. Minn, Mina J. Bissell, Benjamin A. Garcia, Yibin Kang, Vinagolu K. Rajasekhar, Cyrus M. Ghajar, Irina Matei, Hector Peinado, Jacqueline Bromberg, and David Lyden. Tumour exosome integrins determine organotropic metastasis. *Nature*, 527(7578):329–335, 2015.

[13] Vincenzo Bronte, Sven Brandau, Shu-Hsia Chen, Mario P. Colombo, Alan B. Frey, Tim F. Greten, Susanna Mandruzzato, Peter J. Murray, Augusto Ochoa, Suzanne Ostrand-Rosenberg, Paulo C. Rodriguez, Antonio Sica, Viktor Umansky, Robert H. Vonderheide, and Dmitry I. Gabrilovich. Recommendations for myeloid-derived suppressor cell nomenclature and characterization standards. *Nature Communications*, 7:12150, 2016.

[14] Carl H. June, Roddy S. O'Connor, Omkar U. Kawalekar, Saba Ghassemi, and Michael C. Milone. CAR T cell immunotherapy for human cancer. *Science*, 359(6382):1361–1365, 2018.

[15] Philip W. Kantoff, Celestia S. Higano, Neal D. Shore, E. Roy Berger, Eric J. Small, David F. Penson, Charles H. Redfern, Anna C. Ferrari, Robert Dreicer, Robert B. Sims, Yi Xu, Mark W. Frohlich, and Paul F. Schellhammer. Sipuleucel-T Immunotherapy for Castration-Resistant Prostate Cancer. *New England Journal of Medicine*, 363(5):411–422, 2010.

[16] Ruth A. Franklin, Will Liao, Abira Sarkar, Myoungjoo V. Kim, Michael R. Bivona, Kang Liu, Eric G. Pamer, and Ming O. Li. The cellular and molecular origin of tumor-associated macrophages. *Science*, 344(6186):921–925, 2014.

[17] Bin-Zhi Qian, Jiufeng Li, Hui Zhang, Takanori Kitamura, Jinghang Zhang, Liam R Campion, Elizabeth A Kaiser, Linda A Snyder, and Jeffrey W Pollard. CCL2 recruits inflammatory monocytes to facilitate breast-tumour metastasis. *Nature*, 475(7355):222–5, 2011.

[18] Debbie C. Strachan, Brian Ruffell, Yoko Oei, Mina J. Bissell, Lisa M. Coussens, Nancy Pryer, and Dylan Daniel. CSF1R inhibition delays cervical and mammary tumor growth in murine models by attenuating the turnover of tumor-associated macrophages and enhancing infiltration by CD8+ T cells. *OncoImmunology*, 2(12), 2013.

[19] Naoki Horikawa, Kaoru Abiko, Noriomi Matsumura, Tsukasa Baba, Junzo Hamanishi, Ken Yamaguchi, Ryusuke Murakami, Mana Taki, Masayo Ukita, Yuko Hosoe, Masafumi Koshiyama, Ikuo Konishi, and Masaki Mandai. Anti-VEGF therapy resistance in ovarian cancer is caused by GM-CSF-induced myeloid-derived suppressor cell recruitment. *British Journal of Cancer*, 122(6):778–788, 2020.

[20] Grace G. Bushnell, Tejaswini P. Hardas, Rachel M. Hartfield, Yining Zhang, Robert S. Oakes, Scott Ronquist, Haiming Chen, Indika Rajapakse, Max S. Wicha, Jacqueline S. Jeruss, and Lonnie D. Shea. Biomaterial Scaffolds Recruit an Aggressive Population of Metastatic Tumor Cells In Vivo. *Cancer Research*, 79(8):2042–2053, 2019.

[21] Samira M Azarin, Ji Yi, Robert M Gower, Brian A Aguado, Megan E Sullivan, Ashley G Goodman, Eric J Jiang, Shreyas S Rao, Yinying Ren, Susan L Tucker, Vadim Backman, Jacqueline S Jeruss, and Lonnie D Shea. In vivo capture and label-free detection of early metastatic cells. *Nature Communications*, 6(1):8094, 2015.

[22] Shreyas S. Rao, Grace G. Bushnell, Samira M. Azarin, Graham Spicer, Brian A. Aguado, Jenna R. Stoehr, Eric J. Jiang, Vadim Backman, Lonnie D. Shea, and Jacqueline S. Jeruss. Enhanced survival with implantable scaffolds that capture metastatic breast cancer cells in vivo. *Cancer Research*, 76(18):5209–5218, 2016.

[23] Alexandre De La Fuente, Lorena Alonso-Alconada, Clotilde Costa, Juan Cueva, Tomas Garcia-Caballero, Rafael Lopez-Lopez, and Miguel Abal. M-Trap: Exosome-Based Capture of Tumor Cells as a New Technology in Peritoneal Metastasis. *Journal of the National Cancer Institute*, 107(9):1–10, 2015.

[24] Cheng-Yu Ko, Lanxiao Wu, Ashwin M. Nair, Yi-Ting Tsai, Victor K. Lin, and Liping Tang. The use of chemokine-releasing tissue engineering scaffolds in a model of inflammatory response-mediated melanoma cancer metastasis. *Biomaterials*, 33(3):876–885, 2012.

[25] Grace G. Bushnell, Shreyas S. Rao, Rachel M. Hartfield, Yining Zhang, Robert S. Oakes, Jacqueline S. Jeruss, and Lonnie D. Shea. Microporous scaffolds loaded with immunomodulatory lentivirus to study the contribution of immune cell populations to tumor cell recruitment in vivo. *Biotechnology and Bioengineering*, 117(1):210–222, 2020.

[26] David G. DeNardo, Donal J. Brennan, Elton Rexhepaj, Brian Ruffell, Stephen L. Shiao, Stephen F. Madden, William M. Gallagher, Nikhil Wadhwani, Scott D. Keil, Sharfaa A. Junaid, Hope S. Rugo, E. Shelley Hwang, Karin Jirström, Brian L. West, and Lisa M. Coussens. Leukocyte complexity predicts breast cancer survival and functionally regulates response to chemotherapy. *Cancer Discovery*, 1(1):54–67, 2011.

[27] Elisa Peranzoni, Jean Lemoine, Lene Vimeux, Vincent Feuillet, Sarah Barrin, Chahrazade Kantari-Mimoun, Nadège Bercovici, Marion Guérin, Jérôme Biton, Hanane Ouakrim, Fabienne Régnier, Audrey Lupo, Marco Alifano, Diane Damotte, and Emmanuel Donnadieu. Macrophages impede CD8 T cells from reaching tumor cells and limit the efficacy of antiPD-1 treatment. *Proceedings of the National Academy of Sciences of the United States of America*, 115(17):E4041–E4050, 2018.

[28] Stefanie K. Wculek and Ilaria Malanchi. Neutrophils support lung colonization of metastasis-initiating breast cancer cells. *Nature*, advance on:1–21, 2015.

[29] Xiaocan Guo, Yang Zhao, Huan Yan, Yingcheng Yang, Shuying Shen, Xiaoming Dai, Xinyan Ji, Fubo Ji, Xing-Guo Gong, Li Li, Xueli Bai, Xin-Hua Feng, Tingbo Liang, Junfang Ji, Lei Chen, Hongyang Wang, and Bin Zhao. Single tumor-initiating cells evade immune clearance by recruiting type II macrophages. *Genes & Development*, 31(3):247–259, 2017.

[30] Huaiyu Zhang, Shujun Dong, Zhongmin Li, and Xiangru Feng. Biointerface engineering nanoplatforms for cancer-targeted drug delivery. *Asian Journal of Pharmaceutical Sciences*, 2019.

[31] Jason M. Fritz, Meredith A. Tennis, David J. Orlicky, Hao Lin, Cynthia Ju, Elizabeth F. Redente, Kevin S. Choo, Taylor A. Staab, Ronald J. Bouchard, Daniel T. Merrick, Alvin M. Malkinson, and Lori D. Dwyer-Nield. Depletion of Tumor-Associated Macrophages Slows the Growth of Chemically Induced Mouse Lung Adenocarcinomas. *Frontiers in Immunology*, 5, 2014.

[32] Chenran Zhang, Liquan Gao, Yuehong Cai, Hao Liu, Duo Gao, Jianhao Lai, Bing Jia, Fan Wang, and Zhaofei Liu. Inhibition of tumor growth and metastasis by photoimmunotherapy targeting tumor-associated macrophage in a sorafenib-resistant tumor model. *Biomaterials*, 84:1–12, 2016.

[33] Joseph A. Flores-Toro, Defang Luo, Adithya Gopinath, Matthew R Sarkisian, James J Campbell, Israel F Charo, Rajinder Singh, Thomas J. Schall, Meenal Datta, Rakesh K. Jain, Duane A. Mitchell, and Jeffrey K. Harrison. CCR2 inhibition reduces tumor myeloid cells and

unmasks a checkpoint inhibitor effect to slow progression of resistant murine gliomas. *Proceedings of the National Academy of Sciences*, 117(2):1129–1138, 2020.

[34] Jerry Silver and Jared H. Miller. Regeneration beyond the glial scar. *Nature Reviews Neuroscience*, 5(2):146–156, 2004.

[35] Glenn Yiu and Zhigang He. Glial inhibition of CNS axon regeneration. *Nature Reviews Neuroscience*, 7(8):617–627, 2006.

[36] Jonghyuck Park, Eunjeong Lim, Seungkeun Back, Heungsik Na, Yongdoo Park, and Kyung Sun. Nerve regeneration following spinal cord injury using matrix metalloproteinase-sensitive, hyaluronic acid-based biomimetic hydrogel scaffold containing brain-derived neurotrophic factor. *Journal of Biomedical Materials Research Part A*, 93A(3):1091–1099, 2009.

[37] Dustin J. Donnelly and Phillip G. Popovich. Inflammation and its role in neuroprotection, axonal regeneration and functional recovery after spinal cord injury. *Experimental neurology*, 209(2):378–88, 2008.

[38] Michael R. Due, Jonghyuck Park, Lingxing Zheng, Michael Walls, Yohance M. Allette, Fletcher A. White, and Riyi Shi. Acrolein involvement in sensory and behavioral hypersensitivity following spinal cord injury in the rat. *Journal of Neurochemistry*, 128(5):776–786, 2014.

[39] Zhe Chen, Jonghyuck Park, Breanne Butler, Glen Acosta, Sasha Vega-Alvarez, Lingxing Zheng, Jonathan Tang, Robyn McCain, Wenpeng Zhang, Zheng Ouyang, Peng Cao, and Riyi Shi. Mitigation of sensory and motor deficits by acrolein scavenger phenelzine in a rat model of spinal cord contusive injury. *Journal of Neurochemistry*, 138(2):328–338, 2016.

[40] Riyi Shi, Breanne Muratori, and Jonghyuck Park. Acrolein as a novel therapeutic target for motor and sensory deficits in spinal cord injury. *Neural Regeneration Research*, 9(7):677, 2014.

[41] Jonghyuck Park, Joseph T. Decker, Dominique R. Smith, Brian J. Cummings, Aileen J. Anderson, and Lonnie D. Shea. Reducing inflammation through delivery of lentivirus encoding for anti-inflammatory cytokines attenuates neuropathic pain after spinal cord injury. *Journal of Controlled Release*, 290:88–101, 2018.

[42] Jonghyuck Park, Lingxing Zheng, Glen Acosta, Sasha Vega-Alvarez, Zhe Chen, Breanne Muratori, Peng Cao, and Riyi Shi. Acrolein contributes to TRPA1 up-regulation in peripheral and central sensory hypersensitivity following spinal cord injury. *Journal of Neurochemistry*, 135(5):987–997, 2015.

[43] Jing Wang. Neutrophils in tissue injury and repair. *Cell and Tissue Research*, 371(3):531–539, 2018.

[44] Daniel R Getts, Aaron J Martin, Derrick P McCarthy, Rachael L Terry, Zoe N Hunter, Woon Teck Yap, Meghann Teague Getts, Michael Pleiss, Xunrong Luo, Nicholas J C King, Lonnie D Shea, and Stephen D Miller. Microparticles bearing encephalitogenic peptides induce T-cell tolerance and ameliorate experimental autoimmune encephalomyelitis. *Nature biotechnology*, 30(12):1217–24, 2012.

[45] D. R. Getts, Rachael L Terry, Meghann Teague Getts, Celine Deffrasnes, M. Muller, C. van Vreden, Thomas M Ashhurst, Belal Chami, D. McCarthy, Huiling Wu, Jin Ma, Aaron Martin, Lonnie D Shae, Paul Witting, Geoffrey S Kansas, J. Kuhn, Wali Hafezi, Iain L Campbell, David Reilly, Jana Say, Louise Brown, Melanie Y White, Stuart J Cordwell, Steven J Chadban, Edward B Thorp, Shisan Bao, Stephen D Miller, and Nicholas J C King. Therapeutic Inflammatory Monocyte Modulation Using Immune-Modifying Microparticles. *Science Translational Medicine*, 6(219):219ra7, 2014.

[46] Daniel R. Getts, Lonnie D. Shea, Stephen D. Miller, and Nicholas J.C. King. Harnessing nanoparticles for immune modulation. *Trends in Immunology*, 36(7):419–427, jul 2015.

[47] John C. Gensel and Bei Zhang. Macrophage activation and its role in repair and pathology after spinal cord injury. *Brain Research*, 1619:1–11, 2015.

[48] Su Ji Jeong, John G. Cooper, Igal Ifergan, Tammy L. McGuire, Dan Xu, Zoe Hunter, Sripadh Sharma, Derrick McCarthy, Stephen D. Miller, and John A. Kessler. Intravenous immune-modifying nanoparticles as a therapy for spinal cord injury in mice. *Neurobiology of Disease*, 108:73–82, 2017.

[49] Chia-Lin Tsou, Wendy Peters, Yue Si, Sarah Slaymaker, Ara M. Aslanian, Stuart P. Weisberg, Matthias Mack, and Israel F. Charo. Critical roles for CCR2 and MCP-3 in monocyte mobilization from bone marrow and recruitment to inflammatory sites. *Journal of Clinical Investigation*, 117(4):902–909, 2007.

[50] Robert Kuo, Eiji Saito, Stephen D. Miller, and Lonnie D. Shea. Peptide-Conjugated Nanoparticles Reduce Positive Co-stimulatory Expression and T Cell Activity to Induce Tolerance. *Molecular Therapy*, 25(7):1676–1685, 2017.

[51] Samuel David and Antje Kroner. Repertoire of microglial and macrophage responses after spinal cord injury. *Nature Reviews Neuroscience*, 12(7):388–399, 2011.

[52] Daniel J. Margul, Jonghyuck Park, Ryan M. Boehler, Dominique R. Smith, Mitchell A. Johnson, Dylan A. McCreedy, Ting He, Aishani Ataliwala, Todor V. Kukushliev, Jesse Liang, Alireza Sohrabi, Ashley G. Goodman, Christopher M. Walthers, Lonnie D. Shea, and Stephanie K. Seidlits. Reducing neuroinflammation by delivery of IL-10 encoding lentivirus from multiple-channel bridges. *Bioengineering & Translational Medicine*, 1(2):136–148, 2016.

[53] Jonghyuck Park, Joseph T. Decker, Daniel J. Margul, Dominique R. Smith, Brian J. Cummings, Aileen J. Anderson, and Lonnie D. Shea. Local Immunomodulation with Anti-inflammatory Cytokine-Encoding Lentivirus Enhances Functional Recovery after Spinal Cord Injury. *Molecular Therapy*, 26(7):1756–1770, 2018.

[54] Kristina A. Kigerl, John C. Gensel, Daniel P. Ankeny, Jessica K. Alexander, Dustin J. Donnelly, and Phillip G. Popovich. Identification of Two Distinct Macrophage Subsets with Divergent Effects Causing either Neurotoxicity or Regeneration in the Injured Mouse Spinal Cord. *Journal of Neuroscience*, 29(43):13435–13444, 2009.

[55] Mousumi Ghosh and Damien D. Pearse. The role of the serotonergic system in locomotor recovery after spinal cord injury. *Frontiers in Neural Circuits*, 8:151, 2015.

[56] Brian J. Schmidt and Larry M. Jordan. The role of serotonin in reflex modulation and locomotor rhythm production in the mammalian spinal cord. *Brain Research Bulletin*, 53(5):689–710, 2000.

[57] Ninh M. La-Beck and Alberto A. Gabizon. Nanoparticle Interactions with the Immune System: Clinical Implications for Liposome-Based Cancer Chemotherapy. *Frontiers in Immunology*, 8, 2017.

[58] Kim, Eun Hyun Ahn, Tal Dvir, and Deok-Ho Kim. Emerging nanotechnology approaches in tissue engineering and regenerative medicine. *International Journal of Nanomedicine*, page 1, 2014.

[59] Daniel R. Getts, Rachael L. Terry, Meghann Teague Getts, Marcus Muller, Sabita Rana, Bimmi Shrestha, Jane Radford, Nico Van Rooijen, Iain L. Campbell, and Nicholas J.C. King. Ly6c+ inflammatory monocytes are microglial precursors recruited in a pathogenic manner in West Nile virus encephalitis. *Journal of Experimental Medicine*, 205(10):2319–2337, 2008.

[60] Courtney M. Dumont, Jonghyuck Park, and Lonnie D. Shea. Controlled release strategies for modulating immune responses to promote tissue regeneration. *Journal of Controlled Release*, 219:155–166, 2015.

[61] Samuel David, Rubèn López-Vales, and V. Wee Yong. Harmful and beneficial effects of inflammation after spinal cord injury. In *Handbook of Clinical Neurology*, pages 485–502. 2012.

[62] Benjamin T. Noble, Faith H. Brennan, and Phillip G. Popovich. The spleen as a neuroimmune interface after spinal cord injury. *Journal of Neuroimmunology*, 321:1–11, 2018.

[63] Ryan M. Pearson, Liam M. Casey, Kevin R. Hughes, Leon Z. Wang, Madeleine G. North, Daniel R. Getts, Stephen D. Miller, and Lonnie D. Shea. Controlled Delivery of Single or Multiple Antigens in Tolerogenic Nanoparticles Using Peptide-Polymer Bioconjugates. *Molecular Therapy*, 25(7):1655–1664, 2017.

[64] Suzanne E. Hickman, Nathan D. Kingery, Toshiro K. Ohsumi, Mark L. Borowsky, Li-chong Wang, Terry K. Means, and Joseph El Khoury. The microglial sensome revealed by direct RNA sequencing. *Nature Neuroscience*, 16(12):1896–1905, 2013.

[65] Florian Leuschner, Partha Dutta, Rostic Gorbatov, Tatiana I. Novobrantseva, Jessica S. Donahoe, Gabriel Courties, Kang Mi Lee, James I. Kim, James F. Markmann, Brett Marinelli, Peter Panizzi, Won Woo Lee, Yoshiko Iwamoto, Stuart Milstein, Hila Epstein-Barash, William Cantley, Jamie Wong, Virna Cortez-Retamozo, Andita Newton, Kevin Love, Peter Libby, Mikael J. Pittet, Filip K. Swirski, Victor Koteliansky, Robert Langer, Ralph Weissleder, Daniel G. Anderson, and Matthias Nahrendorf. Therapeutic siRNA silencing in inflammatory monocytes in mice. *Nature Biotechnology*, 29(11):1005–1010, 2011.

[66] Peter Boros, Jordi C. Ochando, Shu-Hsia Chen, and Jonathan S. Bromberg. Myeloid-derived suppressor cells: Natural regulators for transplant tolerance. *Human Immunology*, 71(11):1061–1066, 2010.

[67] Thomas Wynn and Luke Barron. Macrophages: Master Regulators of Inflammation and Fibrosis. *Seminars in Liver Disease*, 30(03):245–257, 2010.

[68] Y. Zhu, C. Soderblom, V. Krishnan, J. Ashbaugh, J.R. Bethea, and J.K. Lee. Hematogenous macrophage depletion reduces the fibrotic scar and increases axonal growth after spinal cord injury. *Neurobiology of Disease*, 74:114–125, 2015.

[69] Jonghyuck Park, Lingxing Zheng, Andrew Marquis, Michael Walls, Brad Duerstock, Amber Pond, Sasha Vega-Alvarez, He Wang, Zheng Ouyang, and Riyi Shi. Neuroprotective role of hydralazine in rat spinal cord injury-attenuation of acrolein-mediated damage. *Journal of Neurochemistry*, 129(2):339–349, 2014.

[70] Dongming Cai, Kangwen Deng, Wilfredo Mellado, Junghee Lee, Rajiv R. Ratan, and Marie T. Filbin. Arginase I and Polyamines Act Downstream from Cyclic AMP in Overcoming Inhibition of Axonal Growth MAG and Myelin In Vitro. *Neuron*, 35(4):711–719, 2002.

[71] Zhigang Zhou, Xiangmin Peng, Ryan Insolera, David J. Fink, and Marina Mata. Interleukin-10 provides direct trophic support to neurons. *Journal of Neurochemistry*, 110(5):1617–1627, 2009.

[72] Veronique E. Miron, Amanda Boyd, Jing-Wei Zhao, Tracy J. Yuen, Julia M. Ruckh, Jennifer L. Shadrach, Peter van Wijngaarden, Amy J. Wagers, Anna Williams, Robin J M Franklin, and Charles Ffrench-Constant. M2 microglia and macrophages drive oligodendrocyte differentiation during CNS remyelination. *Nature Neuroscience*, 16(9):1211–1218, 2013.

[73] David M. de Kretser, Robyn E. O'Hehir, Charles L. Hardy, and Mark P. Hedger. The roles of activin A and its binding protein, follistatin, in inflammation and tissue repair. *Molecular and Cellular Endocrinology*, 359(1-2):101–106, 2012.

[74] Kiran Pawar, Brian J. Cummings, Aline Thomas, Lonnie D. Shea, Ariel Levine, Sam Pfaff, and Aileen J. Anderson. Biomaterial bridges enable regeneration and re-entry of corticospinal tract axons into the caudal spinal cord after SCI: Association with recovery of forelimb function. *Biomaterials*, 65:1–12, 2015.

[75] Hirenkumar K. Makadia and Steven J. Siegel. Poly Lactic-co-Glycolic Acid (PLGA) as Biodegradable Controlled Drug Delivery Carrier. *Polymers*, 3(3):1377–1397, 2011.

[76] Qiuju Yuan, Huanxing Su, Kin Chiu, Zhi-Xiu Lin, and Wutian Wu. Assessment of the rate of spinal motor axon regeneration by choline acetyltransferase immunohistochemistry following sciatic nerve crush injury in mice. *Journal of Neurosurgery*, 120(2):502–508, 2014.

[77] Kenneth J. Livak and Thomas D. Schmittgen. Analysis of Relative Gene Expression Data Using Real-Time Quantitative PCR and the 2ΔΔCT Method. *Methods*, 25(4):402–408, 2001.

[78] Makoto Ishii, Haitao Wen, Callie A. S. Corsa, Tianju Liu, Ana L. Coelho, Ronald M. Allen, William F. Carson, Karen A. Cavassani, Xiangzhi Li, Nicholas W. Lukacs, Cory M. Hogaboam, Yali Dou, and Steven L. Kunkel. Epigenetic regulation of the alternatively activated macrophage phenotype. *Blood*, 114(15):3244–3254, 2009.

[79] D. Michele Basso, Lesley C. Fisher, Aileen J. Anderson, Lyn B. Jakeman, Dana M. Mctigue, and Phillip G. Popovich. Basso Mouse Scale for Locomotion Detects Differences in Recovery after Spinal Cord Injury in Five Common Mouse Strains. *Journal of Neurotrauma*, 23(5):635–659, may 2006.

[80] Asghar Ghasemi and Saleh Zahediasl. Normality Tests for Statistical Analysis: A Guide for Non-Statisticians. *International Journal of Endocrinology and Metabolism*, 10(2):486–489, 2012.

[81] Binzhi Qian, Yan Deng, Jae Hong Im, Ruth J. Muschel, Yiyu Zou, Jiufeng Li, Richard A. Lang, and Jeffrey W. Pollard. A distinct macrophage population mediates metastatic breast cancer cell extravasation, establishment and growth. *PLoS ONE*, 4(8), 2009.

[82] Sunil Singhal, Jason Stadanlick, Michael J. Annunziata, Abhishek S. Rao, Pratik S. Bhojnagarwala, Shaun O'Brien, Edmund K. Moon, Edward Cantu, Gwenn Danet-Desnoyers, Hyun Jeong Ra, Leslie Litzky, Tatiana Akimova, Ulf H. Beier, Wayne W. Hancock, Steven M. Albelda, and Evgeniy B. Eruslanov. Human tumor-associated monocytes/macrophages and their regulation of T cell responses in early-stage lung cancer. *Science Translational Medicine*, 11(479), 2019.

[83] Lillian Sun, Paul E. Clavijo, Yvette Robbins, Priya Patel, Jay Friedman, Sarah Greene, Rita Das, Chris Silvin, Carter Van Waes, Lucas A. Horn, Jeffrey Schlom, Claudia Palena, Dean Maeda, John Zebala, and Clint T. Allen. Inhibiting myeloid-derived suppressor cell trafficking enhances T cell immunotherapy. *JCI Insight*, 4(7), 2019.

[84] Silvina Gazzaniga, Alicia I. Bravo, Angelo Guglielmotti, Nico Van Rooijen, Fabricio Maschi, Annunciata Vecchi, Alberto Mantovani, José Mordoh, and Rosa Wainstok. Targeting tumor-associated macrophages and inhibition of MCP-1 reduce angiogenesis and tumor growth in a human melanoma xenograft. *Journal of Investigative Dermatology*, 127(8):2031–2041, 2007.

[85] Ana M Gil-Bernabé, Spela Ferjancic, Monika Tlalka, Lei Zhao, Philip D Allen, Jae Hong Im, Karla Watson, Sally A Hill, Ali Amirkhosravi, John L Francis, Jeffrey W Pollard, Wolfram Ruf, and Ruth J Muschel. Recruitment of monocytes/macrophages by tissue factor-mediated coagulation is essential for metastatic cell survival and premetastatic niche establishment in mice. *Blood*, 119(13):3164–3175, 2012.

[86] Sean H. Colligan, Stephanie L. Tzetzo, and Scott I. Abrams. Myeloid-driven mechanisms as barriers to antitumor CD8+ T cell activity. *Molecular Immunology*, 118(September 2019):165–173, 2020.

[87] Wei He, Neha Kapate, C. Wyatt Shields, and Samir Mitragotri. Drug delivery to macrophages: A review of targeting drugs and drug carriers to macrophages for inflammatory diseases. *Advanced Drug Delivery Reviews*, 2019.

[88] Kyohei Nakamura and Mark J. Smyth. Myeloid immunosuppression and immune checkpoints in the tumor microenvironment. *Cellular and Molecular Immunology*, (September):1–12, 2019.

[89] Mohammad Rashidian, Martin W. LaFleur, Vincent L. Verschoor, Anushka Dongre, Yun Zhang, Thao H. Nguyen, Stephen Kolifrath, Amir R. Aref, Christie J. Lau, Cloud P. Paweletz, Xia Bu, Gordon J. Freeman, M. Inmaculada Barrasa, Robert A. Weinberg, Arlene H. Sharpe, and Hidde L. Ploegh. Immuno-PET identifies the myeloid compartment as a key contributor to the outcome of the antitumor response under PD-1 blockade. *Proceedings of the National Academy of Sciences of the United States of America*, 116(34):16971–16980, 2019.

[90] Melissa G. Lechner, Daniel J. Liebertz, and Alan L. Epstein. Characterization of Cytokine-Induced Myeloid-Derived Suppressor Cells from Normal Human Peripheral Blood Mononuclear Cells. *The Journal of Immunology*, 185(4):2273–2284, 2010.

[91] Kiavash Movahedi, Damya Laoui, Conny Gysemans, Martijn Baeten, Geert Stangé, Jan Den Van Bossche, Matthias Mack, Daniel Pipeleers, Peter In't Veld, Patrick De Baetselier, and Jo A. Van Ginderachter. Different tumor microenvironments contain functionally distinct subsets of macrophages derived from Ly6C(high) monocytes. *Cancer Research*, 70(14):5728–5739, 2010.

[92] Sripadh Sharma, Igal Ifergan, Jonathan E. Kurz, Robert A. Linsenmeier, Dan Xu, John G. Cooper, Stephen D. Miller, and John A. Kessler. Intravenous Immunomodulatory Nanoparticle Treatment for Traumatic Brain Injury. *Annals of Neurology*, 87(3):442–455, 2020.

[93] Jonghyuck Park, Yining Zhang, Eiji Saito, Steve J. Gurczynski, Bethany B. Moore, Brian J. Cummings, Aileen J. Anderson, and Lonnie D. Shea. Intravascular innate immune cells reprogrammed via intravenous nanoparticles to promote functional recovery after spinal cord injury. *Proceedings of the National Academy of Sciences of the United States of America*, 116(30):14947–14954, 2019.

[94] Quoc Viet Le, Geon Yang, Yina Wu, Ho Won Jang, Mohammadreza Shokouhimehr, and Yu Kyoung Oh. Nanomaterials for modulating innate immune cells in cancer immunotherapy. *Asian Journal of Pharmaceutical Sciences*, 14(1):16–29, 2019.

[95] Michael I. Love, Wolfgang Huber, and Simon Anders. Moderated estimation of fold change and dispersion for RNA-seq data with DESeq2. *Genome Biology*, 15(12):1–21, 2014.

[96] Trevor E. Angell, Melissa G. Lechner, Alison M. Smith, Sue E. Martin, Susan G. Groshen, Dennis R. Maceri, Peter A. Singer, and Alan L. Epstein. Circulating myeloid-derived suppressor cells predict differentiated thyroid cancer diagnosis and extent. *Thyroid*, 2016.

[97] A. L. Feng, J. K. Zhu, J. T. Sun, M. X. Yang, M. R. Neckenig, X. W. Wang, Q. Q. Shao, B. F. Song, Q. F. Yang, B. H. Kong, and X. Qu. CD16+ monocytes in breast cancer patients: Expanded by monocyte chemoattractant protein-1 and may be useful for early diagnosis. *Clinical and Experimental Immunology*, 164(1):57–65, 2011.

[98] Rita A. Mukhtar, Onouwem Nseyo, Michael J. Campbell, and Laura J. Esserman. Tumor-associated macrophages in breast cancer as potential biomarkers for new treatments and diagnostics. *Expert Review of Molecular Diagnostics*, 11(1):91–100, 2011.

[99] Alexander Hamm, Hans Prenen, Wouter Van Delm, Mario Di Matteo, Mathias Wenes, Estelle Delamarre, Thomas Schmidt, Jürgen Weitz, Roberta Sarmiento, Angelo Dezi, Giampietro Gasparini, Françoise Rothé, Robin Schmitz, André D'Hoore, Hannes Iserentant, Alain Hendlisz, and Massimiliano Mazzone. Tumour-educated circulating monocytes are powerful candidate biomarkers for diagnosis and disease follow-up of colorectal cancer. *Gut*, 65(6):990–1000, 2016.

[100] Dominic Schauer, Patrick Starlinger, Christian Reiter, Nikolaus Jahn, Philipp Zajc, Elisabeth Buchberger, Thomas Bachleitner-Hofmann, Michael Bergmann, Anton Stift, Thomas Gruenberger, and Christine Brostjan. Intermediate Monocytes but Not TIE2-Expressing Monocytes Are a Sensitive Diagnostic Indicator for Colorectal Cancer. *PLoS ONE*, 7(9):1–10, 2012.

[101] Jean M. Daley, Alan A. Thomay, Michael D. Connolly, Jonathan S. Reichner, and Jorge E. Albina. Use of Ly6G-specific monoclonal antibody to deplete neutrophils in mice. *Journal of Leukocyte Biology*, 83(1):64–70, 2008.

[102] Minu K. Srivastava, Li Zhu, Marni Harris-White, Upendra Kar, Min Huang, Ming F. Johnson, Jay M. Lee, David Elashoff, Robert Strieter, Steven Dubinett, and Sherven Sharma. Myeloid suppressor cell depletion augments antitumor activity in lung cancer. *PLoS ONE*, 7(7), 2012.

[103] Momir Bosiljcic, Rachel A. Cederberg, Melisa J. Hamilton, Nancy E. Lepard, Bryant T. Harbourne, Jenna L. Collier, Elizabeth C. Halvorsen, Rocky Shi, S. Elizabeth Franks, Ada Y. Kim, Judit P. Banáth, Mark Hamer, Fabio M. Rossi, and Kevin L. Bennewith. Targeting myeloid-derived suppressor cells in combination with primary mammary tumor resection reduces metastatic growth in the lungs. *Breast Cancer Research*, 21(1):1–16, 2019.

[104] Laura Bonapace, Marie May Coissieux, Jeffrey Wyckoff, Kirsten D. Mertz, Zsuzsanna Varga, Tobias Junt, and Mohamed Bentires-Alj. Cessation of CCL2 inhibition accelerates breast cancer metastasis by promoting angiogenesis. *Nature*, 515(7525):130–133, 2014.

[105] Michal Beffinger, Paulino Tallón de Lara, Sònia Tugues, Marijne Vermeer, Yannick Montagnolo, Isabel Ohs, Virginia Cecconi, Giulia Lucchiari, Aron Gagliardi, Nikola Misljencevic, James Sutton, Roman Spörri, Burkhard Becher, Anurag Gupta, and Maries van den Broek. CSF1R-dependent myeloid cells are required for NKmediated control of metastasis. *JCI insight*, 3(10), 2018.

[106] Cristina Perez, Cirino Botta, Aintzane Zabaleta, Noemi Puig, Maria-Teresa Cedena, Ibai Goicoechea, Daniel Alameda, Edurne San-José Enériz, Juana Merino, Paula Rodriguez-Otero, Catarina Alexandra Da Silva Maia, Diego Alignani, Patricia Maiso, Irene Manrique, David Lara-Astiaso, Amaia Vilas-Zornoza, Sarai Sarvide, Caterina Riillo, Marco Rossi, Laura Rosiñol, Albert Oriol, María-Jesús Blanchard, Rafael Rios, Anna Sureda, Jesús Martín Sánchez, Rafael Martinez, Joan Bargay, Javier de la Rubia, Miguel T Hernandez Garcia, Joaquín Martínez-López, Alberto Orfao, Xabier Agirre, Felipe Prosper, Maria-Victoria Mateos, Juan-José Lahuerta, Joan Bladé, Jesús San Miguel, and Bruno Paiva. Immunogenomic identification and characterization of granulocytic myeloid derived suppressor cells in multiple myeloma. *Blood*, 2020.

[107] Catherine A. Fromen, William J. Kelley, Margaret B. Fish, Reheman Adili, Jeffery Noble, Mark J. Hoenerhoff, Michael Holinstat, and Omolola Eniola-Adefeso. Neutrophil-Particle Interactions in Blood Circulation Drive Particle Clearance and Alter Neutrophil Responses in Acute Inflammation. *ACS Nano*, 11(11):10797–10807, 2017.

[108] Congyu Wu, Megan E. Muroski, Jason Miska, Catalina Lee-Chang, Yajing Shen, Aida Rashidi, Peng Zhang, Ting Xiao, Yu Han, Aurora Lopez-Rosas, Yu Cheng, and Maciej S. Lesniak. Repolarization of myeloid derived suppressor cells via magnetic nanoparticles to promote radiotherapy for glioma treatment. *Nanomedicine: Nanotechnology, Biology, and Medicine*, 16(xxxx):126–137, 2019.

[109] Liam M. Casey, Sandeep Kakade, Joseph T. Decker, Justin A. Rose, Kyle Deans, Lonnie D. Shea, and Ryan M. Pearson. Cargo-less nanoparticles program innate immune cell responses to toll-like receptor activation. *Biomaterials*, 218(July):119333, 2019.

[110] Eiji Saito, Robert Kuo, Ryan M. Pearson, Nishant Gohel, Brandon Cheung, Nicholas J.C. King, Stephen D. Miller, and Lonnie D. Shea. Designing drug-free biodegradable nanoparticles to modulate inflammatory monocytes and neutrophils for ameliorating inflammation. *Journal of Controlled Release*, 300(February):185–196, 2019.

[111] Soyeon Jeon, Jessica Clavadetscher, Dong Keun Lee, Sunay V. Chankeshwara, Mark Bradley, and Wan Seob Cho. Surface charge-dependent cellular uptake of polystyrene nanoparticles. *Nanomaterials*, 8(12):1–11, 2018.

[112] Laura Pinton, Sara Magri, Elena Masetto, Marina Vettore, Ilaria Schibuola, Vincenzo Ingangi, Ilaria Marigo, Kevin Matha, Jean Pierre Benoit, Alessandro Della Puppa, Vincenzo Bronte, Giovanna Lollo, and Susanna Mandruzzato. Targeting of immunosuppressive myeloid cells from glioblastoma patients by modulation of size and surface charge of lipid nanocapsules. *Journal of Nanobiotechnology*, 18(1):1–12, 2020.

[113] Bryan Ronain Smith, Eliver Eid Bou Ghosn, Harikrishna Rallapalli, Jennifer A. Prescher, Timothy Larson, Leonore A. Herzenberg, and Sanjiv Sam Gambhir. Selective uptake of single-walled carbon nanotubes by circulating monocytes for enhanced tumour delivery. *Nature Nanotechnology*, 9(6):481–487, 2014.

[114] Shuya Li, Qin Wang, Yanqiong Shen, Muhammad Hassan, Jizhou Shen, Wei Jiang, Yitan Su, Jing Chen, Li Bai, Wenchao Zhou, and Yucai Wang. Pseudoneutrophil Cytokine Sponges Disrupt Myeloid Expansion and Tumor Trafficking to Improve Cancer Immunotherapy. *Nano letters*, pages 2–11, 2019.

[115] Sachie Hiratsuka, Kazuhiro Nakamura, Shinobu Iwai, Masato Murakami, Takeshi Itoh, Hiroshi Kijima, J. Michael Shipley, Robert M. Senior, and Masabumi Shibuya. MMP9 induction by vascular endothelial growth factor receptor-1 is involved in lung-specific metastasis. *Cancer Cell*, 2(4):289–300, 2002.

[116] Juechao Zhang, Xiaoqing Han, Huifang Shi, Yanyan Gao, Xuan Qiao, Huihan Li, Min Wei, and Xianlu Zeng. Lung resided monocytic myeloid-derived suppressor cells contribute to premetastatic niche formation by enhancing MMP-9 expression. *Molecular and Cellular Probes*, 50:101498, 2020.

[117] Steven A. Rosenberg. IL-2: The First Effective Immunotherapy for Human Cancer. *The Journal of Immunology*, 2014.

[118] Nikolaos Patsoukis, Julia Brown, Victoria Petkova, Fang Liu, Lequn Li, and Vassiliki A. Boussiotis. Selective Effects of PD-1 on Akt and Ras Pathways Regulate Molecular Components of the Cell Cycle and Inhibit T Cell Proliferation. *Science Signaling*, 5(230):ra46–ra46, 2012.

[119] Anqi Zhu, Joseph G. Ibrahim, and Michael I. Love. Heavy-Tailed prior distributions for sequence count data: Removing the noise and preserving large differences. *Bioinformatics*, 35(12):2084–2092, 2019.

[120] Lyndsay N. Harris, Nofisat Ismaila, Lisa M. McShane, Fabrice Andre, Deborah E. Collyar, Ana M. Gonzalez-Angulo, Elizabeth H. Hammond, Nicole M. Kuderer, Minetta C. Liu, Robert G. Mennel, Catherine Van Poznak, Robert C. Bast, and Daniel F. Hayes. Use of Biomarkers to Guide Decisions on Adjuvant Systemic Therapy for Women With Early-Stage Invasive Breast Cancer: American Society of Clinical Oncology Clinical Practice Guideline. *Journal of Clinical Oncology*, 34(10):1134–1150, 2016.

[121] Soonmyung Paik, Steven Shak, Gong Tang, Chungyeul Kim, Joffre Baker, Maureen Cronin, Frederick L. Baehner, Michael G. Walker, Drew Watson, Taesung Park, William Hiller, Edwin R. Fisher, D. Lawrence Wickerham, John Bryant, and Norman Wolmark. A Multigene Assay to Predict Recurrence of Tamoxifen-Treated, Node-Negative Breast Cancer. *New England Journal of Medicine*, 351(27):2817–2826, 2004.

[122] Laura J. van 't Veer, Hongyue Dai, Marc J. van de Vijver, Yudong D. He, Augustinus A. M. Hart, Mao Mao, Hans L. Peterse, Karin van der Kooy, Matthew J. Marton, Anke T. Witteveen, George J. Schreiber, Ron M. Kerkhoven, Chris Roberts, Peter S. Linsley, René Bernards, and Stephen H. Friend. Gene expression profiling predicts clinical outcome of breast cancer. *Nature*, 415(6871):530–536, 2002.

[123] Giovanni Ciriello, Michael L. Gatza, Andrew H. Beck, Matthew D. Wilkerson, Suhn K. Rhie, Alessandro Pastore, Hailei Zhang, Michael McLellan, Christina Yau, Cyriac Kandoth, Reanne Bowlby, Hui Shen, Sikander Hayat, Robert Fieldhouse, Susan C. Lester, Gary M.K. Tse, Rachel E. Factor, Laura C. Collins, Kimberly H. Allison, Yunn-Yi Chen, Kristin Jensen, Nicole B. Johnson, Steffi Oesterreich, Gordon B. Mills, Andrew D. Cherniack, Gordon Robertson, Christopher Benz, Chris Sander, Peter W. Laird, Katherine A. Hoadley, Tari A. King, Charles M. Perou, Rehan Akbani, J. Todd Auman, Miruna Balasundaram, Saianand Balu, Thomas Barr, Andrew Beck, Christopher Benz, Stephen Benz, Mario Berrios, Rameen Beroukhim, Tom Bodenheimer, Lori Boice, Moiz S. Bootwalla, Jay Bowen, Reanne Bowlby, Denise Brooks, Andrew D. Cherniack, Lynda Chin, Juok Cho, Sudha Chudamani, Giovanni Ciriello, Tanja Davidsen, John A. Demchok, Jennifer B. Dennison, Li Ding, Ina Felau, Martin L. Ferguson, Scott Frazer, Stacey B. Gabriel, JianJiong Gao, Julie M. Gastier-Foster, Michael L. Gatza, Nils Gehlenborg, Mark Gerken, Gad Getz, William J. Gibson, D. Neil Hayes, David I. Heiman, Katherine A. Hoadley, Andrea Holbrook, Robert A. Holt, Alan P. Hoyle, Hai Hu, Mei Huang, Carolyn M. Hutter, E. Shelley Hwang, Stuart R. Jefferys, Steven J.M. Jones, Zhenlin Ju, Jaegil Kim, Phillip H. Lai, Peter W. Laird, Michael S. Lawrence, Kristen M. Leraas, Tara M. Lichtenberg, Pei Lin, Shiyun Ling, Jia Liu, Wenbin Liu, Laxmi Lolla, Yiling Lu, Yussanne Ma, Dennis T. Maglinte, Elaine Mardis, Jeffrey Marks, Marco A. Marra, Cynthia McAllister, Michael McLellan, Shaowu Meng, Matthew Meyerson, Gordon B. Mills, Richard A. Moore, Lisle E. Mose, Andrew J. Mungall, Bradley A. Murray, Rashi Naresh, Michael S. Noble, Steffi Oesterreich, Olufunmilayo Olopade, Joel S. Parker, Charles M. Perou, Todd Pihl, Gordon Saksena, Steven E. Schumacher, Kenna R. Mills Shaw, Nilsa C. Ramirez, W. Kimryn Rathmell, Suhn K. Rhie, Jeffrey Roach, A. Gordon Robertson, Gordon Saksena, Chris Sander, Jacqueline E. Schein, Nikolaus Schultz, Hui Shen, Margi Sheth, Yan Shi, Juliann Shih, Carl Simon Shelley, Craig Shriver, Janae V. Simons, Heidi J. Sofia, Matthew G. Soloway, Carrie Sougnez, Charlie Sun, Roy Tarnuzzer, Daniel G. Tiezzi, David J. Van Den Berg, Doug Voet, Yunhu Wan, Zhining Wang, John N. Weinstein, Daniel J. Weisenberger, Matthew D. Wilkerson, Richard Wilson, Lisa Wise, MacIej Wiznerowicz, Junyuan Wu, Ye Wu, Liming Yang, Christina Yau, Travis I. Zack, Jean C. Zenklusen, Hailei Zhang, Jiashan Zhang, and Erik Zmuda. Comprehensive Molecular Portraits of Invasive Lobular Breast Cancer. *Cell*, 163(2):506–519, 2015.

[124] Joel S. Parker, Michael Mullins, Maggie C.U. Cheang, Samuel Leung, David Voduc, Tammi Vickery, Sherri Davies, Christiane Fauron, Xiaping He, Zhiyuan Hu, John F. Quackenbush, Inge J. Stijleman, Juan Palazzo, J.S. Marron, Andrew B. Nobel, Elaine Mardis, Torsten O. Nielsen, Matthew J. Ellis, Charles M. Perou, and Philip S. Bernard. Supervised Risk Predictor of Breast Cancer Based on Intrinsic Subtypes. *Journal of Clinical Oncology*, 27(8):1160–1167, 2009.

[125] Xiao-Jun Ma, Zuncai Wang, Paula D. Ryan, Steven J. Isakoff, Anne Barmettler, Andrew Fuller, Beth Muir, Gayatry Mohapatra, Ranelle Salunga, J.Todd Tuggle, Yen Tran, Diem Tran, Ana Tassin, Paul Amon, Wilson Wang, Wei Wang, Edward Enright, Kimberly Stecker, Eden Estepa-Sabal, Barbara Smith, Jerry Younger, Ulysses Balis, James Michaelson, Atul

Bhan, Karleen Habin, Thomas M. Baer, Joan Brugge, Daniel A. Haber, Mark G. Erlander, and Dennis C. Sgroi. A two-gene expression ratio predicts clinical outcome in breast cancer patients treated with tamoxifen. *Cancer Cell*, 5(6):607–616, 2004.

[126] P. Dubsky, J. C. Brase, R. Jakesz, M. Rudas, C. F. Singer, R. Greil, O. Dietze, I. Luisser, E. Klug, R. Sedivy, M. Bachner, D. Mayr, M. Schmidt, M. C. Gehrmann, C. Petry, K. E. Weber, K. Fisch, R. Kronenwett, M. Gnant, and M. Filipits. The EndoPredict score provides prognostic information on late distant metastases in ER+/HER2 breast cancer patients. *British Journal of Cancer*, 109(12):2959–2964, 2013.

[127] Andy J. Minn, Yibin Kang, Inna Serganova, Gaorav P. Gupta, Dilip D. Giri, Mikhail Doubrovin, Vladimir Ponomarev, William L. Gerald, Ronald Blasberg, and Joan Massagué. Distinct organ-specific metastatic potential of individual breast cancer cells and primary tumors. *Journal of Clinical Investigation*, 115(1):44–55, 2005.

[128] Keith J. Luzzi, Ian C. MacDonald, Eric E. Schmidt, Nancy Kerkvliet, Vincent L. Morris, Ann F. Chambers, and Alan C. Groom. Multistep Nature of Metastatic Inefficiency. *The American Journal of Pathology*, 153(3):865–873, 1998.

[129] Zhongyi Zhu, Si Qiu, Kang Shao, and Yong Hou. Progress and challenges of sequencing and analyzing circulating tumor cells. *Cell Biology and Toxicology*, 34(5):405–415, 2018.

[130] Brian A. Aguado, Jordan R. Caffe, Dhaval Nanavati, Shreyas S. Rao, Grace G. Bushnell, Samira M. Azarin, and Lonnie D. Shea. Extracellular matrix mediators of metastatic cell colonization characterized using scaffold mimics of the pre-metastatic niche. *Acta Biomaterialia*, 33:13–24, 2016.

[131] Francesca Bersani, Jungwoo Lee, Min Yu, Robert Morris, Rushil Desai, Sridhar Ramaswamy, Mehmet Toner, Daniel A. Haber, and Biju Parekkadan. Bioengineered Implantable Scaffolds as a Tool to Study Stromal-Derived Factors in Metastatic Cancer Models. *Cancer Research*, 74(24):7229–7238, 2014.

[132] Brian A. Aguado, Rachel M. Hartfield, Grace G. Bushnell, Joseph T. Decker, Samira M. Azarin, Dhaval Nanavati, Matthew J. Schipma, Shreyas S. Rao, Robert S. Oakes, Yining Zhang, Jacqueline S. Jeruss, and Lonnie D. Shea. Biomaterial Scaffolds as Pre-metastatic Niche Mimics Systemically Alter the Primary Tumor and Tumor Microenvironment. *Advanced Healthcare Materials*, 7(10):1700903, 2018.

[133] Jungwoo Lee, Matthew Li, Jack Milwid, Joshua Dunham, Claudio Vinegoni, Rostic Gorbatov, Yoshiko Iwamoto, Fangjing Wang, Keyue Shen, Kimberley Hatfield, Marianne Enger, Sahba Shafiee, Emmet McCormack, Benjamin L. Ebert, Ralph Weissleder, Martin L. Yarmush, and Biju Parekkadan. Implantable microenvironments to attract hematopoietic stem/cancer cells. *Proceedings of the National Academy of Sciences*, 109(48):19638–19643, nov 2012.

[134] Grace G. Bushnell, Xiaowei Hong, Rachel M. Hartfield, Yining Zhang, Robert S. Oakes, Shreyas S. Rao, Jacqueline S. Jeruss, Jan P. Stegemann, Cheri X. Deng, and Lonnie D. Shea. High Frequency Spectral Ultrasound Imaging to Detect Metastasis in Implanted Biomaterial Scaffolds. *Annals of Biomedical Engineering*, 48(1):477–489, 2020.

[135] Amber Jin Giles, Caitlin Marie Reid, Justin DeWayne Evans, Meera Murgai, Yorleny Vicioso, Steven Lorenz Highfill, Miki Kasai, Linda Vahdat, Crystal Lee Mackall, David Lyden, Leonard Wexler, and Rosandra Natasha Kaplan. Activation of Hematopoietic Stem/Progenitor Cells Promotes Immunosuppression Within the Premetastatic Niche. *Cancer Research*, 76(6):1335–1347, 2016.

[136] Sachie Hiratsuka, Akira Watanabe, Hiroyuki Aburatani, and Yoshiro Maru. Tumour-mediated upregulation of chemoattractants and recruitment of myeloid cells predetermines lung metastasis. *Nature Cell Biology*, 8(12):1369–1375, 2006.

[137] Pratima Sinha, Chinonyerem Okoro, Dirk Foell, Hudson H. Freeze, Suzanne Ostrand-Rosenberg, and Geetha Srikrishna. Proinflammatory S100 Proteins Regulate the Accumulation of Myeloid-Derived Suppressor Cells. *The Journal of Immunology*, 181(7):4666–4675, 2008.

[138] Nuria Oliva, Maria Carcole, Margarita Beckerman, Sivan Seliktar, Alison Hayward, James Stanley, Nicola Maria Anne Parry, Elazer R. Edelman, and Natalie Artzi. Regulation of dendrimer/dextran material performance by altered tissue microenvironment in inflammation and neoplasia. *Science Translational Medicine*, 7(272):272ra11–272ra11, 2015.

[139] Teresa Oviedo Socarrás, Anilton C. Vasconcelos, Paula P. Campos, Nubia B. Pereira, Jessica P. C. Souza, and Silvia P. Andrade. Foreign Body Response to Subcutaneous Implants in Diabetic Rats. *PLoS ONE*, 9(11):e110945, 2014.

[140] Arturo J. Vegas, Omid Veiseh, Joshua C. Doloff, Minglin Ma, Hok Hei Tam, Kaitlin Bratlie, Jie Li, Andrew R. Bader, Erin Langan, Karsten Olejnik, Patrick Fenton, Jeon Woong Kang, Jennifer Hollister-Locke, Matthew A. Bochenek, Alan Chiu, Sean Siebert, Katherine Tang, Siddharth Jhunjhunwala, Stephanie Aresta-Dasilva, Nimit Dholakia, Raj Thakrar, Thema Vietti, Michael Chen, Josh Cohen, Karolina Siniakowicz, Meirigeng Qi, James McGarrigle, Adam C Graham, Stephen Lyle, David M. Harlan, Dale L. Greiner, Jose Oberholzer, Gordon C. Weir, Robert Langer, and Daniel G. Anderson. Combinatorial hydrogel library enables identification of materials that mitigate the foreign body response in primates. *Nature Biotechnology*, 34(3):345–352, 2016.

[141] Ksenya Kveler, Elina Starosvetsky, Amit Ziv-Kenet, Yuval Kalugny, Yuri Gorelik, Gali Shalev-Malul, Netta Aizenbud-Reshef, Tania Dubovik, Mayan Briller, John Campbell, Jan C. Rieckmann, Nuaman Asbeh, Doron Rimar, Felix Meissner, Jeff Wiser, and Shai S. Shen-Orr. Immune-centric network of cytokines and cells in disease context identified by computational mining of PubMed. *Nature Biotechnology*, 36(7):651–659, 2018.

[142] Je-In Youn, Michelle Collazo, Irina N. Shalova, Subhra K. Biswas, and Dmitry I. Gabrilovich. Characterization of the nature of granulocytic myeloid-derived suppressor cells in tumor-bearing mice. *Journal of Leukocyte Biology*, 91(1):167–181, 2012.

[143] Jan M. Ehrchen, Cord Sunderkötter, Dirk Foell, Thomas Vogl, and Johannes Roth. The endogenous Toll-like receptor 4 agonist S100A8/S100A9 (calprotectin) as innate amplifier of infection, autoimmunity, and cancer. *Journal of Leukocyte Biology*, 86(3):557–566, 2009.

[144] Maryann Kwa, Andreas Makris, and Francisco J. Esteva. Clinical utility of gene-expression signatures in early stage breast cancer. *Nature Reviews Clinical Oncology*, 14(10):595–610, 2017.

[145] Kevin A Janes and Douglas A Lauffenburger. A biological approach to computational models of proteomic networks. *Current Opinion in Chemical Biology*, 10(1):73–80, 2006.

[146] Orly Alter, Patrick O. Brown, and David Botstein. Singular value decomposition for genome-wide expression data processing and modeling. *Proceedings of the National Academy of Sciences*, 97(18):10101–10106, 2000.

[147] Leo Breiman. Random forests. *Machine Learning*, 45:5–32, 2001.

[148] Jae-Hyung Jang, Christopher B. Rives, and Lonnie D. Shea. Plasmid Delivery in Vivo from Porous Tissue-Engineering Scaffolds: Transgene Expression and Cellular Transfection. *Molecular Therapy*, 12(3):475–483, 2005.

[149] Pingyan Cheng, Cesar A. Corzo, Noreen Luetteke, Bin Yu, Srinivas Nagaraj, Marylin M. Bui, Myrna Ortiz, Wolfgang Nacken, Clemens Sorg, Thomas Vogl, Johannes Roth, and Dmitry I. Gabrilovich. Inhibition of dendritic cell differentiation and accumulation of myeloid-derived

suppressor cells in cancer is regulated by S100A9 protein. *Journal of Experimental Medicine*, 205(10):2235–2249, 2008.

[150] Sachie Hiratsuka, Akira Watanabe, Yoshiko Sakurai, Sachiko Akashi-Takamura, Sachie Ishibashi, Kensuke Miyake, Masabumi Shibuya, Shizuo Akira, Hiroyuki Aburatani, and Yoshiro Maru. The S100A8serum amyloid A3TLR4 paracrine cascade establishes a pre-metastatic phase. *Nature Cell Biology*, 10(11):1349–1355, 2008.

[151] Anne Becker, Nils Große Hokamp, Stefanie Zenker, Fabian Flores-Borja, Katarzyna Barzcyk, Georg Varga, Johannes Roth, Christiane Geyer, Walter Heindel, Christoph Bremer, Thomas Vogl, and Michel Eisenblaetter. Optical In Vivo Imaging of the Alarmin S100A9 in Tumor Lesions Allows for Estimation of the Individual Malignant Potential by Evaluation of Tumor-Host Cell Interaction. *Journal of Nuclear Medicine*, 56(3):450–456, 2015.

[152] Maria Ouzounova, Eunmi Lee, Raziye Piranlioglu, Abdeljabar El Andaloussi, Ravindra Kolhe, Mehmet F. Demirci, Daniela Marasco, Iskander Asm, Ahmed Chadli, Khaled A. Hassan, Muthusamy Thangaraju, Gang Zhou, Ali S. Arbab, John K. Cowell, and Hasan Korkaya. Monocytic and granulocytic myeloid derived suppressor cells differentially regulate spatiotemporal tumour plasticity during metastatic cascade. *Nature Communications*, 8(1):14979, 2017.

[153] Stephanie Downs-Canner, Sara Berkey, Greg M. Delgoffe, Robert P. Edwards, Tyler Curiel, Kunle Odunsi, David L. Bartlett, and Nataša Obermajer. Suppressive IL-17A+Foxp3+ and ex-Th17 IL-17AnegFoxp3+ Treg cells are a source of tumour-associated Treg cells. *Nature Communications*, 8(1):14649, 2017.

[154] Günther Weber, Clara Ibel Chamorro, Fredrik Granath, Annelie Liljegren, Sami Zreika, Zuzana Saidak, Bengt Sandstedt, Samuel Rotstein, Romuald Mentaverri, Fabio Sánchez, Andor Pivarcsi, and Mona Ståhle. Human antimicrobial protein hCAP18/LL-37 promotes a metastatic phenotype in breast cancer. *Breast Cancer Research*, 11(1):R6, 2009.

[155] Do-Hyun Kim, Hong-Jai Park, Sangho Lim, Ja-Hyun Koo, Hong-Gyun Lee, Jin Ouk Choi, Ji Hoon Oh, Sang-Jun Ha, Min-Jong Kang, Chang-Min Lee, Chun Geun Lee, Jack A. Elias, and Je-Min Choi. Regulation of chitinase-3-like-1 in T cell elicits Th1 and cytotoxic responses to inhibit lung metastasis. *Nature Communications*, 9(1):503, 2018.

[156] Anja Müller, Bernhard Homey, Hortensia Soto, Nianfeng Ge, Daniel Catron, Matthew E. Buchanan, Terri McClanahan, Erin Murphy, Wei Yuan, Stephan N. Wagner, Jose Luis Barrera, Alejandro Mohar, Emma Verástegui, and Albert Zlotnik. Involvement of chemokine receptors in breast cancer metastasis. *Nature*, 410(6824):50–56, 2001.

[157] Tyler J. Curiel, George Coukos, Linhua Zou, Xavier Alvarez, Pui Cheng, Peter Mottram, Melina Evdemon-Hogan, Jose R. Conejo-Garcia, Lin Zhang, Matthew Burow, Yun Zhu, Shuang Wei, Ilona Kryczek, Ben Daniel, Alan Gordon, Leann Myers, Andrew Lackner, Mary L. Disis, Keith L. Knutson, Lieping Chen, and Weiping Zou. Specific recruitment of regulatory T cells in ovarian carcinoma fosters immune privilege and predicts reduced survival. *Nature Medicine*, 10(9):942–949, 2004.

[158] Andy J. Minn, Gaorav P. Gupta, Peter M. Siegel, Paula D. Bos, Weiping Shu, Dilip D. Giri, Agnes Viale, Adam B. Olshen, William L. Gerald, and Joan Massagué. Genes that mediate breast cancer metastasis to lung. *Nature*, 436(7050):518–524, 2005.

[159] Robert S. Oakes, Eugene Froimchuk, and Christopher M. Jewell. Engineering Biomaterials to Direct Innate Immunity. *Advanced Therapeutics*, 2(6):1800157, 2019.

[160] Mark Robson, Seock-Ah Im, Elżbieta Senkus, Binghe Xu, Susan M. Domchek, Norikazu Masuda, Suzette Delaloge, Wei Li, Nadine Tung, Anne Armstrong, Wenting Wu, Carsten Goessl, Sarah Runswick, and Pierfranco Conte. Olaparib for Metastatic Breast Cancer in Patients with a Germline BRCA Mutation. *New England Journal of Medicine*, 377(6):523–533, 2017.

[161] P. Schmid, S. Adams, H.S. Rugo, A. Schneeweiss, C.H. Barrios, H. Iwata, V. Dieras, R. Hegg, S.-A. Im, G.S. Wright, V. Henschel, L. Molinero, S.Y. Chui, R. Funke, A. Husain, E.P. Winer, S. Loi, and L.A. Emens. IMpassion130: Results from a global, randomised, double-blind, phase III study of atezolizumab (atezo) + nab-paclitaxel (nab-P) vs placebo + nab-P in treatment-naive, locally advanced or metastatic triple-negative breast cancer (mTNBC). *Annals of Oncology*, 29:viii707–viii708, 2018.

[162] Chi Ma, Tamar Kapanadze, Jaba Gamrekelashvili, Michael P. Manns, Firouzeh Korangy, and Tim F. Greten. Anti-Gr-1 antibody depletion fails to eliminate hepatic myeloid-derived suppressor cells in tumor-bearing mice. *Journal of Leukocyte Biology*, 92(6):1199–1206, 2012.

[163] Vinit Kumar, Sima Patel, Evgenii Tcyganov, and Dmitry I. Gabrilovich. The Nature of Myeloid-Derived Suppressor Cells in the Tumor Microenvironment. *Trends in Immunology*, 37(3):208–220, 2016.

[164] Marcin Kowanetz, Xiumin Wu, John Lee, Martha Tan, Thijs Hagenbeek, Xueping Qu, Lanlan Yu, Jed Ross, Nina Korsisaari, Tim Cao, Hani Bou-Reslan, Dara Kallop, Robby Weimer, Mary J.C. Ludlam, Joshua S. Kaminker, Zora Modrusan, Nicholas Van Bruggen, Franklin V. Peale, Richard Carano, Y. Gloria Meng, and Napoleone Ferrara. Granulocyte-colony stimulating factor promotes lung metastasis through mobilization of Ly6G+Ly6C+ granulocytes. *Proceedings of the National Academy of Sciences of the United States of America*, 2010.

[165] Hamad Alshetaiwi, Nicholas Pervolarakis, Laura Lynn McIntyre, Dennis Ma, Quy Nguyen, Jan Akara Rath, Kevin Nee, Grace Hernandez, Katrina Evans, Leona Torosian, Anushka Silva, Craig Walsh, and Kai Kessenbrock. Defining the emergence of myeloid-derived suppressor cells in breast cancer using single-cell transcriptomics. *Science immunology*, 2020.